MODULATION OF TERAHERTZ WAVES BY VO_2 BASED METAMATERIALS

A Thesis Submitted to
the Graduate School of Engineering and Sciences of
İzmir Institute of Technology
in Partial Fulfillment of the Requirements for the Degree of

DOCTOR OF PHILOSOPHY

in Physics

by
Aileen Noori

June 2023
İZMİR

We approve the thesis of **Aileen Noori**

Prof. Dr. Gülnur AYGÜN
Department of Physics, İzmir Institute of Technology

Prof. Dr. Hakan ALTAN
Department of Physics, Middle East Technical Unitverisy

Prof. Dr. Cem ÇELEBİ
Department of Physics, İzmir Institute of Technology

Prof. Dr. Sinan BALCI
Department of Photonic, İzmir Institute of Technology

Assoc. Prof. Dr. İlbeyi AVCI
Department of Physics, Ege University

June 6, 2023

Prof. Dr. Lütfi ÖZYÜZER
Head of the Department of
Department of Physics

Prof. Dr. Mehtap EANES
Dean of the Graduate School of
Engineering and Sciences

Dedicated to my family

ACKNOWLEDGMENTS

I appreciate the knowledge, support, and direction provided by my supervisor, Prof. Dr. Gulnur Aygun, and my defense committee. I'd like to thank thesis monitoring committee members Prof. Dr. Hakan Altan, Prof. Dr. Cem Celebi, and also Prof. Dr. Kaan Guven for providing me with knowledge and experience that I would not have had otherwise. Furthermore, I would like to express my gratitude to Prof. Dr. Lutfi Ozyuzer for his continued support and guidance with my thesis study.

This research was supported by TUBITAK (Scientific and Technological Research Council of Turkey) with project number 119R038 and partially by the University Research Foundation (BAP) with project numbers 2022IYTE-1-0101 and 2021 IYTE-1-0052. I would like to thank the Research and Application Center for Quantum Technologies (RACQUT) of IZTECH for experimental facilities. I would also like to thank the Turkish Scholarship (YTB) for funding my Ph.D. for about 5 years and 1 year of Turkish education.

ABSTRACT

MODULATION OF TERAHERTZ WAVES BY VO_2 BASED METAMATERIALS

Terahertz (THz) waves, being a form of electromagnetic radiation have frequencies ranging from 0.1 THz to 10 THz. Due to the lack of suitable radiation sources and detectors, this region is not well known. Interaction with THz waves becomes more effective by introducing the metamaterials (MM) and metasurfaces (MS) (3D and 2D, respectively), which are made up of artificially subwavelength compositions arranged in periodic arrays. MMs provide a unique control on the propagation of (EM) waves and their geometries determine their properties. Recently, coding MM has made it possible to regulate the far-field scattering pattern of EM waves. In other words, it is possible to shape the THz wavefront by changing the sequence of the coding unit cells into a 2D surface pattern. The reflection phase of the two types of unit cells in 1-bit coding MM is 0 and π.

In this thesis, two different types of coding MMs were designed and fabricated. One type is hard-coded (metal-based), while the other is based on VO_2 thin film. Both types of samples share a similar structure, which includes a sapphire substrate, a gold patch, a PET layer serving as a dielectric spacer, and a ground gold layer. However, there is an additional layer of VO_2 beneath the gold patch and on top of the sapphire substrate in one of the fabricated MMs. The coding MM consists of two identical unit cells, with the only distinction being the size of the gold patch's side. This size determines whether the unit cell is considered as 0-bit or 1-bit. When the side size is 90 µm, the unit cell is 0-bit. On the other hand, when the side sizes are 60 µm and 70 µm (for different samples), the unit cell is 1-bit. Two different sets of hard-coded MM were fabricated. One set is composed of the 60-90 µm unit cells arranged in the form of checkerboard and stripe designs. The other set is made of 70-90 µm unit cells arranged in the form of checkerboard and stripe designs. The samples were measured with a custom-built setup and the THz full spectrum (0.50-0.75 THz) was obtained at each reflection angle. The results indicate that the checkerboard samples' reflection angle for each frequency has a good consistency with the calculations. Since the detector was obstructing the incoming beam, the measurable angle range begins at 23 degrees from normal incidence. This issue limits the ability to obtain the maximum scattering pattern of the strip design samples.

At the final section of the thesis, the VO_2-based MM, was fabricated and measured. VO_2 layer was used in this structure, due to its phase-changing characteristic. It

undergoes a reversible transformation from an insulator to a metallic state at about 68°C. The initial concept was to design and fabricate the MM just entirely out of 1-bit (60 µm) unit cells. After that, using a CW laser pump and a digital micromirror (DMD), convert this 1-bit into the 0-bit unit cell by modifying the conductivity of the VO_2 layer of each individual unit cell. Using this idea, it was possible to develop a tunable digital MM. However, the CST simulation results demonstrated that the proposed MM is ineffective due to the significant amplitude difference between the 0 and 1-bit unit cells. Due to that, using the VO_2-based unit cells (0 and 1-bit) the striped and checkerboarded pattern of MMs was designed and fabricated. The VO_2 conductivity was modulated using a CW 915 nm laser beam. The measurement results show that VO_2-based MM can be used for THz beam splitting at room temperature, and the scattering pattern weakens when the laser is illuminated over the sample, causing the VO_2 layer to turn conductive.

CST Studio Suite simulation software was used to determine the unit cells' geometrical dimensions, amplitudes, and phases. The analytical calculations were performed using MATLAB. The investigated MM has the potential to be used in THz communications.

ÖZET

VO$_2$ TABANLI METAMALZEMELER İLE TERAHERTZ DALGALARİ MODÜLASYONU

Elektromanyetik radyasyonun bir formu olan terahertz (THz) dalgaları, 0,1 THz ile 10 THz arasında değişen frekanslara sahiptir. Uygun radyasyon kaynaklarının ve dedektörlerin bulunmaması sonucu bu bölge çok iyi bilinmemektedir. THz dalgaları ile etkileşim, periyodik dizilerde düzenlenmiş yapay olarak alt dalga boyu bileşimlerinden oluşan metamalzemeler (MM) ve metayüzeyler (MS) (sırasıyla 3D ve 2D) tanıtılarak daha etkili hale gelir. MM'ler, elektromanyetik (EM) dalgaların yayılması üzerinde benzersiz bir kontrol sağlar ve geometrileri özelliklerini belirler. Son zamanlarda, MM kodlaması, EM dalgalarının uzak alan saçılma modelini düzenlemeyi mümkün kılmıştır. Başka bir deyişle, kodlama birim hücrelerinin dizisini 2 boyutlu bir yüzey modeline değiştirerek THz dalga cephesini şekillendirmek mümkün kılmıştır. 1 bitlik kodlama MM'sindeki iki tür birim hücrenin yansıma fazları 0 ve π'dir. Kodlama birim hücrelerinin dizisini 2B bir yüzey deseni haline dönüştürerek THz dalgasının ön yüzünü şekillendirmek mümkündür. Bir 2B yüzey modelinde, kodlama birim hücrelerinin dizisini değiştirerek THz dalga cephesini şekillendirmek mümkündür.

Bu tezde, iki farklı tipte kodlama MM'si tasarlanmış ve üretilmiştir. Bir türü sabit kodlama (metal tabanlı), diğeri ise VO$_2$ ince film tabanlıdır. Her iki numune türü de benzer bir yapıyı paylaşır; safir bir altaş, bir şekillendirilmiş altın katmanı, dielektrik ayırıcı görevi gören bir PET tabakası ve bir altın taban katmanı içermektedir. Bununla birlikte, fabrikasyon MM'lerden birinde şekillendirilmiş altın katmanın altında ve safir altaşın üstünde ek bir VO$_2$ katmanı vardır. Kodlama MM'si iki özdeş birim hücreden oluşur ve tek fark, şekillendirilmiş altın katmanın yan tarafının boyutudur. Bu boyut, birim hücrenin 0 bit mi yoksa 1 bit mi olarak kabul edildiğini belirler. Kenar boyutu 90 µm olduğunda birim hücre 0 bittir. Öte yandan, kenar boyutları 60 µm ve 70 µm olduğunda (farklı örnekler için), birim hücre 1 bittir. Sabit kodlama MM'sinin iki farklı seti imal edilmiştir. Bir set, dama tahtası ve şerit tasarımları şeklinde düzenlenmiş 60-90 µm birim hücrelerden oluşmaktadır. Diğer takım damalı ve şerit desenler şeklinde dizilmiş 70-90 µm birim hücrelerden oluşmaktadır. Numuneler, özel yapım bir kurulumla ölçülmüş ve her yansıma açısında THz tam spektrumu (0,50-0,75 THz) elde edilmiştir. Sonuçlar, dama tahtası örneklerinin her frekans için yansıma açısının hesaplamalarla iyi bir tutarlılığa sahip olduğunu göstermektedir. Dedektör gelen ışını engellediğinden,

ölçülebilir açı aralığı normal gelişten 23 derecede başlamaktadır. Bu sorun, şerit tasarım numunelerinin maksimum saçılma modelini elde etme yeteneğini sınırlamaktadır.

Tezin son bölümünde, VO_2 tabanlı MM üretilmiş ve ölçülmüştür. Bu yapıda faz değiştirme özelliğinden dolayı VO_2 tabakası kullanılmıştır. Yapı, yaklaşık 68°C'de bir yalıtkan durumdan metalik bir duruma tersinir bir şekilde dönüşüme uğramaktadır. İlk aşamadaki amaç, MM'yi tamamen 1 bitlik (60 µm) birim hücrelerden tasarlamak ve üretmekti. Ardından, bir CW lazer pompası ve bir dijital mikro ayna (DMD) kullanarak, her bir birim hücrenin VO_2 katmanının iletkenliğini değiştirerek bu 1-biti, 0-bit birim hücreye dönüştürüldü. Bu fikri kullanarak, bir ayarlanabilir dijital MM geliştirmek mümkün olmuştur. Bununla birlikte, CST simülasyon sonuçları, önerilen MM'nin, 0 ve 1 bitlik birim hücreler arasındaki önemli genlik farkı nedeniyle etkisiz olduğunu gösterdi. Bu nedenle, MM'lerin şerit ve damalı deseni, VO_2 tabanlı birim hücreler kullanılarak tasarlanmış ve üretilmiştir. VO_2 iletkenliği, bir CW 915 nm lazer ışını kullanılarak modüle edilmiştir. Ölçüm sonuçları, VO_2 tabanlı MM'nin oda sıcaklığında THz ışın ayırma için kullanılabileceğini ve lazer numune üzerinde aydınlatıldığında saçılma modelinin zayıflayarak VO_2 tabakasının iletken hale gelmesine neden olduğunu göstermektedir.

Birim hücrelerin geometrik boyutlarını, genliklerini ve fazlarını belirlemek için CST Studio Suite simülasyon yazılımı kullanılmıştır. Analitik hesaplamalar ise MATLAB kullanılarak yapılmıştır. İncelenen MM, THz iletişiminde kullanılma potansiyeline sahiptir.

TABLE OF CONTENTS

LIST OF FIGURES

CHAPTER 1

INTRODUCTION

1.1. Terahertz Radiation

The Terahertz waves are those in the electromagnetic spectrum that have frequencies between the mid-infrared and the microwave. Its frequency range is between 0.1 and 10 THz, which translates to a wavelength range between 3 mm and 30 µm (Sun et al., 2021; Tonouchi, 2007). Due to the lack of suitable radiation sources and detectors, this region is not very well known (Davies et al., 2002) and sometimes this region is called as THz gap. THz waves science has been used extensively in research and technologies. The corresponding wavelength, energy, wavenumber, and frequency of the THz waves and their corresponding applications are shown in Figure 1.1. THz has low photon energy (4.14 meV at 1 THz). This value corresponds to the energy levels related to a molecule's rotational and vibrational modes and to structural vibrations within molecules, such as hydrogen bonds (D'Arco et al., 2020). The need for faster communication drives researchers to employ the THz frequency. THz modulators are one of the key components of THz communications (Ma et al., 2019). Modulators must actively manage the precise electromagnetic properties of the THz radiation in order to provide flexible THz measurement equipment (Rahm et al., 2013). The characteristics of modulation can be categorized by the type of control that they provide. These characteristics can include phase, spectrum, amplitude, waveform, spatial, temporal properties, and so on. Also, it is quite common for modulators to modify several aspects of the THz waves simultaneously (Rahm et al., 2013). The manipulation may occur under controlled conditions or may take place unpredictably (Rahm et al., 2013).

1.1.1. THz Applications

Some of the THz applications are imaging (Mittleman et al., 1996), spectroscopy, communication technology, and the medical field (Wang et al., 2019) (Figure 1.2).

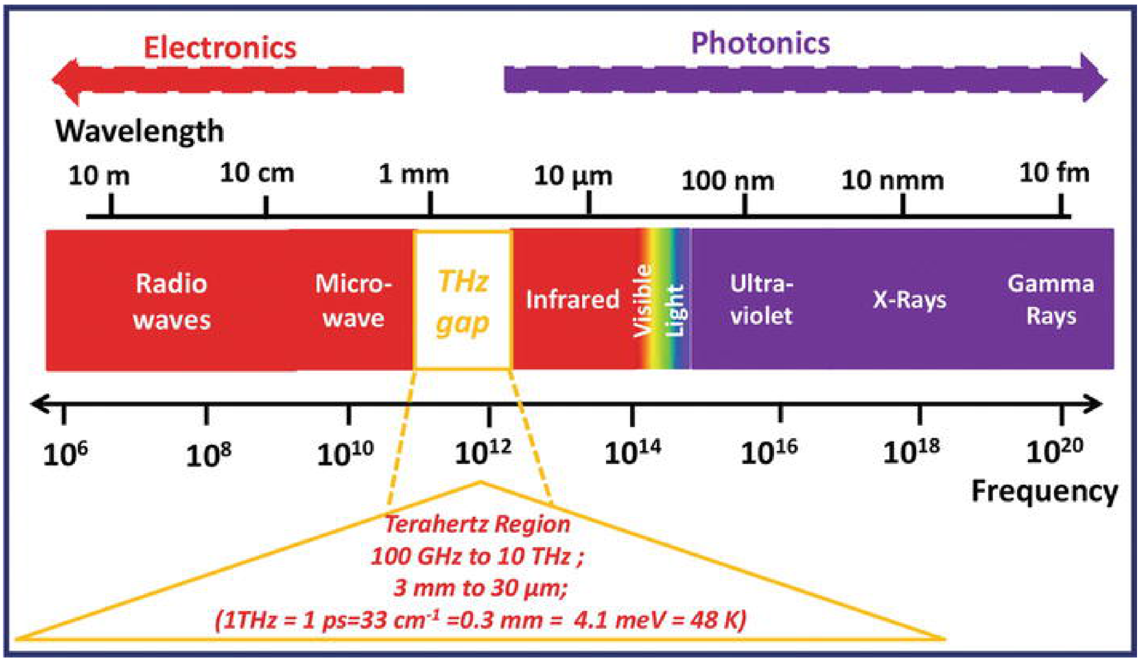

Figure 1.1. The THz spectrum region. Source: (Uddin, 2017)

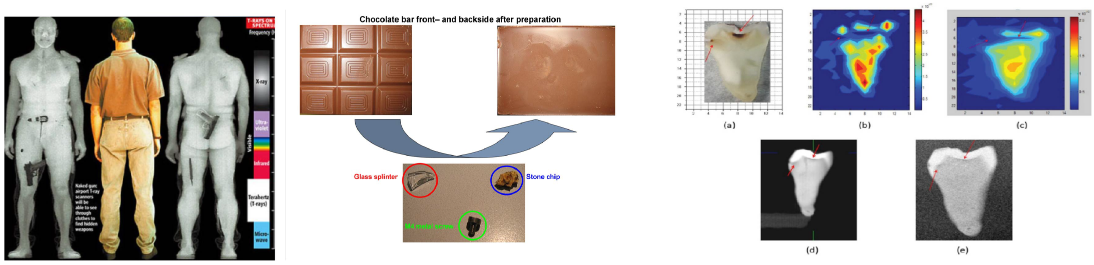

Security
Source: https://othjournal.com

Food Processing
Source: (Joerdens et al., 2006)

Medical imaging
Source: (D'Arco et al.,2020)

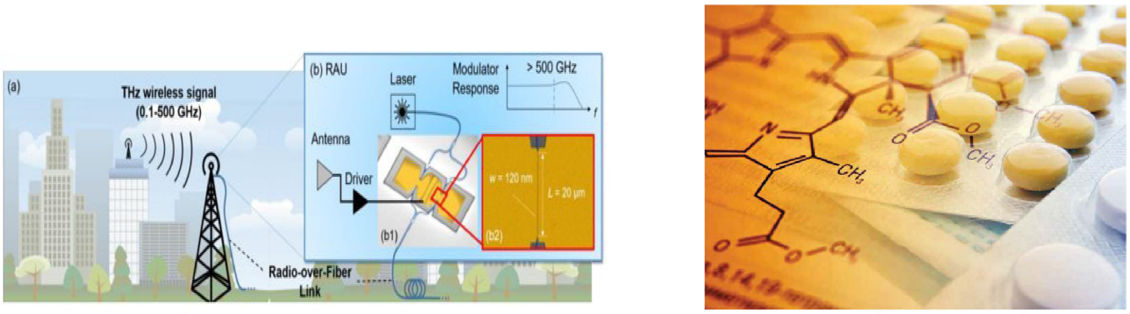

Wireless communication
Source: (Burla et al., 2019)

Pharmaceuticals
Source: https://teraview.com

Figure 1.2. Some of the THz applications.

In the presence of water molecules, THz waves will be absorbed; Thus, they can be used in the characterization of the animal's skin tissues (He et al., 2006).

THz radiation can pass through most dielectrics as well as intrinsic semiconductors easily (Tonouchi, 2007). THz light can be used for data communication due to large bandwidth and high bit transmission rates (El Haddad et al., 2013; Rahm et al., 2013). As an example of THz application, THz domain spectroscopy (TDS) is used for quality monitoring in the food industry. Compared with conventional metal detectors, TDS can acquire 2D images with higher spatial resolution, which can reveal some kind of food contamination since it is able to penetrate the food and show the contamination in detail (Jördens et al., 2006). The THz can be used in wireless communications (Burla et al., 2019). THz is used to characterize the spectral features of biomolecules and identify them using its low-frequency motions (D'Arco et al., 2020). THz radiation is reflected by metals so it can be used for security monitoring in the case of hidden devices and materials under clothes, in plastic boxes and etc (Kemp et al., 2003).

1.2. Metamaterials

In 1968, Victor Veselago explained the hypothetical material with both negative electric permittivity and magnetic permeability in his research paper (Pendry and Smith, 2004). This research leads to the discovery of an artificial material, which does not exist in nature. This unique material is called metamaterials (MM). MMs are artificially subwavelength compositions arranged in periodic arrays, in which their geometries determine their properties. MMs respond to electromagnetic waves in a unique way, due to that, they are one of the best candidates in the research area as a multifunctional material and devices. Having control over the permittivity and permeability of the MMs is allowed because their responses to the EM waves are obtained by their structure and physical geometry (Zhang et al., 2019). MMs are usually characterized by continuous and uniform macroscopic medium parameters, based on the effective medium theory (Cui et al., 2014; Landy et al., 2008; Tao et al., 2008). The refractive index is directly related to the two properties of the material: permittivity and permeability, which together indicate the wave phase velocity inside the material. The dielectric properties of MMs can be used to control the resonance of MMs (Shin et al., 2022). The Drude-Lorentz model is useful for understanding how negative values occur in materials (Pendry and Smith, 2004).

$$\varepsilon(\omega) = 1 - \frac{\omega_p^2 - \omega_0^2}{\omega^2 - \omega_0^2 + i\omega\Gamma} \tag{1.1}$$

For applying Eq.1.1 in MMs, the geometry of the cell will be used to determine the plasma frequency ω_p and the resonance frequency ω_0. While in natural materials, these properties are obtained by the charge, effective mass, and density of electrons. For any frequency between the resonance frequency and plasma frequency, the permittivity is negative (Pendry and Smith, 2004). To obtain a negative permeability inside the conductors local currents must circulate in closed loops to produce a magnetic response. It is possible to achieve this by creating a resonance within the element, causing a negative permeability (Pendry and Smith, 2004).

MMs usually are described by different theoretical models such as effective medium theory, transmission line modeling, coupled mode, and interference theory. All of these models are somehow connected to each other (Duan et al., 2019). An example is transmission line theory, where the relationship between structural parameters and electromagnetic characteristics from microwave to optical frequencies is discussed (Itoh and Caloz, 2005; Pu et al., 2011) and one study also conducted in THz regime (Wen et al., 2009). 2-dimensional or planar MMs are called metasurfaces (MS) which are more applicable in EM wave manipulating due to their less complexity with respect to the MMs which need a sophisticated fabrication technology (Rajabalipanah et al., 2019). Wavefront control (Cai et al., 2021), cloaking (Manjappa et al., 2018; Zhou et al., 2011), perfect absorption (Cheng et al., 2019; Dhillon and Mittal, 2019; Scarborough et al., 2012; Tao et al., 2008), filters (Huang et al., 2020), superlenses (Pendry, 2000; Scarborough et al., 2012), and holography (Huang et al., 2013; Kuznetsov et al., 2015; Ni et al., 2013; Zheng et al., 2015) are a few of the applications of MSs. A variety of THz applications, use MSs because of their astonishing characteristics, including modulators (Ahmadivand et al., 2019; Bai et al., 2016; Chen et al., 2009; Yuan et al., 2019), filters (Huang et al., 2020; Lee et al., 2018; Zhu et al., 2012), polarization converters (Cong et al., 2013), sensors (Alves et al., 2012) and switching (Ou et al., 2020), and so on.

A research group introduced the concept of ”Coding metamaterial”, opening up a whole new world in the MMs industry in 2014 (Cui et al., 2014; Della Giovampaola and Engheta, 2014). They have demonstrated coding MMs using two different unit cells consisting of the same structures but different widths, that respond to the signal in two different phases 0 and π. Binary representation in digital mode could be shown as ”0” and ”1” unit cell (Cui et al., 2014). There have been many studies that propose different coding MMs structures that utilize different coding sequences to manipulate electromagnetic waves, such as anomalous beam reflections and random diffusion (Chen et al., 2018; Liu et al., 2016; Shabanpour et al., 2020; Shao et al., 2019; Zhang et al., 2017). There are also some researches that introduced the 2-bit and multi-bit MMs (Gao et al., 2015). Having a fully tunable material will enable digital MMs to be used to their maximum capability. In other words, once a digital MM is designed and fabricated, its functionality is permanent and unchanging. Because of this, its applications are limited. There is a need to fabricate different MMs for different purposes. It is, therefore, necessary to design multifunctionally MMs with the ability to be modified by means of tunable MMs.

1.2.1. Metamaterial's Beam Steering Application in THz region

THz beam steering has attracted a lot of attention due to its applications in radar, high-resolution imaging, and wireless communication (Fu et al., 2020). It is possible to steer beams in the microwave band through a technology called phased arrays. However, the high losses of semiconductor switches become a restriction when trying to apply this technology in the THz frequency range (Fu et al., 2020). Researchers are therefore looking for alternatives that perform better within this frequency range (Fu et al., 2020). As wireless technology advances, more people will utilize it, driving up demand for bandwidth. Therefore, it will be necessary to investigate suitable spectral areas for data communications. THz waves are drawing a lot of attention since they are high-frequency EM waves with a larger bandwidth than microwaves. During the last decade, recent developments have made it possible to use the THz band for communication. The EM spectrum's mmWave and THz frequency bands are not currently used for wireless communication (Akyildiz et al., 2018).

The fifth generation (5G) of cellular systems has officially adopted millimeter-wave communication systems with frequencies between 30 and 300 GHz (Akyildiz et al., 2018). They are not capable of supporting very high data rates like terabit per second due to their limited consecutive bandwidth of less than 10 GHz (Akyildiz et al., 2018). While the 5G network uses the mmWave band, the 6G network may use the THz band, which has a very wide bandwidth and very small antennas. Robotic surgery, eHealth, virtual and augmented reality, and autonomous driving all depend on 6G networks (Taghvaee et al., 2022). THz frequency bands are wireless frequencies that can provide a great deal of capacity. The capacity of these systems could be measured in terabits per second, which is higher than the capacity of millimeter-wave (mmW) systems (Elayan et al., 2018). Comparing the THz to microwave and optical communication systems, it is worth mentioning that THz communication systems are much more secure by contrast with millimeter signals, THz signals enable higher precision in the link directionality, and provide better security (Elayan et al., 2018). In addition to having a shorter propagation distance than optical communication, THz communication is less susceptible to light scattering, making it more difficult to detect and lastly, THz signals can be hidden in background noise (Fu et al., 2020). This range can have different applications, including wireless backhaul, access in small cell networks, and ultra-high speed indoor wireless links (Akyildiz et al., 2018). Although these waves can pass through non-line-of-sight places such as corners or obstructions (Elayan et al., 2018), they are less affected by fog, dust, and turbulence. Moreover, no additional noise creates from light sources or poses health risks (Elayan et al., 2018). THz's characteristics make it a promising technology for a variety of applications. However, as a disadvantage, in THz communications, some signals can be absorbed by the atmosphere. This limitation can also be considered as a benefit in short distances since the signal doesn't have to travel as far (Fu et al., 2020).

THz communications are essentially wireless signals broadcast at a specific frequency (Fu et al., 2020). Yet, the propagation loss is a significant obstacle to communication at mm-Wave and THz-band frequencies. This indicates that the strength of the signal weakens as it travels, which restricts how far a signal can reach. This phenomenon is related to Friis' law, which states that as frequency increases, the amount of signal that spreads out over distance increases, as well (Akyildiz et al., 2018). Furthermore, in the mm-wave and THz bands, some signal loss occurs due to interactions with air molecules (absorption loss). This path loss occurs because of the fact that a portion of the wave energy is converted into internal kinetic energy of the molecules in the propagation medium, mainly oxygen, and water vapor, respectively, at mm-wave and THz frequency bands (Akyildiz et al., 2018). As a result, depending on the signal distance, the signal experiences distinct peaks in strength known as spectral windows (Akyildiz et al., 2018). To develop a communication system based on THz, a great deal of effort must be devoted to researching and creating the necessary devices and tools. For future wireless communications with higher data rates, new spectral bands, and physical layer solutions are necessary. Current wireless networks have capacity limitations and spectrum scarcity and mm-Wave and THz can be explored to overcome those issues (Akyildiz et al., 2018).

Reconfigurable Intelligent Surfaces (RISs) have been used to build more reliable connections. RIS consists of several movable unit cells that can be used to control and shape the propagation of waves for faster and more reliable communication (Taghvaee et al., 2022). There are two methods for creating RISs: MSs and reflect arrays, with the latter having unit cells that are a lot farther apart than the former (Taghvaee et al., 2022). In order to maximize the capacity of networks, it may be beneficial to use RIS (reflection and scattering surfaces) technology. This benefit is provided by the internal MS/reflectarray of the RIS. The waves that are transmitted from the source at different frequency channels can be regulated using MS. Before the waves can travel to the receivers with enough strength, they will lose a lot of energy. MS/reflectarray will be required to address this problem (Taghvaee et al., 2022). RIS systems can provide amplitude and phase information in order to perform beam steering, beam splitting, collimation, and random scattering (Taghvaee et al., 2022). Due to their ability to alter the beam's angle, these technologies have the potential to increase the efficiency of the systems. As a result, many different fields of research and new technology are built on THz beam steering technologies.

1.3. Motivation

The goal of this thesis is to design, simulate, and fabricate two types of MS, one metal-based and the other with a tunable layer inside its structure for a potential application in THz communications. The metal-based MM and tunable MM have fabricated the two well-known structures of the checkerboard and stripe patterns, which are made of super unit cells capable of modifying normal incident THz waves and fabricating a THz beam splitting. The checkerboard pattern separates the normal incidence plane wave into four distinct beams, each of which has an equal oblique angle with respect to the z-axis. The striped pattern splits a plane wave that is normally incident into two beams that have identical deflection angles in proportion to the direction of the incident beam. According to the generalized Snell's law, these reflection angles depend on both the unit cell's size and the wavelength of the incident wave. So, by changing the periodicity or the size of the unit cell, one can adjust the reflection angle, as the properties of MM are determined by their geometries.

Vanadium dioxide (VO_2) has been used as our active material in this research in order to fabricate a VO_2-based MM structure. As a phase change material, VO_2 is a suitable candidate because it has near-room temperature phase change characteristics, making it a good candidate to use as an active material. It is possible to trigger the phase change of VO_2 using a variety of methods. Among them, the external laser technique is selected since it does not require changing the structure of the MMs as complex as triggering using an external electric field which needs complex structures or wire bonding. A novel structure of the hard-coded and VO_2-based MM was simulated, designed, and fabricated in this thesis. The structure employed in this thesis, i.e. dielectric substrate (sapphire) /metasurface (metal) /dielectric spacer (PET) / backplane (metal) is novel for this frequency range. To the best of our knowledge, PET has never been used as a spacer layer in any coded MMs beyond 300 GHz. To the best of our knowledge, there is no experimental VO_2-based MM research for the beam-splitting application in the THz range. There are three different topics discussed in Chapter 2, the basic explanation and phase-transition characteristics of vanadium dioxide and a review of literature on tunable coding MMs. Finally, there are some electromagnetic theory discussions of multilayer structures. In the 3rd Chapter, the specifics of the experiments and the different methods used to characterize the samples are outlined. There is a discussion in Chapter 4 about the temperature dependence of the VO_2 and the result of manipulating waves and THz transmission characterization. In Chapter 5, the MM design, simulation, fabrication process, and then measurement results are discussed. In Chapter 6, the thesis summary and conclusion are written.

CHAPTER 2

BACKGROUND

This chapter provides background information on the phase transition of vanadium dioxide and its modulation techniques, followed by some of VO_2's theoretical concepts. The current chapter also includes a review of the literature on waveform modulators and tunable coding MMs. The final section describes the multilayer structure's underlying theory.

2.1. Vanadium Dioxide

Vanadium dioxide (VO_2) is one of several transition metal oxide compounds that exhibit metal-insulator transitions (MIT) close to room temperature ($T_{MIT} \sim 340$ K in bulk). VO_2 was selected as the active layer in MM since it exhibits metal-insulator transition (MIT) that is accompanied by structural phase transition (Liu et al., 2018). Its critical temperature is approximately 68°C. Above this temperature, it has a tetragonal (rutile) structure, while below it, it has a monoclinic structure (Liu et al., 2018). Along with the structural transition, a significant transition in electronic conductivity occurs as a consequence of changes in the band structure of the VO_2 (Lu et al., 2021).

VO_2 exhibits metal-to-insulator transitions when exposed to heat, and this was found in 1959 by Morin, F.J. (Wang et al., 2019).

It is estimated that there are approximately 20 stable vanadium oxide compounds, out of which three demonstrate insulator (or semiconductor)-to-metal transition behavior (Krammer et al., 2016). These compounds include VO_2, V_2O_3, and V_2O_5, whose transition occurs at different critical temperature (T_C = 68°C for VO_2, T_C = -123°C for V_2O_3, and T_C = 257°C for V_2O_5) (Krammer et al., 2016; Pergament et al., 2013). VO_2 has astonishing properties of MIT about 68°C (near room temperature) in comparison with other oxides of vanadium. Due to this characteristic, VO_2 has been the subject of extensive experimental and theoretical studies. At the transition temperature, there is a significant drop in the resistivity of VO_2. The metallic phase of the VO_2 can be seen at temperatures over the transition temperature, whereas the insulator phase can be seen at temperatures below the transition temperature. In spite of the controversy surrounding the

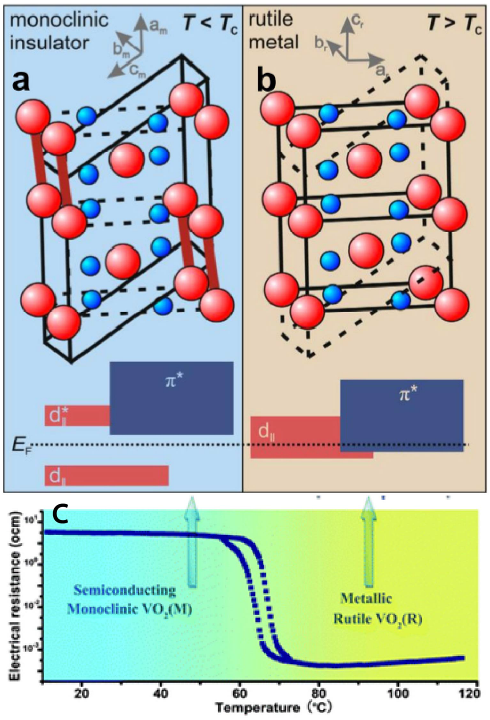

Figure 2.1. a and b) An illustration comparing insulating monoclinic, and metallic rutile VO_2. Crystallographic structures and solid lines indicate unit cells. The red balls represent vanadium atoms, and the blue balls represent oxygen atoms. An illustration of the VO_2 electronic band structure near the Fermi level is shown at the bottom (Wegkamp and Stähler, 2015). c) Reversible phase transitions and the temperature dependence of resistivity (Wu et al., 2013).

VO_2 phase transition mechanism, scientists have made excellent achievements in knowing how the MIT mechanism works in recent decades. Understanding what causes MIT will allow researchers to have control over its modulation as well. There are two well-known theory explanations of the MIT behavior of the VO_2: structural-based Peierls transition mechanism and Mott-Hubbard electron correlation mechanism. The first one is based on the changing in lattice symmetry and the latter is based on the electronic transition. The Peierls and Mott transition of the VO_2 phase change transition has been explained by Shao et al review paper. Below is a summary of their discussion:

As it is shown in Figure 2.1, crystal parameters change during phase transition, causing the V atom to deviate from the vertex angle. This results in a monoclinic crystal structure with low symmetry, and it is then possible to form V-V bonds with varying lengths. The formation of a V-V dimer directly results in the transition from a delocalized to a localized state. Theoretically, Rudolf Peierls, in the 1930s, proposed that 1D conductors are composed of atoms with equal spacing (the lattice constant (a)), each carrying a conduction electron. This 1D system is unstable due to electron interactions with the lattice, leading to lattice distortion at low temperatures at pairs of atoms. When the modulation wave vector is q = 2k (k is the Fermi wave vector), the Fermi surface and the Brillouin zone boundary are completely nested. The energy of the entire electronic lattice system is lowered in this situation, which causes the transition from a conductor to an insulator. This occurs since the amount of energy lost when the band gap widens up is greater than the elasticity of the distortion in the lattice. According to the Mott-Hubbard mechanism, which is explained using band theory, MIT phase transition is accompanied by a change in the band structure. A metallic behavior can be determined by its Fermi level, which falls between the π^* and $d_{||}$ bands of its phase band structure. However, in lower temperatures, while VO_2 is in its monoclinic band structure, an energy band is split into two energy bands ($d_{||}$ band and $d_{||}^*$ band), and a forbidden band is formed between the $d_{||}$ band and the π^* band. VO_2 is the insulation phase because its Fermi level drops within the forbidden band of approximately 0.7 eV (Shao et al., 2018).

Phases of VO_2 can include both insulation monoclinic (M1) and conductive rutile (R), but there can also be intermediate insulating phases such as M2, M3 (monoclinic), and T (triclinic). These vanadium phases can occur under pressure or lattice strain depending on conditions (Otto et al., 2019). The most significant phase of these intermediate states is M2, where half of the vanadium chains dimerize (Lu et al., 2021). Raman spectroscopy can be used to distinguish between the various phases of VO_2 (Shi et al., 2021). There are two problems with the Peierls mechanism: it cannot explain the rather large 0.6 eV band gap of VO_2 in the monoclinic phase, and also it cannot account for the emergence of the intermediate phase of the VO_2 (Aetukuri et al., 2013; Shao et al., 2018). In accordance with the Mott-Hubord mechanism, lattice distortion is responsible for the MIT, but it appears that structural distortion does not appear to be the only factor responsible for phase change of metal/insulator, nor is it mandatory (Shao et al., 2018). Mott's theory can't explain the discovery of other phases (M2, M3, and T) at low temperatures (Aetukuri et al., 2013; Shao et al., 2018). Using modern numerical techniques, namely density function theory (DFT), understanding VO_2 phase change has progressed significantly. Wentzcovitch's DFT (LDA) approximation in the 1990s, found minimum energy for a structure that is very similar to the M1 phase, and they failed to open a gap in their simulations (by -0.004 eV) (Tiwari, 2015). As a result, they were unable to predict the gap in the M1 phase and could not adequately discuss the insulating behavior of the M2 phase (Tiwari, 2015).

Despite the above explanations, until now the exact reason VO_2 transition has not been clarified.

2.1.1. VO_2 Conductivity

To explain the tunability properties of the VO_2, it is necessary to understand how changes in the conductivity of the film lead to changes in the reflection phase. It is necessary to study the optical properties of the VO_2 in order to understand its conductivity.

2.1.2. Drude Model

It is possible to calculate the dielectric function of the metallic phase of the VO_2 using the classical Drude's model.

$$\varepsilon_m(\omega) = \varepsilon_\infty + i\frac{\omega_p^2}{\omega(\omega + \frac{i}{\tau})} \tag{2.1}$$

In which, ε_∞ is the dielectric constant at VO_2 insulating mode. VO_2 is transparent for the THz wave in the insulating phase. The Drude model assumes that $\varepsilon_\infty = \varepsilon_{insulating}$ which is equal to 9. At Eq. 2.1, τ is relaxation time and it is proportional to the carrier mobility of the film (μ= 2 $cm^2/V.s$) and effective mass of the electron and inversely changes by electron charge, $\omega_p^2 = \frac{Ne^2}{2\varepsilon_0 m_e}$ is the plasma frequency which is related to carrier density N=8.7×10^{21} cm^{-3} (Fan et al., 2012). $\omega=2\pi\nu$ is the cyclic frequency (Jepsen et al., 2006). The following formula which is obtained using the Drude model, gives the DC conductivity of a material can be written as follow (Jepsen et al., 2006):

$$\sigma_{dc} = \frac{Ne^2}{m_e}\tau \tag{2.2}$$

Where, N stands for carrier density, e electron charge, m_e electron mass, and τ mean collision rate which describes loss in conductors, and it is the reciprocal of damping rate. Since DC conductivity is a characteristic behavior of a material, its value is independent of the applied electric field. AC conductivity of a material can be written as (Jepsen et al., 2006):

$$\sigma_\omega = \frac{\sigma_{dc}}{1 - i\omega\tau} \tag{2.3}$$

Drude's model, can not be used to explain the intermediate phase of the VO_2. The VO_2 phase transition process can be explained using Effective Medium Theories (EMT). There are two types of EMTs that are commonly used to explain the phase transition process using the effective dielectric function (Jepsen et al., 2006).

2.1.3. Effective Medium Theories

VO_2 films undergo phase transitions when conductive domains form (Figure 2.2). The effective-medium theory describes the relationship between the local microscopic and macroscopic dielectric functions in a spatially inhomogeneous thin film. The most popular explanations of the effective dielectric function are the Bruggeman and Maxwell-Garnett EMTs (Jepsen et al., 2006).

2.1.3.1. Maxwell-Garnett EMT

VO_2 exhibits hysteresis behaviour when subjected to heat modulation. In 2018 a research group modified the Maxwell Garnett effective medium model in order to explain the hysteresis behavior of the VO_2.

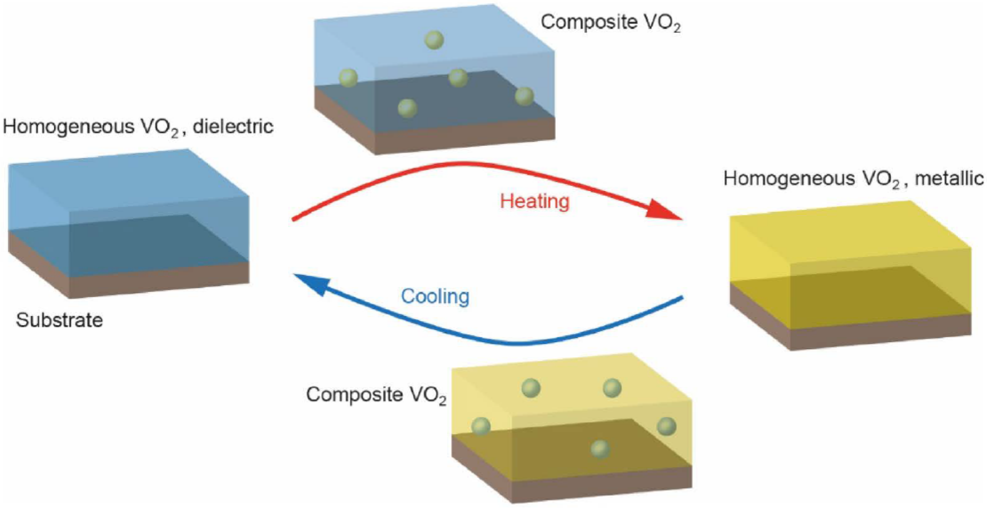

Figure 2.2. The idea of hysteresis is depicted as an asymmetrical structural change. To demonstrate, a thin layer of VO_2 is fabricated on a substrate. There are considerable structural variations between the two states when temperatures are raised and cooled. The embedded spheres approximate the growth of one phase inside another in a complicated, inhomogeneous manner (Frame et al., 2018).

This model assumes the formation of dielectric islands within metallic host structures (Figure 2.2) instead of the previous Maxwell Garnett EFT, which introduces a single effective permittivity for the phase change materials. In the modified model the effective permittivity is separated into two independent equations; Effective permittivity for heating and cooling are separated. As they explain, in their theory, the filling fraction f is regarded as the metallic phase volume fraction. It can be stated that when f equals 0, VO_2 is in its pure dielectric phase, whereas, when f equals 1, VO_2 is in its pure metallic phase. The effective permittivity of heating is not the same as the effective permittivity of cooling (Frame et al., 2018).

$$\varepsilon_{eff,h} = \varepsilon_i \frac{\varepsilon_m(1+2f) + \varepsilon_i(2-2f)}{\varepsilon_m(1-f) + \varepsilon_i(2+f)} \tag{2.4}$$

$$\varepsilon_{eff,c} = \varepsilon_m \frac{\varepsilon_m * 2f + \varepsilon_i(3-2f)}{\varepsilon_m(3-f) + \varepsilon_i * f} \tag{2.5}$$

$$\varepsilon_{eff,h} \neq \varepsilon_{eff,c} \tag{2.6}$$

Where ε_m and ε_i are the metallic phase and insulator phase permittivity of the VO_2. The Maxwell-Garnett EMT is anticipated to be valid at low volume fractions f since it assumes the conductive domains are spatially separated (Jepsen et al., 2006).

2.1.3.2. Bruggeman EMT

In the MIT process, VO_2 undergoes a great change in resistivity, causing a 10^4 order increase in conductivity at the same time. The conductivity of metallic VO_2 is derived using the Drude model (Eq. 2.1), and the effective medium theory (Bruggeman) is applied to the intermediate states of the VO_2 (Fan et al., 2012). One can determine the dielectric function of the metallic phase of the VO_2 using the Drude model and insert it into EMT's effective dielectric constant. However, Eq. 2.2 indicates that both VO_2 phases (insulating and metallic) were present at the intermediate temperatures. Brugemann's effective medium theory can be applied to the intermediate phases.

$$\varepsilon_{eff} = \frac{1}{4}\{\varepsilon_i(2-3f) + \varepsilon_m(3f-1) + \sqrt{[\varepsilon_i(2-3f) + \varepsilon_m(3f-1)]^2 + 8\varepsilon_i\varepsilon_m} \tag{2.7}$$

$$f = 1 - \frac{1}{1 + \exp[(T - T_0)/ \bigtriangleup T]} \tag{2.8}$$

In which, ε_i and ε_m are dielectric constants of the insulating and metallic phase of the VO_2, respectively, f filling fraction which is $0 < f < 1$ and ΔT is the hysteresis width (Fan et al., 2012). In this study T_0= 74 °C for heating graph and T_0= 68 °C for cooling is used. Using the mentioned values, the conductivity of the VO_2 will be obtained (Jiu-sheng et al., 2020)

$$\sigma = -i\varepsilon_0\omega(\varepsilon_{eff} - 1) \tag{2.9}$$

The conductivity of the VO_2 was obtained for 0.1 THz using Eq.2.9. With regard to these two EMT models: According to Jepsen et al., the Maxwell-Garnett EMT considers the conductive zones to be spatially separated. Because of this premise, the theory is applicable to low-volume fractions f. The volume fraction of the conductive domains is large enough to create a continuous conducting channel throughout the sample, and the Bruggeman EMT appropriately predicts percolation behavior. Several characteristics of the MIT transition of VO_2 were described using this model (Jepsen et al., 2006).

There is a direct correlation between the thermal hysteresis of thin films of VO_2 and both the grain size distribution as well as the temperature. Various grain sizes have different stoichiometry, which means their oxygen vacancy concentrations differ according to their size. Since these defects possess donor properties, they can play an important role in broadening phase transitions, due to the fact that they are able to provide an abundance of free electrons (Liu et al., 2006).

2.2. VO_2 Application in THz Region as Conventional MMs and as Coding MMs

2.2.1. Conventional Metamaterials

VO_2 was used on a dielectric substrate by Jepsen et al. for THz applications. According to their research, VO_2 on the dielectric substrate passes THz radiation below T_c, so its conductivity should be low, and it should be an insulator. Above T_c, though, it reflects THz radiation, so the state of the VO_2 must be metallic (Jepsen et al., 2006). Jepsen et al investigated the phase and amplitude of the transmission of a broadband THz signal through a VO_2 thin film on a dielectric substrate by terahertz time-domain spectroscopy (Figure 2.3(a)). To avoid water vapor absorption by signal, the THz beam was ejected through a dry nitrogen medium. To control the sample temperature, the entire mount and sample were isolated from the surrounding medium using a thick layer (Figure 2.3(b)). Optical characteristics of the VO_2 thin film between 25°C-100°C was investigated. The

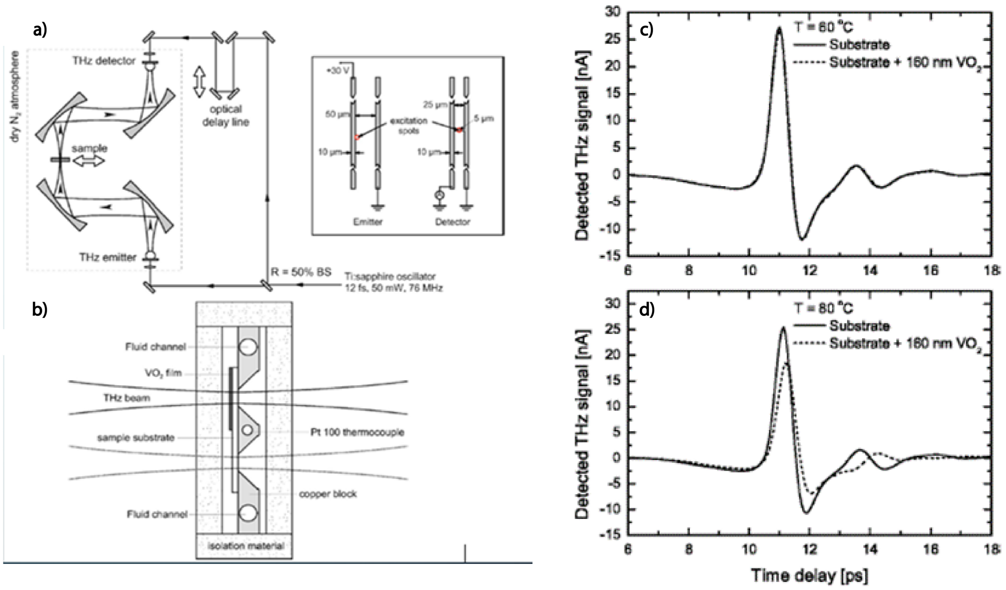

Figure 2.3. a) Time-domain terahertz spectroscopy experimental setup (THz-TDS). b) A detailed view of the thermally isolated sample platform. c) THz signal transmission at 60°C. d) THz signal transmission at 80°C. (Jepsen et al., 2006).

THz signal transmitted from the thin film layer to the substrate at various temperatures was compared to the same THz signal traveling through the pure dielectric substrate and the result is illustrated in Figure 2.3(c and d). The result showed that in higher temperatures the film is in its metallic state therefore the amplitude decreases as some part of the beam was reflected. Figure 2.3(c and d) is comparing the transmission of THz signals from the bare substrate and VO_2 film at a temperature of 60°C and 80°C (Jepsen et al., 2006).

Zhang et al. have used the VO_2 in switching mode. In their study (Zhang et al., 2019), they investigated the VO_2-embedded hybrid MM consisted of the cell of two metal structures connected by VO_2 pads (Figure 2.4). The research consists of simulation using electromagnetic field computational software and commercial software CST Microwave Studio and using the MIT transition of VO_2. They have shown experimentally that the mode-switching phenomenon in this MM occurs using thermal, electrical, and optical stimuli by traditional THz TDS. In their studies, they compared different stimulation techniques and discovered that thermal and electrical stimulation had the same physical reason for phase change, but optical stimulation had a different reason. For thermal and electrical stimuli, the phase transition is caused by Joule heat, and the speed of an electrical stimulus depends on the film's thermal response time. For the optical stimuli, phase transitions are

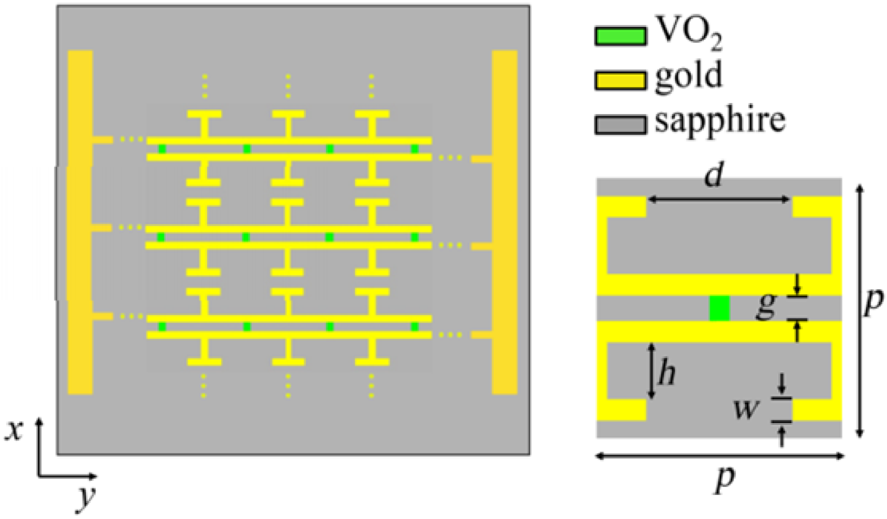

Figure 2.4. Left: Illustration of an embedded MM with VO$_2$ film of 200 nm thickness (green color). Right: Geometric parameters of the unit cell of the MM, (p = 110 µm), (g = 10 µm), (w = 8 µm), (d = 60 µm), (h = 22 µm) (Zhang et al., 2019).

caused by Mott-Peierls phase transitions and are not just pure thermal phenomena so it leads to a faster (order of ps) transition (Zhang et al., 2019). In their research, it is shown that when the VO$_2$ thin film conductivity changes from the higher level to the lower state, resonant mode switching take place.

2.2.2. Coding Metamaterial

A new concept of ”coding MMs”, which is based on coding control, was proposed by Della Giovampaola et al and Cui et al in 2014. Cui et al demonstrated coding MMs using two different unit cells consisting of the same structures but different widths, in which response to the signal in two different phases 0 and π (the maximum phase difference in binary case is in order of π) (Figure 2.5(b). Binary representation in coding mode could be shown as 0 and 1-bit unit cells. In their study, they have shown that if the width of the unit cell is 4.8 mm indicates 0-bit unit cells in digital mode with a 0 phase response, and the width of 3.75 mm indicates a 1-bit unit cell with π response to the signal (Cui et al., 2014). In order to digitally control their MMs, they have designed a novel MM cell as illustrated in Figure 2.6. This unique subwavelength size MM cell can be controlled by ”0” and ”1” unit cells using a biased diode. They have demonstrated that when the biased voltage is about 3.3 V, the diode is ON and corresponds to a ”1” element, when the diode is OFF, functions as a ”0” element (no biased voltage), in the CST software and the phase difference is 180° between 8.3 and 8.9 GHz and at 8.6 GHz, the phase difference is exactly 180° (Figure 2.6).

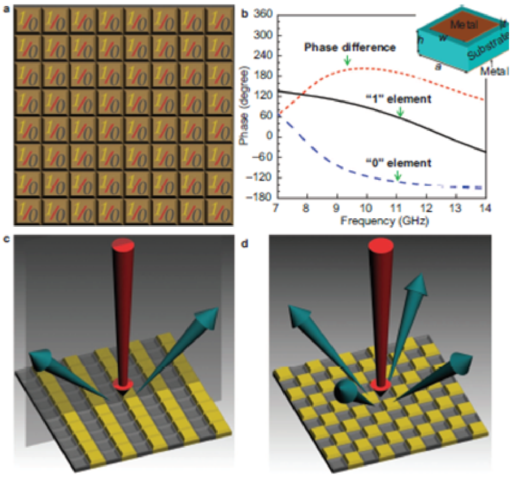

Figure 2.5. The 1-bit coding MS. a) The ”0” and ”1” coding unit cells. b) The unit cell structure and the phase responses of 0 and 1-bit at various frequencies. (c,d) Scattering pattern of the checkerboard and stripe designs (Cui et al., 2014).

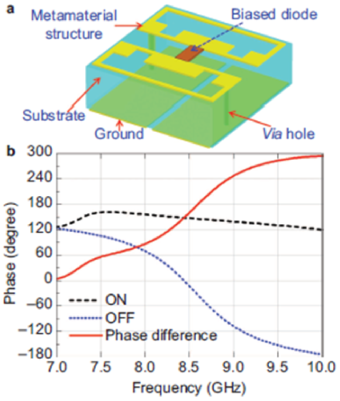

Figure 2.6. a) The diode structure. b) The equivalent phase responses of the biased diode as the MM unit cell are ’OFF’ and ’ON’(Cui et al., 2014).

Moccia et al illustrates the application of coding MM in the THz range in great detail (Moccia et al., 2017) (Figure 2.7).

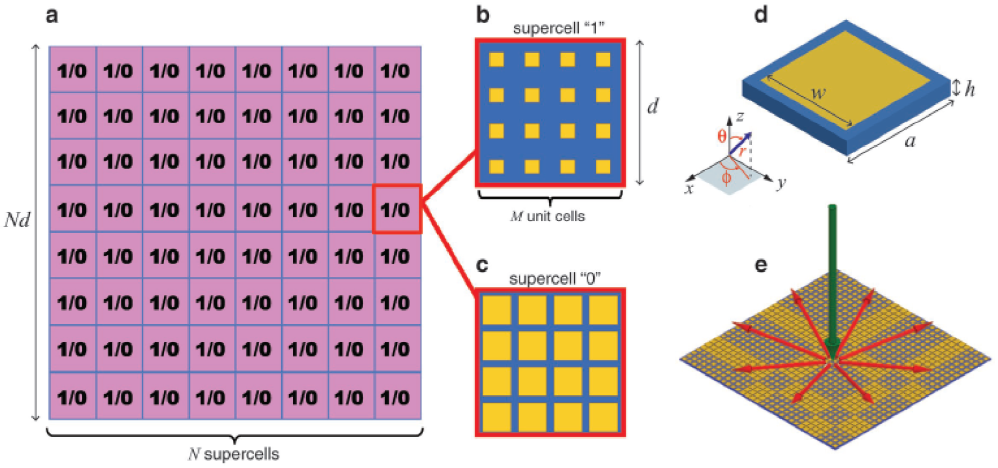

Figure 2.7. A diagram showing the concept and geometry of a) Binary coding MM, b) The 1-bit super unit cell, c) The 0-bit super unit cell, d) Unit cell geometry, e) Diagram of diffuse scattering (Moccia et al., 2017).

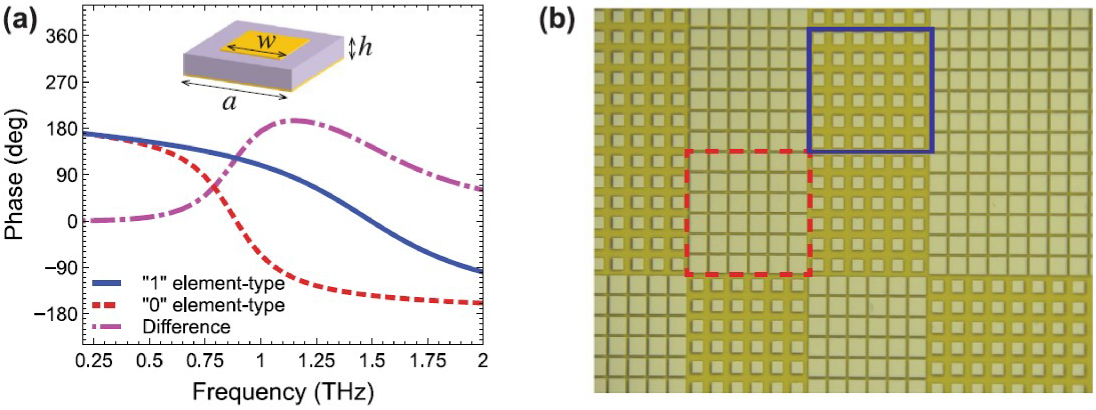

Figure 2.8. The phase graph and super unit cell structure. a) The ’0’ and ’1’ unit cells, as well as their phase responses at various frequencies, were realized in metallic square patch units (the 180° phase difference between the unit cell obtained at 1 THz). b) The blue-solid and red-dashed squares in the optical microscope image identify the 6×6 super cells belonging to the ’1’ and ’0’ unit cell types, respectively (Moccia et al., 2017).

As stated earlier (Figure 2.5), this group designed unit cells with a 180° degree phase difference between them. The only distinction between these two unit cells is the length of the metal patch. They designed this MM to diffuse scattering (Figure 2.7), such that the plane wave that is normally incident is scattered uniformly in all directions. It is often used in beam steering coding MM by implementing super unit cells designs (Figure 2.8) (Cui et al., 2014; Liu et al., 2016; Moccia et al., 2017). The super unit cell simulates periodic boundary conditions and reduces EM coupling between unit cells with different geometrical features (Liu et al., 2016).

2.2.3. Principle of Deflection Angle Calculation

The MM and light interaction follows the generalized Snell's law (Yu et al., 2011). If the phase difference along the interface is intended to be constant, and the interface has a phase discontinuity, Eq. 2.10 can be used.

$$n_t sin\theta_t - n_i sin\theta_i = \frac{\lambda_0}{2\pi}\frac{d\phi}{dx} \tag{2.10}$$

where θ_i is the incidence angle, θ_t refraction angle, n_i and n_t are the refractive indices of the two medium, λ_0 is the vacuum wavelength, $\frac{d\phi}{dx}$ is the the phase gradient along the interface.

As the super unit cell was used in this structure, the qualitative calculations of far-field scattering were used to obtain the deviated reflection angle of this structure. Considering the MM as a perfect reflection (Liu et al., 2016), Liu et al, calculate the scattering pattern of the MM by assuming the reflected amplitude is unity. The electric field on the MM is then assumed to be $E_{m,n}(x', y') = e^{i\varphi(m,n)}$. Following is the scattering pattern of the coding unit cells (Liu et al., 2016).

$$E = \sum_{m=-\frac{M}{2}}^{\frac{M}{2}} \sum_{n=-\frac{N}{2}}^{\frac{N}{2}} E_{m,n}(x', y')\; F(\theta, \varphi) \tag{2.11}$$

Since it is well known that the radiation of each unit cell traverses a different distance to reach the point of interest, the individual unit cells of the array have a phase difference among themselves. In these calculations, these phase discrepancies are considered zero. Under the normal incidence of plane waves the array factor can be written as follows (Liu et al., 2016):

$$F(\theta,\varphi) = f_e(\theta,\varphi)\sum_{m=1}^{M} e^{-j(k_0(m-1/2)d_x \sin\theta\cos\varphi + m\pi)} \sum_{n=1}^{N} e^{-j(k_0(n-1/2)d_y \sin\theta\sin\varphi + n\pi)} \tag{2.12}$$

Where $\sin\theta cos\varphi$ and $\sin\theta sin\varphi$ are the direction with respect to the x-axis and y-axis, respectively. Digital components interfere destructively with each other, eliminating the pattern function $f_e(\theta,\varphi)$ of the (Jiu-Sheng et al., 2017). The array factor should be maximized to obtain the maximum radiation in space (Collin, 1987; Cui et al., 2014; Liu et al., 2016). By maximizing the array factor, to obtain the anomalous reflection beam, θ and ϕ are obtained as:

$$\theta = arcsin(\lambda\sqrt{(\frac{1}{\Gamma_x^2}+\frac{1}{\Gamma_y^2})} \tag{2.13}$$

$$\varphi = \pm\arctan(\frac{\Gamma_x}{\Gamma_y}) \tag{2.14}$$

$$\varphi = \pi \pm \arctan(\frac{\Gamma_x}{\Gamma_y}) \tag{2.15}$$

in which Γ is the periodicity along the x and y directions. The Eq. 2.13, 2.14, 2.15 show that the reflected angle can be customized under normal incidence by varying the periodicity of the MM means a geometrical property. There are two patterns used in this thesis for splitting the THz beam: stripe pattern and checkerboard pattern. The patterns are constructed from 10×10 super unit cells with 8×8 unit cells within each. There is a 16×d periodicity in each pattern, where every unit cell has a periodicity of d.

For the stripe pattern the periodicity along the y-direction is infinity and along the x-direction is 16d. Then, the azimuth and elevation angle can be obtained as: $\phi = 0$ and $\phi = \pi$ and

$$\theta = arcsin(\frac{\lambda}{\Gamma_x}) = arcsin(\frac{\lambda}{16d}) \tag{2.16}$$

For the checkerboarded pattern, the periodicity along the x-direction is equal to the periodicity along the y-direction, then the result will be:

$\phi = \pm\frac{\pi}{4}$ and $\phi = \pm\frac{3\pi}{4}$ and

$$\theta = arcsin(\lambda\sqrt{\frac{2}{\Gamma^2}}) = arcsin(\frac{\sqrt{2}\lambda}{16d}) \tag{2.17}$$

In summary, unlike conventional MM which is characterized by sophisticated effective medium theory, the coding MM requires only the phase of reflection in the unit cell and system design. Creating a coding MM can be achieved by designing a unit cell, changing a physical parameter, and designing another unit cell with a 180° phase difference and with approximately identical reflection amplitude. Consequently, a 1-bit coding MM can be created by assembling these unit cells in a precise pattern (Figure 2.5(b)). The coding MM makes it easy to tailor the far-field scattering pattern, as explained in Chapter 5. The following section will provide a brief description of a few papers that employ the coding MM. Jiu-Sheng. L, (2020) claimed that the first active control of programmable coding MSs was demonstrated at the THz regime by their group using VO_2 (VO_2) embedded metallic patch (Figure 2.9). They showed at room temperature when the VO_2 is in an insulator state, the different phase between two adjacent coding meta-particles is 180° and the normal incident THz beam is reflected into two symmetric main projected directions with a certain angle.

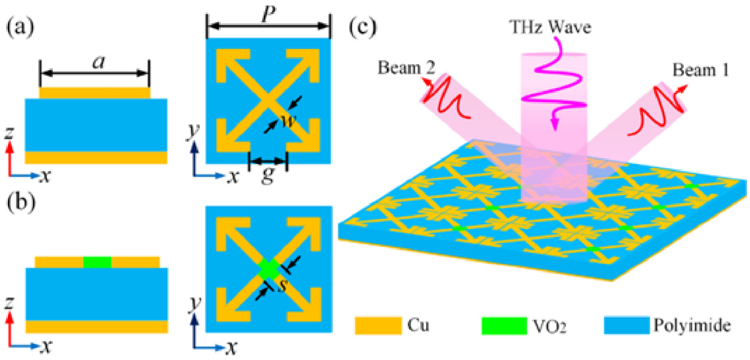

Figure 2.9. a) An illustration of the conventional coding unit cell (coding unit cell ’0’). b) tunable coding unit cell embedded with VO_2 film (coding unit cell ’1’). c) Under normal illumination, the coding unit cell will show two symmetrical directions of normal incidence. Geometric parameters of coding unit cell (p = 110 µm), (g = 40 µm), (w = 6 µm), (a = 80 µm), (s = 20 µm) (Jiu-sheng et al., 2020).

In the metallic state (68°C and upper temperatures), the phase difference between two adjacent coding meta-particle becomes 0 degrees and there will be just a single reflection beam. In coding MSs, the function is typically achieved by designing two unit cells with ”0” and ”π” phase responses to present ”0” and ”1” digital states (Figure 2.10). The phase difference between the VO_2 embedded unit cell and higher conductivity from 0.7 THz to 1.3 THz is approximately ”π” (Figure 2.10(c)), which is a necessary condition for a ”1”-bit coding MS. In conclusion, they have shown by changing the actual temperature of this structure and design they are able to control the reflected THz waves without applying any changes in the MM cell structure.

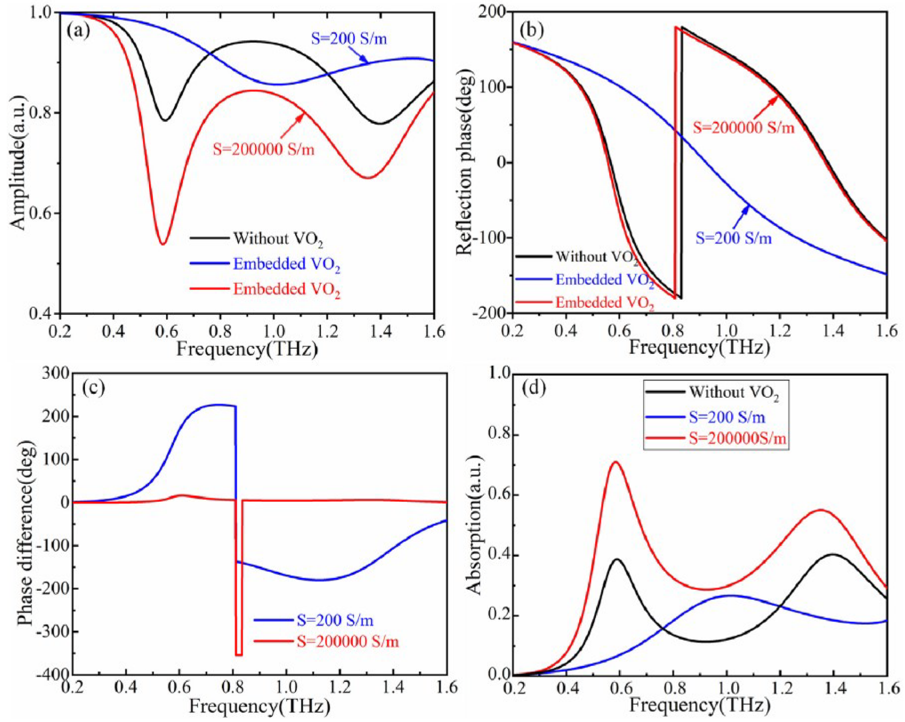

Figure 2.10. a) Reflection amplitude of the unit cells. b) Reflection phase of the unit cells. c) Phase difference between the ”0” and ”1” bit unit cells. d) The absorption amplitude of the unit cells in THz range (Jiu-sheng et al., 2020).

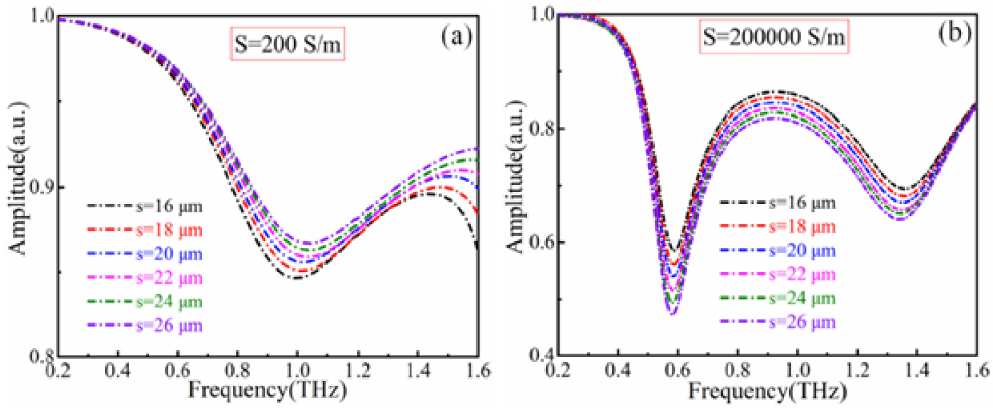

Figure 2.11. Measurement of composite structure reflection amplitude at different values of s. a) 200 S/m (room temperature). b) 200 000 S/m (68°C) (Jiu-sheng et al., 2020).

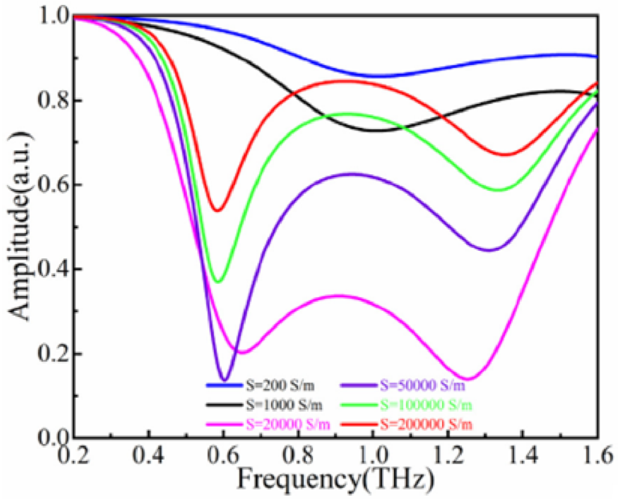

Figure 2.12. Different reflection amplitudes of VO_2 results of different conductivity values (Jiu-sheng et al., 2020).

The reflection amplitudes between the 0 and 1-bit unit cells are quite near to each other from 0.7 THz to 1.3 THz, as seen in Figure 2.10(a). In Figure 2.9 tunable coding MSs has shown in terahertz region using VO_2 embedded metallic patch (Jiu-sheng et al., 2020). The reflection amplitude of the composite structure in different values of s is also measured in various conductivity and Figure 2.11 represents the physical parameter s, does not have much impact on the reflection of the amplitude in different conductive modes of the VO_2. However, the reflection amplitude changes are directly connected to the conductivity of the VO_2 (Figure 2.12). In the insulating state, VO_2 is transparent in the exposure of the THz signal and as the conductivity of the VO_2 increases, the thin film turns to behave as a metal then, the reflection amplitude changes proportionally by operating temperature.

2.3. Basic Theory

2.3.1. Study of Electromagnetism in Nonconducting Medium

In order to understand the response of the material to the incoming electromagnetic wave, a thorough study of electromagnetism in the nonconducting medium is required. By remembering Maxwell's equation (Jackson, 1999)

$$\nabla \cdot \mathbf{D} = 0 \tag{2.18}$$

$$\nabla \cdot \mathbf{B} = 0 \tag{2.19}$$

$$\frac{\partial \mathbf{B}}{\partial t} = -\nabla \times \mathbf{E} \tag{2.20}$$

$$\frac{\partial \mathbf{D}}{\partial t} = \nabla \times \mathbf{H} \tag{2.21}$$

and plane wave solution for $e^{-i\omega t}$, traveling in x direction:

$$\mathbf{E}(\mathbf{x}, t) = \mathbf{E_0} e^{i(kx - \omega t)} \tag{2.22}$$

$$\mathbf{B}(\mathbf{x}, t) = \mathbf{B_0} e^{i(kx - \omega t)} \tag{2.23}$$

Where k is the wave number:

$$k = \omega \sqrt{\varepsilon \mu} \tag{2.24}$$

The phase velocity of the plane wave can be written as:

$$v = \frac{\omega}{k} = \frac{1}{\sqrt{\varepsilon \mu}} = \frac{c}{n} \tag{2.25}$$

Then the refractive index will be obtained as (Rout and Sonkusale, 2017):

$$n = \sqrt{\varepsilon\left(\omega\right) \mu(\omega)} \tag{2.26}$$

Materials with negative values of permeability and permittivity are also called left-handed materials. Such materials have the Poyinting S vector anti-parallel to the wave vector k. The electric permittivity ε and magnetic permeability μ of a material can be used to describe optical property of the material (Shin et al., 2022). When light incidents on a surface of a transparent material, it splits into three parts: one part reflects back, another transmits into the material and the third is absorbed by the material. In the interface between different optical media, the transmission wave (T) and reflection wave (R) are described by the Fresnel coefficient. The wave's polarization depends on the incident angle on the surface and on the reflection plane. Parallel polarization (P-polarization) or Transverse Magnetic (TM), where the electric field of the incident wave is parallel to the plane of reflection, and perpendicular polarization (S-polarization) or Transverse Electric (TE), where the electric field is perpendicular to the plane of reflection.

Boundary conditions for the optical medium interface are derived from the integral versions of Maxwell's equations. Boundary conditions are described as (Jackson, 1999):

$$\epsilon_1 E_1^{\perp} = \epsilon_2 E_2^{\perp} \tag{2.27}$$

$$B_1^{\perp} = B_2^{\perp} \tag{2.28}$$

$$E_1^{||} = E_2^{||} \tag{2.29}$$

$$\frac{B_1^{||}}{\mu_1} = \frac{B_2^{||}}{\mu_2} \tag{2.30}$$

in which subscripts 1 and 2 are referred to the different optical mediums. By considering the monochromatic plane wave

$$\vec{\mathrm{E}}(\vec{\mathrm{r}},\mathrm{t}) = \vec{\mathrm{E}}_{0,i}\exp(i[\vec{\mathrm{k}_i}\cdot\vec{\mathrm{r}} - \omega_i \mathrm{t}]) \tag{2.31}$$

and the continuity of the perpendicular components of the magnetic field (Eq. 2.28), and having the fact that the ratio of the electric field to the magnetic field in free space is equal to the speed of light $\frac{E}{B} = c = \frac{\omega}{k}$, one can obtain the reflection law and Snell's law of refraction:

$$\theta_i = \theta_r \tag{2.32}$$

$$n_1 \sin\theta_1 = n_2 \sin\theta_2 \tag{2.33}$$

By considering i and r, and t refer to the incident, reflecting and transmitting wave, respectively, and s and p for the s- polarization and p-polarization, and using the Eqs. 2.28, 2.29, and 2.30, Fresnel coefficients which provide a relationship between incident amplitude, transmitted amplitude, and reflected amplitude and can be used to determine how much of the wave is reflected or refracted are expressed as follows (Born and Wolf, 2013):

$$r^s = \frac{E_r^s}{E_i^s} = \frac{n_i cos\theta_i - n_t cos\theta_t}{n_i cos\theta_i + n_t cos\theta_t} \tag{2.34}$$

$$t^s = \frac{E_t^s}{E_i^s} = \frac{2 n_i cos\theta_i}{n_i cos\theta_i + n_t cos\theta_t} \tag{2.35}$$

$$r^p = \frac{E_r^p}{E_i^p} = \frac{n_t cos\theta_i - n_i cos\theta_t}{n_t cos\theta_i + n_i cos\theta_t} \tag{2.36}$$

$$t^p = \frac{E_t^p}{E_i^p} = \frac{2 n_i cos\theta_i}{n_t cos\theta_i + n_i cos\theta_t} \tag{2.37}$$

The refraction index n is:

$$n = \frac{c}{v} = \frac{k}{\omega}c \tag{2.38}$$

2.3.2. Fringe or etalon (Fabry-Perot cavity)

Waves are superimposed by repeated reflections at the inner film boundaries of parallel surfaces, which causes fringes or etalon characteristics to appear in the transmittance spectrum of films (Schade et al., 2020).

Consider a multilayer structure (Figure 2.13), where each layer's intersection has multibeam reflections. As the beam emerges from the spacer, it will obtain a phase and a reflecting coefficient r, which can be determined using Fresnel equations. The original transmitted wave is multiplied by r^2e^{i2kt} every time the beam enters a spacer, then reflects from the interference of the spacer and M2 and then reflects again from M1 and then passes from M2 (Pedrotti et al., 2017). For a multilayer structure, the total transmitted (or reflected) wave must be obtained by adding all the transmitted waves (or reflection waves). After summing up all the transmitted (reflected) beams, and after a few calculations and using the trigonometry identity and stokes relations, one gets the total transmission and total reflections intensity of the structure (Pedrotti et al., 2017):

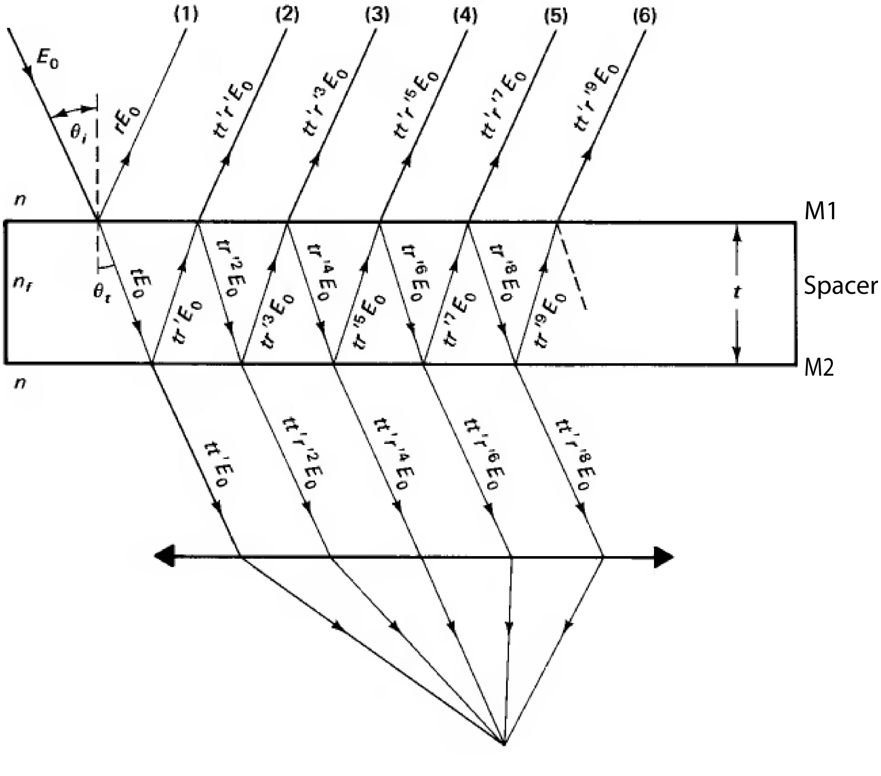

Figure 2.13. Fabry-Perot cavity contains a multiple beam interference in a parallel surface (Pedrotti et al., 2017).

$$I_{transmitted} = \frac{(1-r^2)^2}{1+r^4-2r^2\cos(kt)}I_i \tag{2.39}$$

This equation can be written as:

$$I_{transmitted} = \frac{I_0}{1+F\sin^2\frac{kt}{2}} \tag{2.40}$$

Where F is defined as the finesse coefficient:

$$F = \left(\frac{2r}{1-r^2}\right)^2 \xrightarrow{R=r^2} F = \frac{4R}{(1-R)^2} \tag{2.41}$$

I_i is the radiation intensity of the incident beam. r is the Fresnel's reflection coefficient of the metal, k stands for the wavenumber and t is the thickness of the spacer. Similar for obtaining the total reflection intensity: each ray, which reflects from the region 1 and spacer interference of the structure, has got a factor of the $r\prime^2$ and the total reflected field, is the summation of the individual reflected beams. The result will be:

$$I_{reflected} = \frac{2r^2(1-\cos(kt))}{1+r^4-2r^2\cos(kt)} I_i \tag{2.42}$$

Writing using the finesse coefficient the total reflection can be obtained as:

$$I_{reflected} = \frac{F \sin^2\frac{kt}{2}}{1+F\sin^2\frac{kt}{2}} \tag{2.43}$$

The $sin^2(kt/2)$ function at the denominator needs to be $m\pi$ (m = integer) in order to obtain the peak transmission or dip in the reflection graph. So

$$\frac{kt}{2} = \frac{\pi t}{\lambda} = m\pi \Rightarrow \nu_m = \frac{mc}{2nt\cos\theta_i}, \tag{2.44}$$

and finally, the free spectral range of the Fabry-Perot cavity can be obtained as follows:

$$\nu_{m+1} - \nu_m = \frac{c}{2nt\cos\theta_i} \tag{2.45}$$

In which, c is the speed of light, t is the spacer thickness, n is the refractive index of the spacer, and the θ_i is the incident angle. The Eq. 2.45, is very useful as it could be used to calculate the refractive index of a material.

CHAPTER 3

EXPERIMENTAL DETAILS

The first section of this chapter includes a detailed analysis of the sample's structures and designs. Thin film growth and the photolithography procedures are explained in the following sections.

3.1. Metamaterial Structure

In this thesis MMs are composed of two different unit cells with 180° phase differences. Figures 3.1 and 3.2 show a schematic image of unit cell structures. Unit cells with gold patch sizes of 90 µm and 60 µm (70 µm) are defined as 0-bit and 1-bit, respectively. The size of each MM super unit cell is 10×10, each composed of 8×8 unit cells. Two different patterns were created by these super unit cells including a checkerboard and a stripe pattern. The unit cell geometry was obtained using the commercial EM software CST.

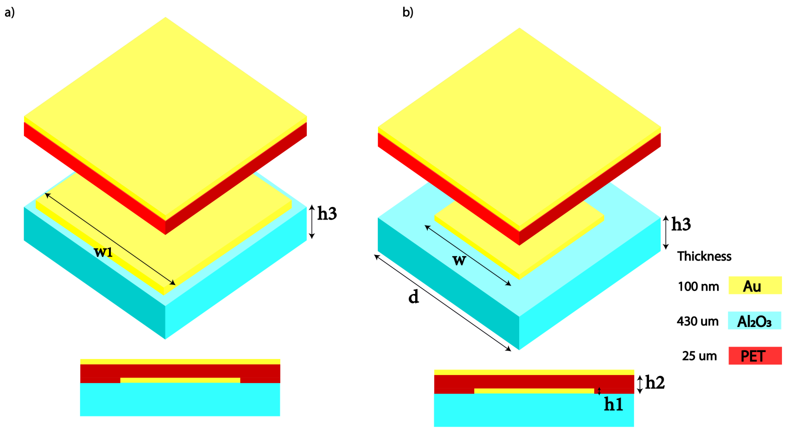

Figure 3.1. Schematic image of the hard-coded unit cells. a) 0-bit b) 1-bit.

A gold layer is deposited at the back-side of the structure in order to prevent the THz wave energy from passing through the structure and obtaining a full reflection. The VO_2 thin films were grown on the sapphire substrate with a thickness of approximately

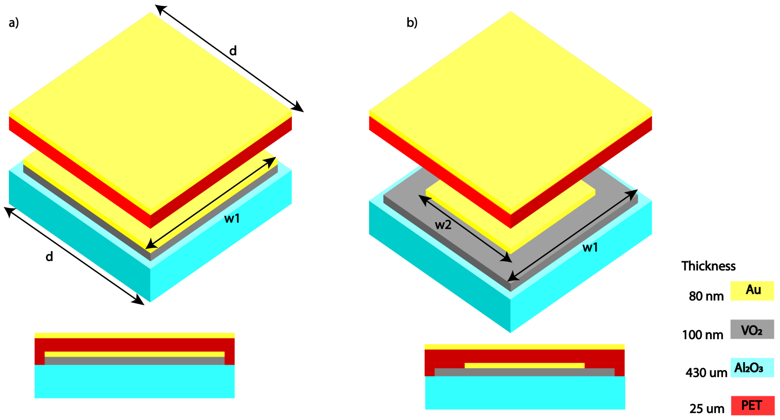

Figure 3.2. Schematic image of the VO_2 based unit cells. a) 0-bit b) 1-bit

430±10 µm. As the substrate was very thick, in order to avoid Fabry-Perot cavity resonance, the THz will be incident from the sapphire side.

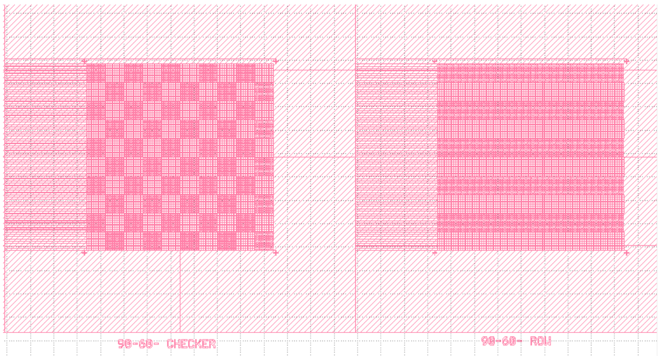

Figure 3.3. This image represents part of the UV lithography mask that was designed in Klayout.

A quartz mask was designed with different unit cell sizes for lithography (Figure 3.3). Figure 3.4 illustrates the optical microscopy image of the used photolithography mask. The mask was designed for both positive and negative photo-resist.

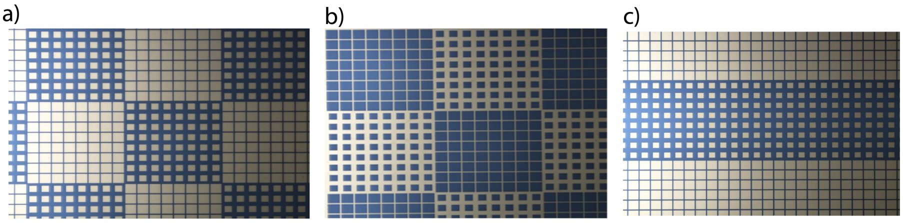

Figure 3.4. Optical images of UV lithography designed mask. a) Checkerboard pattern (70-90 µm) for positive photoresist. b) Checkerboard pattern (60-90 µm) for negative photoresist. c) Stripe pattern (60-90 µm) for positive photoresist.

3.2. Vanadium Dioxide Growth

Magnetron sputtering technique is a type of physical vapor deposition (PVD) that comes in two types, namely, RF and DC. DC magnetron sputtering is a sputtering technique with a conductor cathode (target) that is negative. Conductors or insulators can be used as targets in RF magnetron sputtering. In the process of magnetron sputtering, magnets are used to confine the secondary electrons emitted from the target, thereby improving excitation and ionization, and reducing contamination on the substrate. Figure 3.5(a) and Figure 3.5(b) illustrate the schematic diagram of the events that happen during the growth of VO_2 in the chamber. VO_2 was grown using our lab-made DC magnetron sputtering system (Figures 3.6 and 3.7). The complicated nature of the combination of vanadium and oxygen makes the VO_2 growth challenging. Sometimes different phases of the vanadium oxides can be found together in a sample. Then the growth procedure is crucial and must be conducted in the most efficient possible way. A lot of factors may affect the result of the thin film in order for growth to occur appropriately.

These factors include target-substrate distance, substrate temperature, deposition pressure, sample distance from the holder's center, etc. The above-mentioned parameters were optimized.

Before the growing steps, the substrates were cleaned using an ultrasonic vibration cleaner, successively in acetone, methanol, and propanol alcohol for 10 minutes for each step. Thereafter, it was placed on the sample holder in a specific optimized position. In this case, the position was optimized to be 13 mm from the center of the sample holder. A target of pure vanadium $\sim 99.99\%$ was placed 65 mm away from the sample holder. Sapphire ($c - Al_2O_3$ (0001)), with high thermal conductivity (27.21 $Wm^{-1}K^{-1}$ at 300 K) (Yüce, 2015) was used as a substrate. The advantage of using sapphire as the substrate is

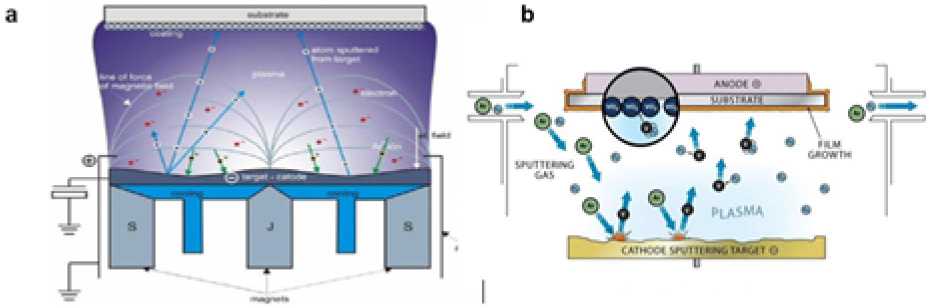

Figure 3.5. Schematic image of the a) magnetron sputtering b) VO_2 growth using DC magnetron sputtering. Source: sputtertargets.net (Yüce, 2015).

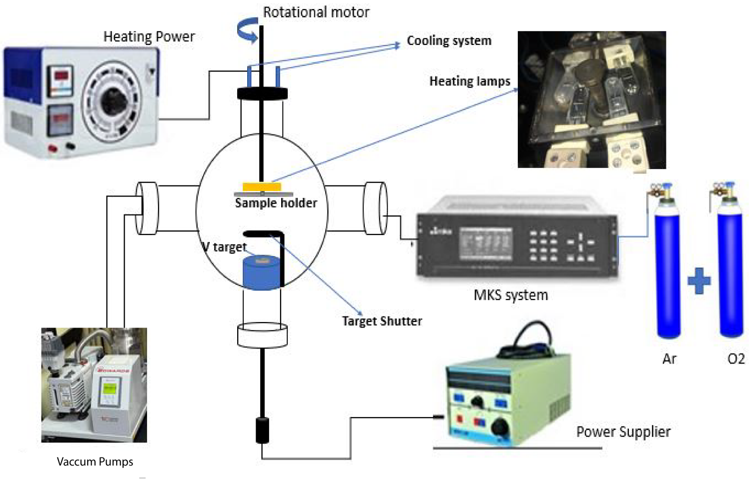

Figure 3.6. Schematic image of our lab's DC Magnetron sputtering system.

its wide availability and high transparency in the THz region (Zhu et al., 2012). The base pressure of the sputtering chamber was below 3.0×10^{-6} Torr, and during the deposition, the chamber pressure was 5.3×10^{-3} Torr. A 10-minute pre-sputtering was carried out to eliminate contamination from the surface of the vanadium target. The pre-sputtering was done by the power of 40 W, and 40 sccm Ar gas. During the deposition DC power of 70 W was directed to the V target. During the sputtering procedure and deposition, the substrate was rotating about 12 rpm to create a homogeneous film. In order to obtain VO_2 phase, 1.60% pure oxygen partial pressure (calculated using the equation 3.1) was sent into the argon medium inside the vacuum system during thin-film deposition by MKS gas controller (MKS Instruments Type 647C). A PID controller device connected to a J-type thermocouple was used to control the temperature and thus obtain the crystalline film. The

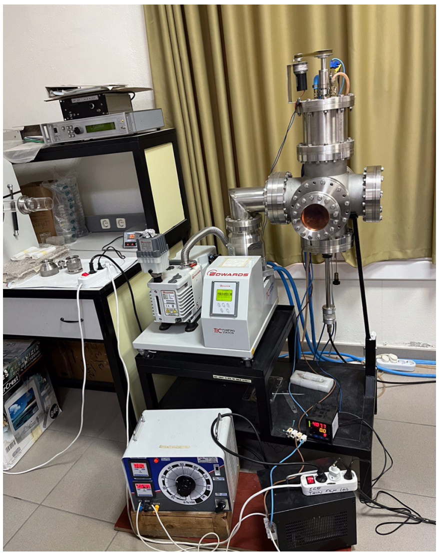

Figure 3.7. Actual image of our DC magnetron sputtering system.

substrate was slowly heated to 550°C prior to deposition and cooled slowly afterward. As part of this process, four lamps with a power of 24 V and 250 W were used for heating. The heating lamps were positioned 1 cm away from the top of the substrate holder as can be seen in Figure 3.6.

The partial oxygen pressure was calculated using the following formula (Alaboz, 2018):

$$\mathrm{p}_{\mathrm{oxygen}} = [\mathrm{Oxygen}(sccm)]/[\mathrm{Oxygen}(sccm) + \mathrm{Argon}(sccm)]. \tag{3.1}$$

3.2.1. The Electrical Characteristic of the Grown Film

The resistance of the produced VO_2 thin film by means of a probe station device (Janis Microprobe Station) was measured (Figure 3.8). As previously discussed in Chapter 2, VO_2 exhibits thermal hysteresis that includes both cooling and heating. A probe station (Figure 3.8) was used to measure the resistance change caused by temperature variations using a defined LabVIEW program and the Keithley 2100 digital multimeter instrument. The sample temperature was steadily elevated to 100°C under vacuum conditions until the metal-insulator transition of the film was observed, and this data was displayed as the heating graph. After turning off the heater, the cooling process began as the temperature progressively decreased to ensure that the transition was successful. If the resistivity of the film has changed by a factor of 10^4, the film VO_2 was successfully grown.

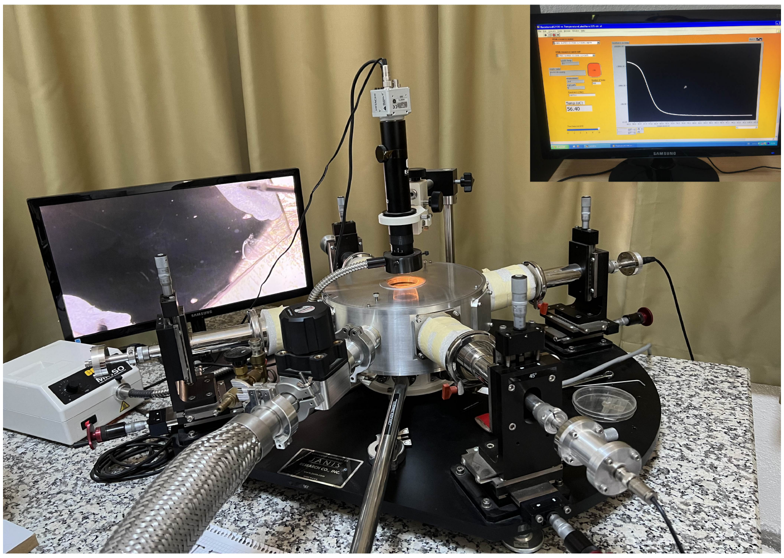

Figure 3.8. Four probe stations to measure temperature-dependent resistivity.

3.2.2. The Surface Characterization of the Grown Film

3.2.2.1. Scanning Electron Microscopy

Scanning electron microscopy (SEM) provides high-resolution images using electrons. The electron is generated by a source of tungsten or lanthanum hexaboride filament. This electron beam is focused on a small point after passing through a series of electromagnetic lenses. The e-beam is then guided to a region of interest and bombards the sample. Various electron fluxes are scattered after this bombardment, depending on the morphology of the sample. Images are obtained via secondary electron detection. Another electric potential is used to guide the electrons to the detector. Finally, a 3D image of the surface will be obtained.

As the VO_2 growth occurred at a relatively high temperature, conventional methods for determining sample thickness, such as photo-resist polymer, cannot be used. Since the polymer hardens throughout the growth process at high temperatures, it cannot be easily cleaned in order to assess the film thickness with profilometry equipment. Then, SEM cross-sections were used to measure the thickness of the VO_2 film and to analyze the sample's morphology.

3.2.2.2. X-Ray powder Diffraction

The technique of X-Ray powder Diffraction (XRD) is used to identify crystals since they have particular atom spacing. This method is based on Bragg's law, which states that the distance between atomic layers is proportional to the wavelength and angle of the incident beam (X-ray). As an X-ray's wavelength is comparable to the atomic spacing, this technique is used to assess material crystal orientation. XRD was carried out in the Bragg-Brentano focusing geometry on a Phillips X'Pert Pro X-Ray diffractometer, with Cu $k\alpha$ radiation (λ=1.5456 A°). The XRD patterns were collected from 2θ=10°-90° with a step size of 0.001° for all samples.

3.2.3. Surface Profilometer

After the films were patterned, the thickness of the patterned structure was measured using Veeco DEKTAK 150 profilometer after photolithography. In the profilometer, the thickness of a sample was obtained by measuring the vertical movements of the tip of the stylus on the surface and comparing them to the initial level of the stylus. Due to the possibility of the stylus scratching the samples, measurements were taken at the edges of the patterns, not at their center.

3.2.4. THz Transmission Characterization

The THz transmission spectra were obtained using the system, illustrated in Figure 3.10. In order to modulate the THz wave from the WR1.5 AMC (Amplified / Multiplier Chain), a function generator (Stanford Research Systems-DS335 Synthesized Function Generator) was first used with a frequency of 15 Hz and a peak-to-peak voltage of 4.0 V using the TTL modulation option of the WR1.5 AMC. A pair of 90° off-axis parabolic mirrors were then used to collimate this THz wave and focus the wave on the sample holder's origin. In order to focus a THz wave to the Golay Cell detector (Tydex GC-1P optoacoustic), the transmitted THz wave was collimated by a second pair of 90° off-axis parabolic mirrors. A lock-in amplifier (Stanford Research Systems 830 Lock-in Amplifier) was used to process the signals acquired by the Golay Cell. More information regarding the setup and each component of our Lab's THz transmission system may be found in the reference (Köseoğlu, 2020). CCMI module with a 45W 915 nm laser diode,

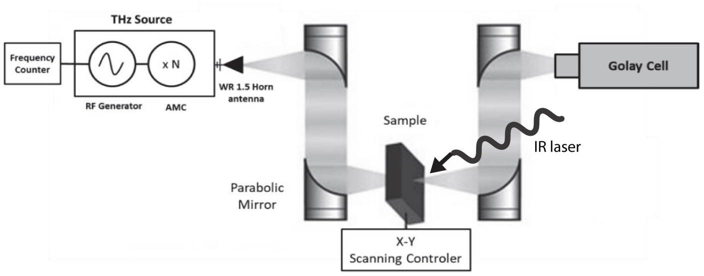

Figure 3.9. Schematic illustration of THz transmission system with an external laser.

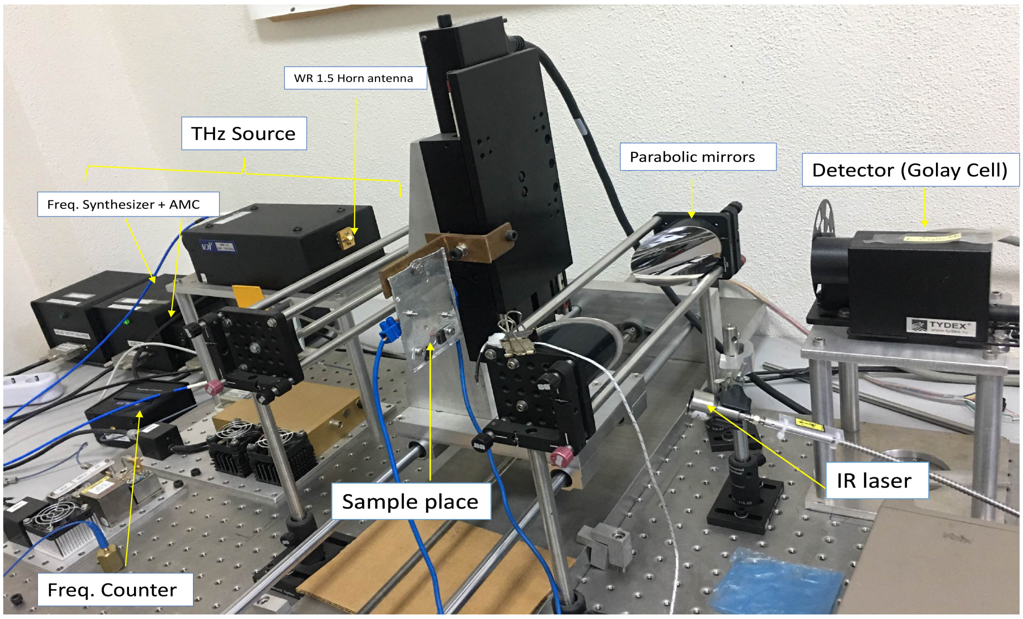

Figure 3.10. Illustration of THz transmission system with an external laser.

with 1.3 cm diameter output was used in order to optically modulate the VO_2 conductivity.

3.3. Gold Film Growth

As gold does not adhere properly when grown on top of dielectric material an adhesive layer is necessary. Metals, such as chromium or titanium, can be used as adhesion layers. In this part of the experiment, DC magnetron sputtering was used in order to grow the 100 nm gold layer on the top of the sapphire substrate (Figure 3.12). The chamber was evacuated to 5.0×10^{-2} Torr using a rough pump (RP), and then a turbo molecular pump (TMP) was used to achieve a 5.0×10^{-6} Torr vacuum. In order to clean the target and eliminate contamination, Ar gas was introduced into the chamber for a duration of 10 minutes and after that the base pressure of 5.0×10^{-6} Torr was achieved. MKS system was used to control the gas flow rate. To grow 15 nm of chromium, 40 sccm of Ar was initially introduced into the chamber. The work pressure was kept constant at 3.4×10^{-3} Torr, and the sample and target distance was around 7 cm. Approximately 50 W of DC voltage was applied. The 100 nm gold layer was sputtered onto the Cr layer with a DC power of 20 W (Advanced Energy, MDX 1K) and a steady Ar flow of 40 sccm. The time allotted for this deposition was 5 minutes. The Au and Cr deposition was done at ambient temperature with no heating within the chamber.

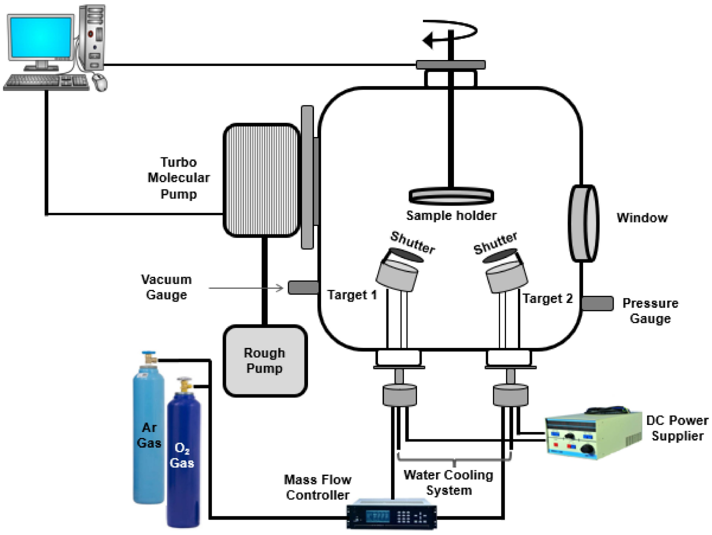

Figure 3.11. Schematically represented magnetron sputtering system used in this work for gold deposition (Yurttaş, 2021).

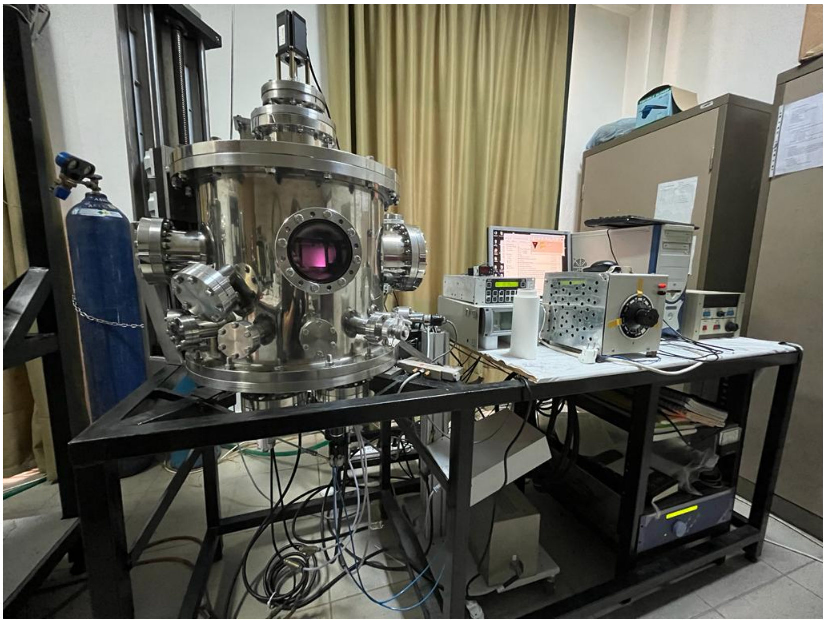

Figure 3.12. Lab-made magnetron sputtering system.

3.3.1. Optical Microscopy

The sample’s surface was analyzed using an optical microscope. Nikon ECLIPSE LV 150 optical microscope is located inside the clean room at Izmir Institute of Technology, physics department (Figure 3.13).

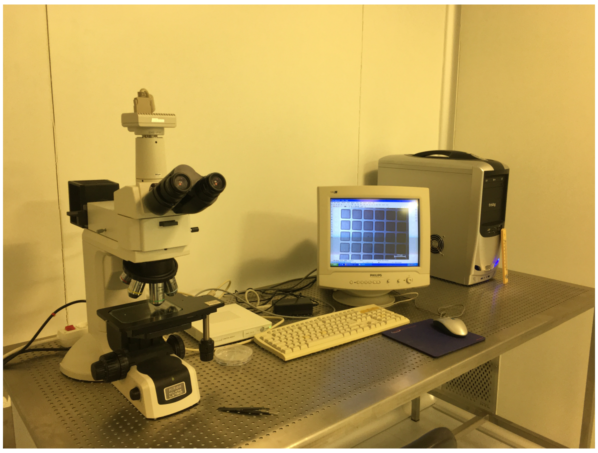

Figure 3.13. Nikon ECLIPSE LV 150 optical microscope.

3.4. Photolithography

In order to obtain the patterned structure for the MM (Figures 3.1 and 3.2), photolithography was done in the clean room of the 1000 class. In this part of the experiment, a spin coater was used to coat the AZ5214E photoresist at a speed of 3000 rpm. In this thesis, the photoresist was used as positive. Then samples were soft baked with a hot plate by 110°C for about 90 seconds. The purpose of this process is to evaporate the solvent, creating a solid AZ5214E photoresist. Then, the sample is exposed to UV light for a period of 20 seconds using the designed mask. Afterward, the samples are developed using NaOH solution 0.8 gram in 100 ml DI water, for about 20 seconds. The developer cannot dissolve the parts of the positive photoresist which have been exposed to UV light. However, the parts that have been exposed to UV can be easily removed by the developer. Immediately following the development process, the samples will be immersed in DI water and then dried using nitrogen gas. Etching VO_2 samples were challenging. Due to that hard baking process was immediately carried out following the photolithography. The samples were left in the oven for 30 minutes at 110 degrees Celsius.

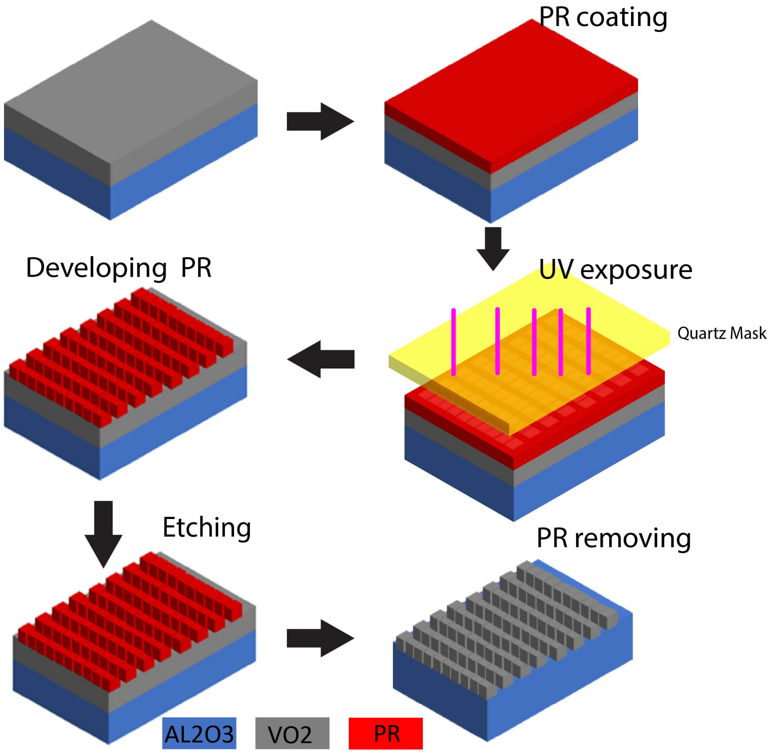

Figure 3.14. Schematic presentation of the photolithography process for the first step.

3.4.1. Dry Etching

The samples were etched by using a custom-built (in our laboratory) argon ion beam etching system, which included an etching chamber, a multi-gas controller (MKS Instruments Type 647C), a double-ending ion source (Advanced Energy MCIS-12), a DC power supply (Advanced Energy Pinnacle Plus), a thermocouple vacuum gauge, a cold cathode gauge, a turbomolecular pump (Agilent Varian Turbo-V 301), and a rough pump (Demirhan et al., 2017; Noori et al., 2021) (Figure 3.7). Both gold samples and VO_2 samples were etched after the lithography in order to achieve the desired square shape patches. Because high etching and heating rates of the beam can cause damage to the substrate surface if the beam is aimed perpendicularly at it during the etching process, the angle between the beam and the substrate surface was kept at 22.5° (Katzschner et al., 1984). The sample holder was cooled to prevent heating of the mask layer during the etching process. In order to obtain a smoother etched surface, the sample holder was rotated with the rotary feed-through. In order to accelerate the free ion beam, low-pressure values were required. Due to that before starting the etching process, the ion beam etching system was pumped up to a pressure of 3.0×10^{-6} Torr by an RP and a TMP. Whereas a maximum pressure of 3.0×10^{-3} Torr was maintained during the etching. During the plasma etching process, we used 30 sccm Ar, 70 mA beam current and 750 V beam voltage, and 49 W DC power. This ion beam etching is typically used on non-photoresist coated areas of the film, as it can only etch metals. Therefore, this technique was used to create the desired pattern on the film surface.

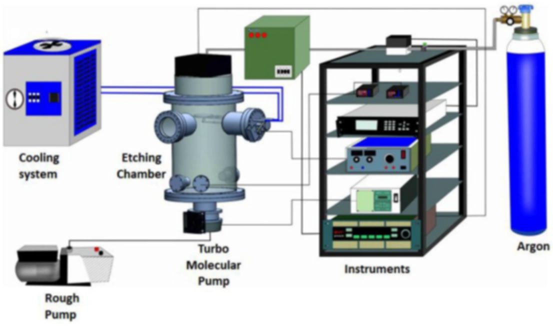

Figure 3.15. An illustration of the ion beam etching system in the schematic form (Sağlam, 2013).

3.5. Thermal Evaporation

Using a physical vapor deposition system (Leybold Univex 300) (Figure 3.16), approximately 80 nm thick was deposited on top of the patterned VO_2 samples and also as a ground layer for the gold and VO_2-based samples. In the first step, a metal mask one millimeter smaller than the sample size was created. These samples were mounted on a mask that covered the alignment lines from the photolithography in order to be used for second-layer fabrication. The chamber of the system was then evacuated to 10^{-6} Torr. The gold targets, which were portioned into little pieces inside the boat, were then evaporated at a rate of 0.7 A°/sec utilizing a current of roughly 126 A. Following this step, the samples were investigated using an optical microscope.

Figure 3.16. IZTECH physics department’s lab thermal evaporation system.

3.6. Spacer layer

As a dielectric spacer between the patch gold layer and the ground gold layer, PET was chosen. The modified Debye model was investigated in order to simulate the PET layer by CST. This model is applicable in the THz range (D'Aloia et al., 2020; Fedulova et al., 2012):

$$\varepsilon(\omega) = \varepsilon_\infty + \frac{\varepsilon_s - \varepsilon_\infty}{\left(1 + (j\omega\tau)^\beta\right)^\gamma} \tag{3.2}$$

Where, the γ= 2.9 and β=0.9 are fitting parameters, the relaxation time τ=0.05 ps ,and ε_s-ε_∞=0.46, ε_∞=2.54 (D'Aloia et al., 2020; Fedulova et al., 2012). Using isopropanol alcohol, the 25 µm PET layer was cleaned and placed on top of the patterned gold layer. The top and bottom of the samples were covered with Teflon pieces to maintain the straightness and firmness of the PET layer. Mechanical pressure was applied with two metal clips to compress the sample. In order to laminate the PET layer, the samples were placed inside a quartz tube inside the furnace (Figure 3.17). Next, the tube was vacuumed to 300 mTorr. The temperature increased by 17°C each minute until it reached 260°C. The samples were left to cool down for about 5 minutes.

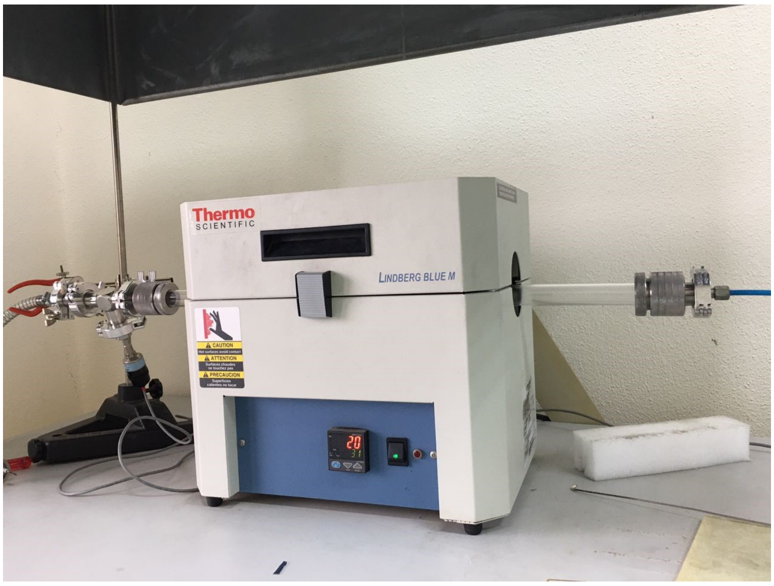

Figure 3.17. The annealing furnace.

CHAPTER 4

VO_2 FILM GROWTH AND CHARACTERIZATION

This chapter thoroughly describes the sample characterization results. Various samples were characterized and analyzed, and some of them were chosen for the final MM fabrication. In the thin film growth procedure, the chamber was inserted with a variable oxygen flow to get pure VO_2, and according to that, distinct VO_2 samples with different transition magnitudes could be obtained by adjusting just 0.01 sccm of oxygen. All other growth parameters were kept roughly constant, with the exception of the oxygen partial pressure, which varied slightly. Electrical, surface (SEM and XRD), optical, and THz transmission characterizations were performed on the produced films.

4.1. Samples Characterization

4.1.1. Electrical Characterization

Electrical characteristics of VO_2 thin films were investigated to analyze the MIT properties and determine temperature-dependent resistance of the films by probe station device (Figure 3.8). All the grown samples were investigated using the probe station device, and the samples showing a transition magnitude of more than $10^{2.5}$ were selected for further studies. Because this amount of change in the conductivity is sufficient to use the samples. S1 and S2 are two of the best samples that had excellent changes in resistance magnitude and sharp transitions. The partial oxygen pressure of this sample was 1.59% and the transition magnitude is the order of $10^{3.77}$ and $10^{4.36}$, respectively (Figure 4.1). These samples were chosen for the XRD characterization. Two other samples are named S3 and S4 (Figure 4.2), these films are then used to fabricate the VO_2-based MM, checkerboard, and strip pattern, respectively. On the hysteresis graph, usually, the cooling state appears to be more stable than the heating state.

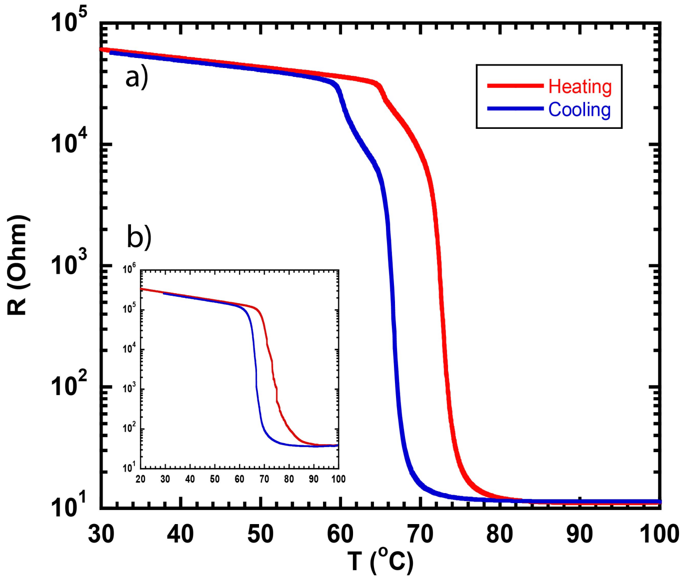

Figure 4.1. Temperature dependent resistance graph a) Sample S1 with a change of the resistance of $10^{3.77}$ and b) S2 with the change of the $10^{4.36}$.

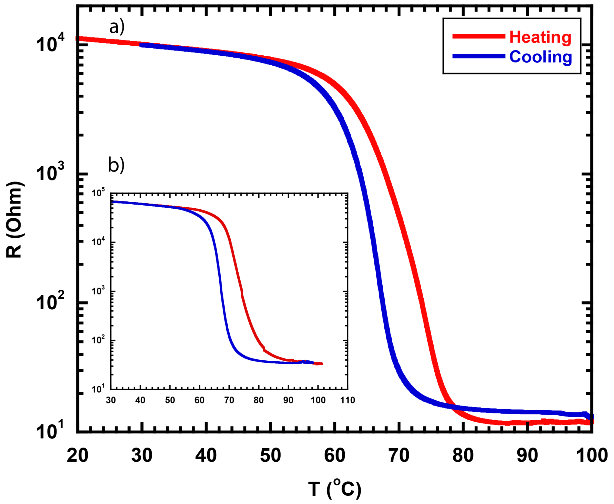

Figure 4.2. Temperature dependent resistance graph a) Sample S3 with a change of the resistance of $10^{2.98}$ and b) Sample S4 with a change of the resistance of $10^{3.25}$.

The characterized samples in this section were grown with a partial oxygen pressure of 1.59%. As can be observed in Figure 4.1(a) there is a step at the hysteresis graph in both cooling and heating cycles. In this case, we have two steps in both cycles that may be related to the existing different VO_2 phases at the same time in the film. This could also be caused by the maximums of the grain size distributions (Klimov et al., 2002). In some studies, the asymmetric dis-shape in hysteresis, such as in the cooling cycle or in the heating cycle, could be explained by the physical structure of the film (Currie et al., 2019).

4.1.2. Surface Characterization

4.1.2.1. Scanning Electron Microscopy

The morphology and the cross-section of the as-grown selected VO_2 sample is illustrated in Figure 4.3. As it can be seen, in Figure 4.3(a), the agglomerates of the VO_2 and the grains are illustrated. In Figure 4.3(b), the SEM cross-section of the S1 sample is shown which indicates the average thickness is about 283 nm. As it was mentioned earlier, since the growth temperature was very high (550°C), the thickness measurement was not possible using the photo-resist technique.

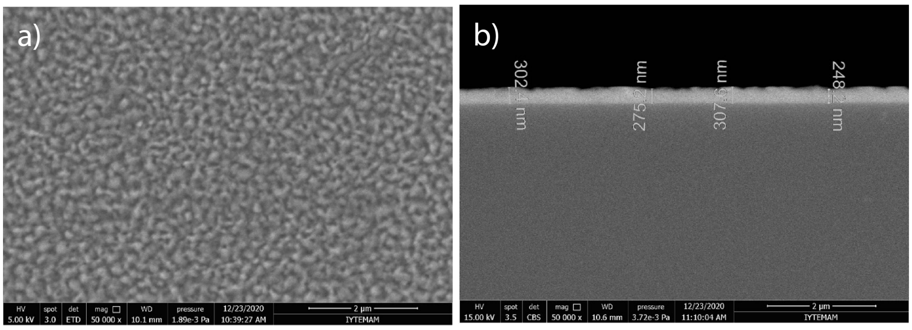

Figure 4.3. Vanadium dioxide grown on the sapphire substrate surface grains and cross-section a) and b) as grown VO_2 (S1) thin film.

4.1.2.2. X-Ray powder Diffraction

Figure 4.4 The primary peaks of the VO_2 sample's XRD pattern are located at 38.12, 64.45, and 44.31, respectively, and these may be associated with the monoclinic vanadium dioxide phase and plans (200) (Zhao et al., 2012), the quadrangular crystalline feature of vanadium dioxide (013) (Santulli et al., 2009), and (210) (Kim et al., 2014), respectively (Figure 4.4). In the sample presented in Figure 4.5, major peaks are found at 38.09, 39.84, 44, 28, and 85.99 and can be correlated with the plane orientation of (200) (Zhao et al., 2012), (020) or (002) (Yang et al., 2010). (210) (Kim et al., 2014) and second-order reflection of the monoclinic phase of vanadium dioxide from the plane (020) or (002), respectively (Yang et al., 2010). The peaks of 41.6 are related to the c-cut sapphire substrate (Zhao et al., 2012).

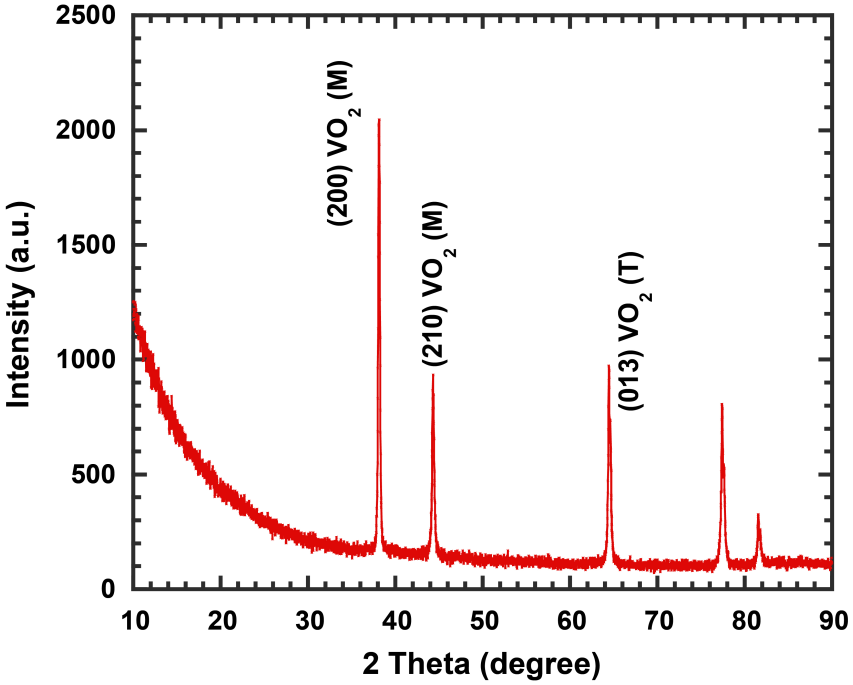

Figure 4.4. XRD patterns of the S1 as grown VO_2 thin film.

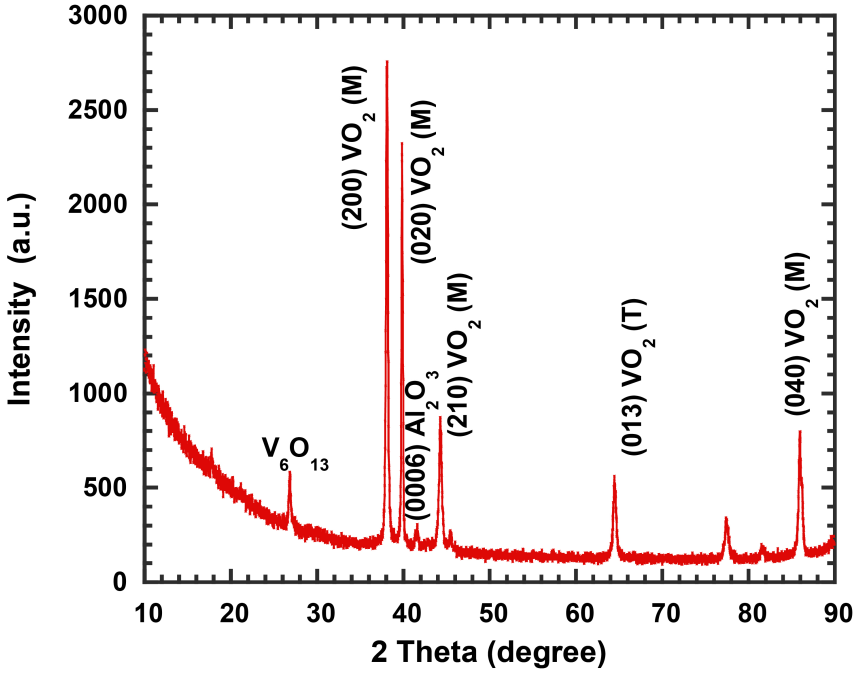

Figure 4.5. XRD patterns of the S2 as grown VO_2 thin film.

4.1.3. THz Transmission by Applying Laser on the Samples

In the 2nd chapter, it is noted that the VO_2 particles are in a monoclinic structure at room temperature without an external laser, and they act as an insulator. With low laser power, only a limited portion of the VO_2 particles transform into the rutile metallic phase, forming discrete metallic domains and then, VO_2 nanostructures are gradually filled with discrete metallic domains as the laser power increases (Zhao et al., 2018). VO_2 grown films were analyzed by measuring their THz transmission and comparing them to their substrate. The THz transmission measurement was performed using the system explained in Chapter 3 (Figure 3.10). The wavy pattern (oscillation) of the normalized data graphs is caused by the Fabry-Parot effect means multiple reflections inside the thick substrate. Figure 4.6 shows the raw and normalized data for bare sapphire substrate at different laser power. Each sample was illuminated for 6 minutes, then the transmission spectrum was measured. The graphs show that temperature has no significant effect on the sapphire properties in the THz region. The raw data for the air, sapphire substrate, and the grown film on top of the sapphire were measured using various laser powers in the figures below (Figure 4.6(a), 4.7(a), 4.8(a), 4.9(a) and 4.10(a)). Figure 4.6(b), shows the bare sapphire normalized THz transmission at various laser intensities and shows that temperature has no impact on this transmission. The sharp peak at 0.56 THz, is caused by water absorption of the THz wave.

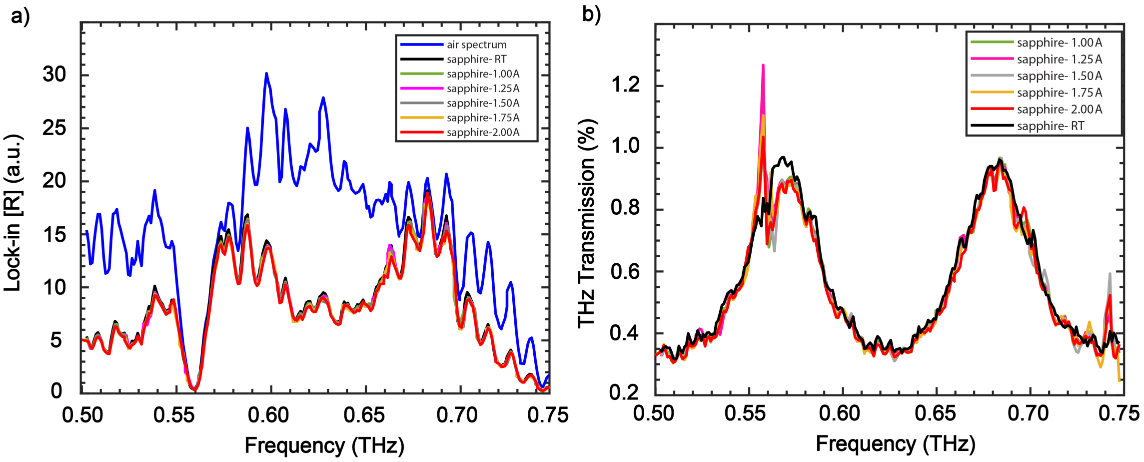

Figure 4.6. THz transmittance spectrum of sapphire substrate with different CW laser power. a) Raw data. b) Normalized to the air data (bare sapphire).

Figure 4.7(b) presents the S3 sample's (bare VO_2) normalized intensity (the effect of the air and sapphire are extracted) at various laser powers. The outcome shows that a 1.25 A laser is sufficient to modulate the VO_2 film. Figures 4.8(a and b), show the raw and normalized data of the S3 (bare patterned VO_2) after it is patterned by photolithography as square patches with a side size of 90 µm. Comparing Figures 4.7(b) and 4.8(b) (as grown and patterned film), there is still a transmission in the patterned structure while VO_2 is operating in its conductive state and as a result of entering a conductive medium, the resonance frequency has now undergone a π shift. The same situation exists for the sample Figure 4.9(b) (thin film) and 4.10(b) (patterned film).

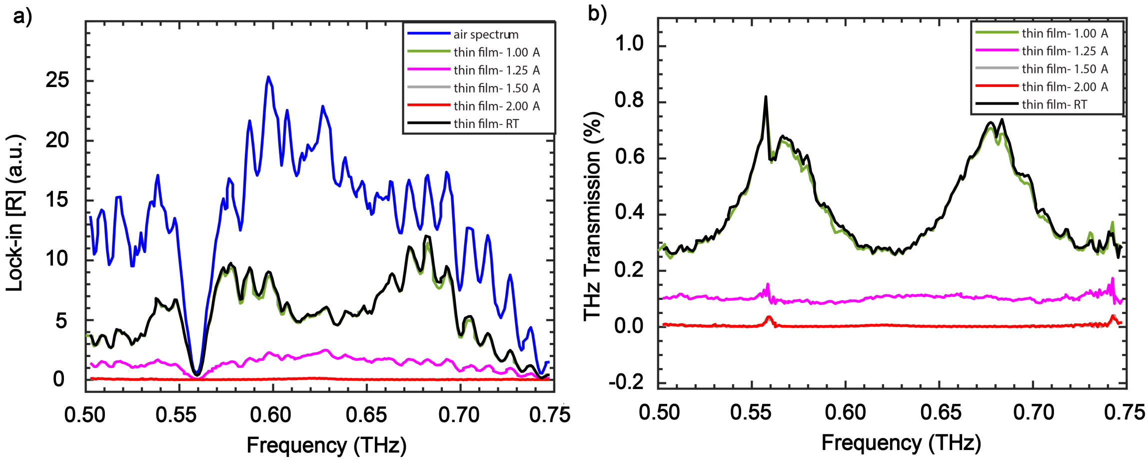

Figure 4.7. THz transmittance spectrum of VO_2 thin films (S3) coated on the sapphire substrate at different laser exposure power. a) Raw data, b) Normalized data graphs (bare thin film).

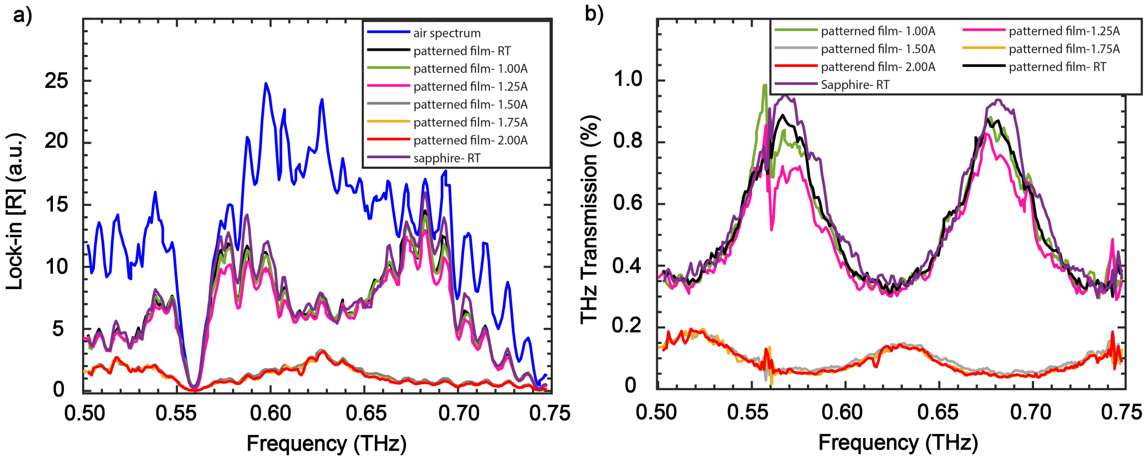

Figure 4.8. THz transmittance spectrum of VO_2 patterned thin films (S3) coated on the sapphire substrate at different laser exposure power. a) Raw data, b) Normalized data graphs (bare patterned thin film).

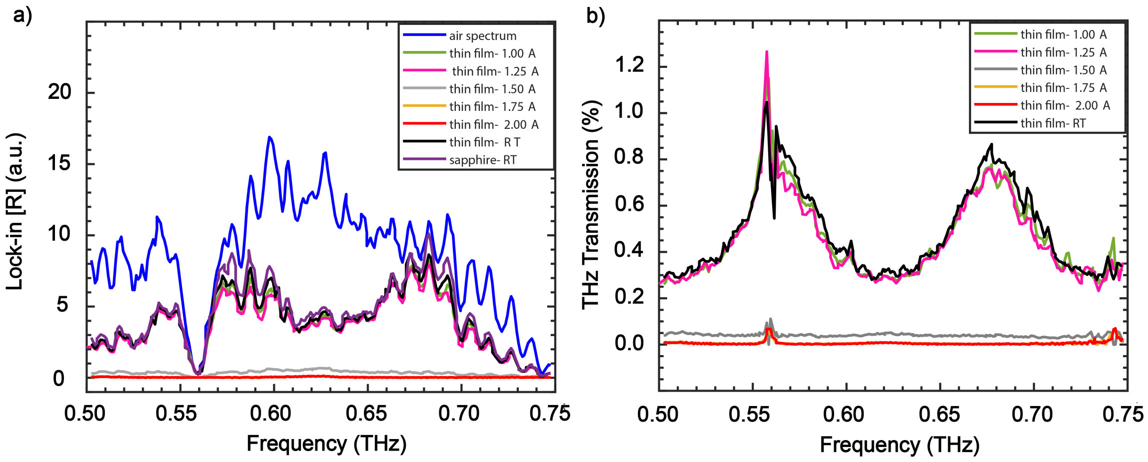

Figure 4.9. THz transmittance spectrum of VO_2 thin films (S4) coated on the sapphire substrate at different laser exposure power. a) Raw data, b) Normalized data graphs (bare thin film).

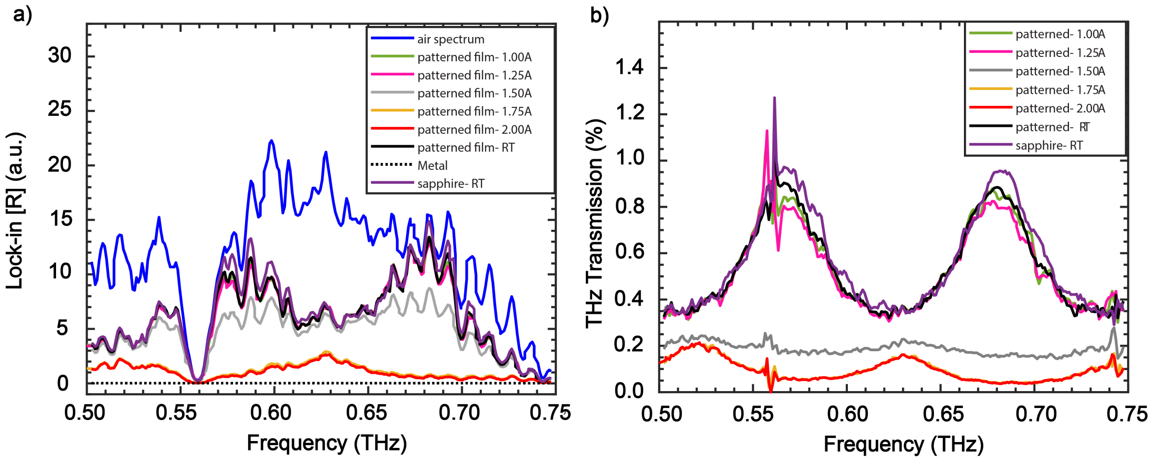

Figure 4.10. THz transmittance spectrum of VO_2 patterned thin films (S4) coated on the sapphire substrate at different laser exposure power. a) Raw data, b) Normalized data graphs (bare patterned thin film).

4.2. Conclusion

In this chapter THz spectrum transmission was measured through the VO_2 layer (Figures 4.7 and 4.9). The results reveal that when VO_2 is in the insulating phase, it is quite transparent to THz waves and has the same transparency as a sapphire substrate. When a laser is incident onto the structure, the VO_2 layer becomes metallic and will reflect and absorb the incident waves, resulting in a decrease in THz transmission. As the laser power increases the THz transmission (%) will decrease. This result indicates in the case of THz waves, VO_2 films exhibit excellent photo-induced switching properties (Zhao et al., 2018).

THz transmission characterization was obtained for each sample after and before the VO_2 layer photolithography. The results implies that the patterned film shows a greater transmission which is expected as some of the film is removed and the sapphire is also transparent for the THz wave. It also could be due to the decreasing film thickness after a 3 hours etching process. In the region of 0.557 THz and 0.562 THz, there is a THz water absorption frequency that can not be kept constant in our laboratory. Due to unstable humidity conditions, in this region, there are some peaks and sometimes it exceeds 1. Also, it has been observed that, in higher temperatures, when the vanadium dioxides turn to be fully metallic, the spectrum will show a π phase shift which is expected as the VO_2 refractive index increases. From the normalized figures, the sapphire refractive index could be obtained using the Fabry-Parot cavity feature, which is explained in Chapter 2 in detail.

$$\triangle\,\nu = \frac{c}{2nd\cos\theta} \tag{4.1}$$

Where $\triangle\nu$ is the distance between two peaks, which is 115 GHz (Figure 4.6(b)), d is the thickness of the sapphire, which was approximately measured between 430±10 µm, θ is the incident angle which 0 here, and c speed of light. The result shows that the refractive index of the sapphire is about 3.04, which is consistent with literature (Lee, 2009).

CHAPTER 5

HARD-CODED AND VO$_2$-BASED CODED METAMATERIALS FOR TERAHERTZ WAVEFRONT ENGINEERING

The concept of coding MM, which was developed in 2014 (Cui et al., 2014; Della Giovampaola and Engheta, 2014) and opens up a new universe of possibilities for the development and production of flexible MMs, was highlighted in Chapter 2. The development of coding MM could also expand the applications of earlier versions of MM.

A coding MM comprises unit cells that can be encoded using binary digits (0 and 1), in which, by creating the coding sequences of digital unit cells EM scattering and radiation patterns may be regulated. Coding unit cells can easily be identified by their opposite reflection phases, which correspond to coding unit cells ”0” and ”1”. The use of coding MMs was widespread within the THz range for controlling EM scattering pattern (Chen et al., 2018; Gao et al., 2015; Liu et al., 2016; Noori et al., 2023; Shabanpour et al., 2020; Shao et al., 2019; Zhang et al., 2017).

Once an MM has been designed and fabricated, its uses are constrained. Therefore, a new MM needs to be created for each unique function. Recently, researchers have shown curiosity in using tunable materials to create their MM. This enables them to fabricate more flexible apparatuses while also expanding the applications of their devices. Therefore, it is necessary to create a multifunctional MM that can be altered by the use of tunable materials. In this chapter, a unique MM structure that regulates THz reflected waves and functions as a beam splitter is designed, fabricated, and characterized. The fabricated beam splitter MMs allow EM waves to propagate in a specific direction. As a result, they have the potential to play an important role as functional devices in visible light, microwave, and THz systems (Yin et al., 2022).

Here, the 0-bit super unit cell contains 8× 8 unit cells of ”0” (90 µm), and the 1-bit super unit cell, contains 8× 8 unit cells of ”1” (60 µm and 70 µm). The MMs are created by arranging the super unit cells in striped and checkerboard patterns. The striped pattern MM can transform the normal incident wave into two oblique orientations with similar angles to the z-axis when the super unit cells are built in a coding pattern like ”0101.../0101...”. The ”0101... /1010...” coding scheme, which separates the normal incident into four beams that are each at an equal angle with respect to the z-axis, is used to depict the checkerboard distribution (Figure 5.1).

This chapter is divided into two major sections: the first deals with the hard-coded MM, and the second deals with the VO_2-based MM. Design, simulation, fabrication, and experimental findings are included in both sections.

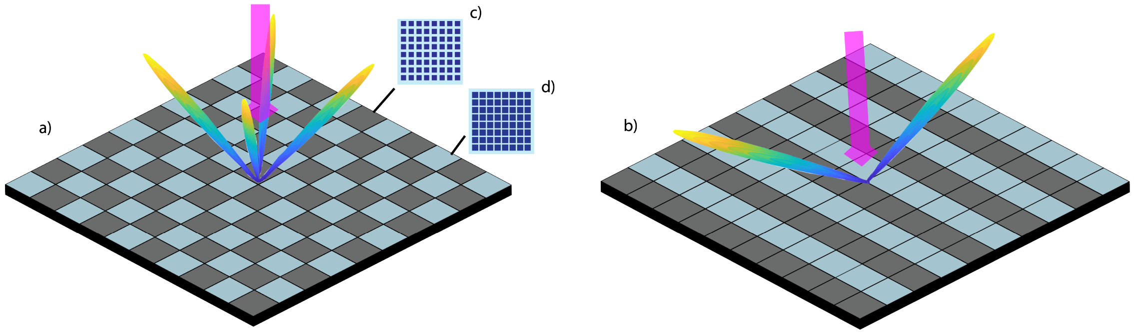

Figure 5.1. The conceptual presentation of the fabricated MM under a normal incident beam. a) the checkerboarded design and four scattered oblique beams. b) The stripe design and two scattered oblique beams. c) 1-bit supercell, contains 8×8 unit cells of ”1” (60 µm). d) 0-bit supercell, contains 8×8 unit cells of ”0” (90 µm). (Noori et al., 2023).

5.1. Hard-Coded MM for THz Wavefront Engineering

The findings from this section are presented in a publication (Noori et al., 2023).

5.1.1. Unit Cell Design

Figure 5.2 shows a schematic view of the fabricated MM studied in this section. CST software was used to determine the geometric dimensions, amplitudes, and phases of the unit cells. The proposed MM consists of four layers; the sapphire layer, the square gold patch layer, the dielectric spacer, and the ground gold layer responsible for achieving reflection.

Polyethylene terephthalate (PET) was utilized as a spacer layer because it has a very low weight, good THz transparency, is cost-effective, and is simple to laminate and

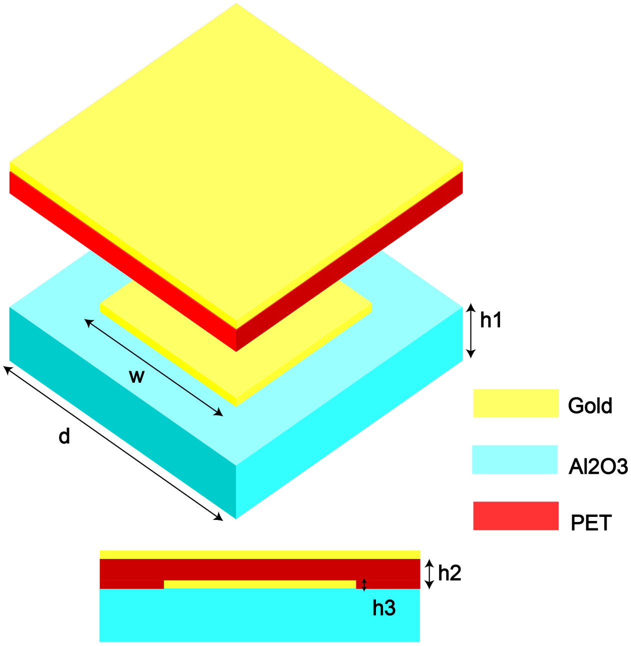

Figure 5.2. The hard-coded unit cell is depicted schematically (Noori et al., 2023).

simulated with the (ε= 2.54, μ= 1) (D'Aloia et al., 2020; Fedulova et al., 2012). A patterned square patch made gold layer was deposited to sapphire (ε= 9.61, μ= 1). The gold layer properties were taken from the CST material library. The periodicity of our coding unit cell is d = 100 μm. The side length of the gold square patch determines the type of the unit cell means ”0” or ”1”. This unit cell represents our 1-bit unit cell if the gold square patch's side is 60 μm or 70 μm, and the 0-bit coding unit cell if the gold square patch's side is 90 μm. The thickness of the sapphire substrate, square gold patch, spacer layer, and ground layer are 428 μm, 100 nm, 25 μm, and 80 nm, respectively. The following boundary conditions were used in CST (version 2021) in order to determine the reflection properties of unit cells (0-bit and 1-bit): an open (add space) boundary condition along the z-axis, and unit cell boundary conditions along the x and y-axes. The linearly polarized plane wave was used as the source with default tetrahedral meshing.

5.1.2. Device Fabrication and Measurement System

A brief explanation of the MM fabrication process is provided in this part; Chapter 3 discussed the more thorough steps. (c-Al_2O_3 (0001)) with a surface area of almost 1 cm^2 was employed as a substrate. A DC magnetron sputtering device was used to grow gold

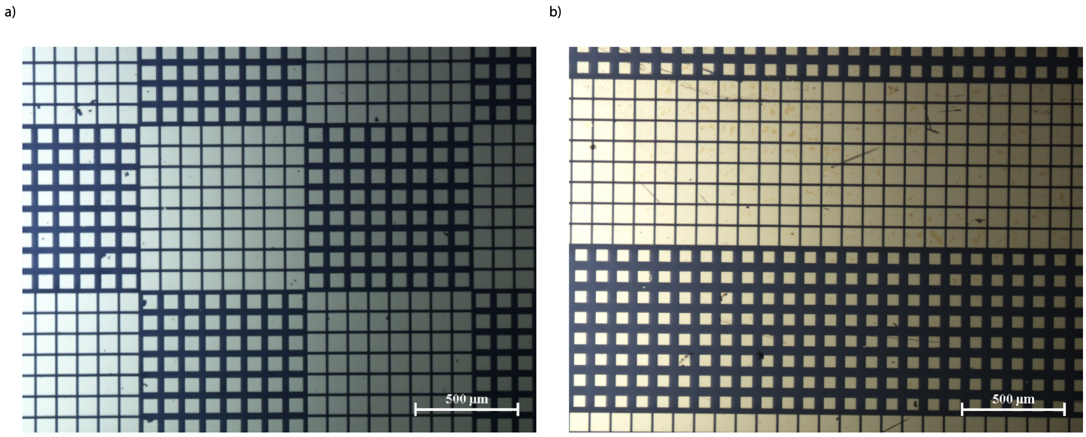

Figure 5.3. Optical images of two samples are illustrated after photolithography and dry etching. a) Checkerboarded design. b) Striped design (Noori et al., 2023).

with chromium assistance. The chromium layer was 15 nm thick, and the gold layer was 100 nm thick. Then, using conventional photolithography, the gold layer was patterned into 0-bit and 1-bit unit cells. After that, samples were etched using argon ion beam etching equipment. In order to create a dielectric layer to separate the gold patches from the ground gold layer, a 25 μm polyethylene terephthalate (PET) layer, was laminated onto the samples using thermal annealing. A gold ground layer of 80 nm was then deposited at a rate of 0.7 A°/sec using a thermal evaporation system. Figure 5.3 illustrates the optical microscope images of the fabricated stripe and checkerboard patterns (just two samples out of four are presented). Figure 5.3(a) illustrate checkerboard design, the 1-bit supercell is up of 8× 8 unit cells that are 70 μm in size. Figure 5.3(b) shows the striped design and the 1-bit supercell is up of 8× 8 unit cells that are 60 μm in size.

Figure 5.4, shows the schematic of a custom-built experimental setup for measuring the fabricated MM. The THz source used in the custom-built experiment setup (Noori et al., 2023) consists of an RF generator, a frequency counter, and a VDI WR1.5 AMC. The frequency range of this THz source is 0.50- 0.75 THz. A homemade linear motorized stage with a step motor (x-axis) is controlled by Lab-view with a lead-Shine step driver and MC USB201 controller, while the y-axis is controlled by Lab-view using Newport ESP 301 controller), and it is used as a sample stage. The Tydex GC-1P optoacoustic Golay Cell detector modulates a signal from an LED onto a photodetector by expanding a small volume of gas to bend a flexible mirror. A detector with a conic aperture which may have a sort of frequency selectivity, for the same power input, responds better at lower frequencies than at higher frequencies. The THz waves, emitted from WR1.5 AMC, were

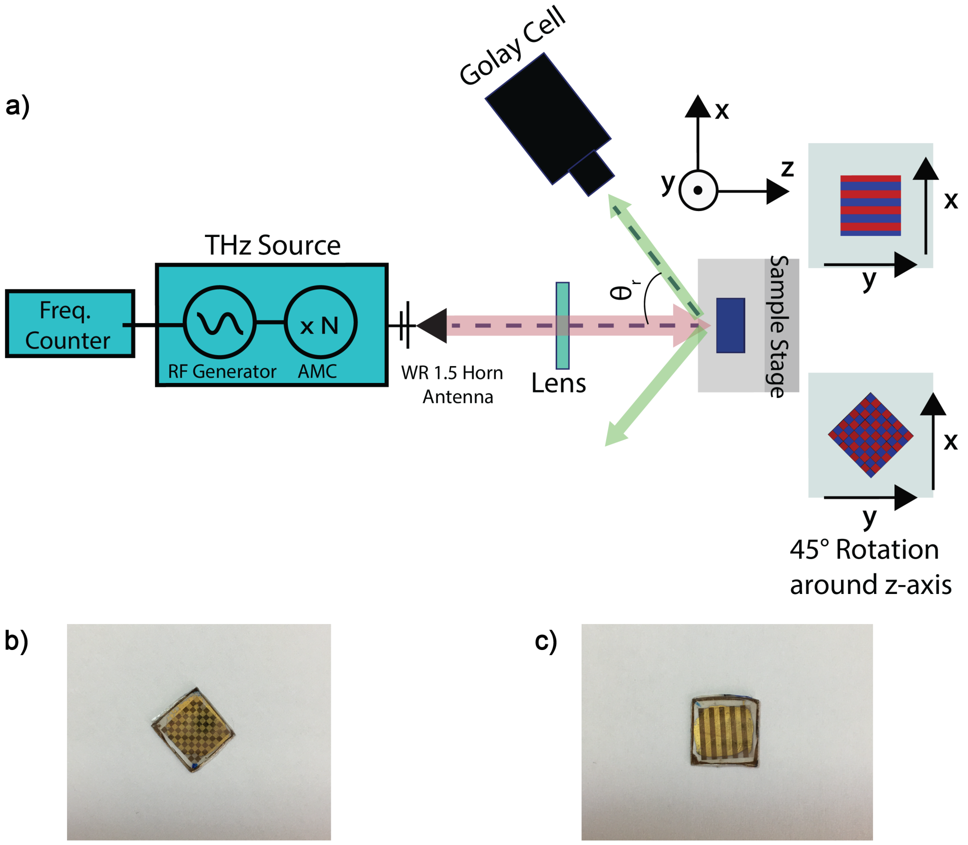

Figure 5.4. a) The experimental setup diagram. b) An illustration of the checkerboard pattern sample. c) An illustration of the stripe pattern sample (Noori et al., 2023).

first modulated by a function generator (Stanford Research Systems-DS335 Synthesized Function Generator) with 15 Hz frequency and 4 V peak-to-peak voltage using the TTL modulation option of the WR1.5 AMC. Teflon Lens with a focal length of 10 cm and 5 cm diameter was used to collimate the sub-millimeter waves emitted from VDI WR1.5 AMC. The WR1.5 AMC is equipped with a diagonal horn antenna to minimize the extra power. The sample is put on an x-y stage to ensure that the incident light is focused into the MM with a normal angle of incidence. To obtain the desired reflection beam, the stripe pattern sample is positioned according to Figure 5.4(c), and the checkerboard pattern is rotated 45 degrees (Figure 5.4(d)) so that the reflected beam can be measured in different angles without changing the detector height. Finally, the Golay Cell signals were examined using a lock-in amplifier (Stanford Research Systems 830 Lock-in Amplifier). A beam diameter of approximately 5 mm was obtained for this configuration (Noori et al., 2023). Due to the beam size, the MM physical structure inside the MATLAB code was considered as 6×6 super unit cells, which are made of 8×8 unit cells.

5.1.3. Result and Discussion

5.1.3.1. Simulation Results

Figure 5.2 illustrates a squared coding unit cell at THz frequency that confirms the beam splitting principle. Figures 5.5(a, b, c, and d) represent the simulated reflection amplitude and phase difference between the 1-bit (60 µm and 70 µm) and 0-bit unit cell (90 µm) from 0.50 to 0.75 THz. By adjusting the size of the metallic gold patch, the suggested unit cell has a relative reflection phase difference of 180°. The operation frequency depends on the patch sizes of 1-bit unit cells.

The phase difference of 180° between 1-bit (60 µm) and 0-bit (90 µm) unit cells has been successfully achieved at 0.526, 0.570, 0.634, and 0.665 THz (Figure 5.5(a and b)) by the suggested unit cells. At these frequencies, the reflection amplitudes of two coding unit cells are approximately equal to 1, resulting in the encoded MM's high reflection efficiency. For the 1-bit (70 µm) and 0-bit unit cell (90 µm) (Figure 5.5(c and d)), 180° phase difference was achieved at 0.528 and 0.550 THz, and also a phase difference of 165° (near 180°) at 0.640 THz. Additionally, at these frequencies, the reflection amplitudes between two unit cells are almost equal to one. The reflection amplitude graph has two dips due to the Fabry-Perot cavity effect caused by the thick sapphire substrate. The expected resonances occur near frequencies 0.53 THz, 0.57 THz, 0.63 THz, and 0.66 THz for 60-90 µm case. For the 70-90 µm case the expected resonances occur at 0.53 THz, 0.55 THz, and 0.64 THz (Noori et al., 2023).

5.1.3.2. Analytically Calculations

This section presents the normalized intensity versus different reflection angles for each frequency. The amplitudes and frequencies obtained from Figure 5.5 were used as input. To obtain the normalized intensity the far-field scattering pattern, Eq. 2.12, was solved in MATLAB. The outcome of the MATLAB is shown in Figures 5.6(a, b, c, and d) and results are approximately compatible with the equations 2.16 and 2.17 for each

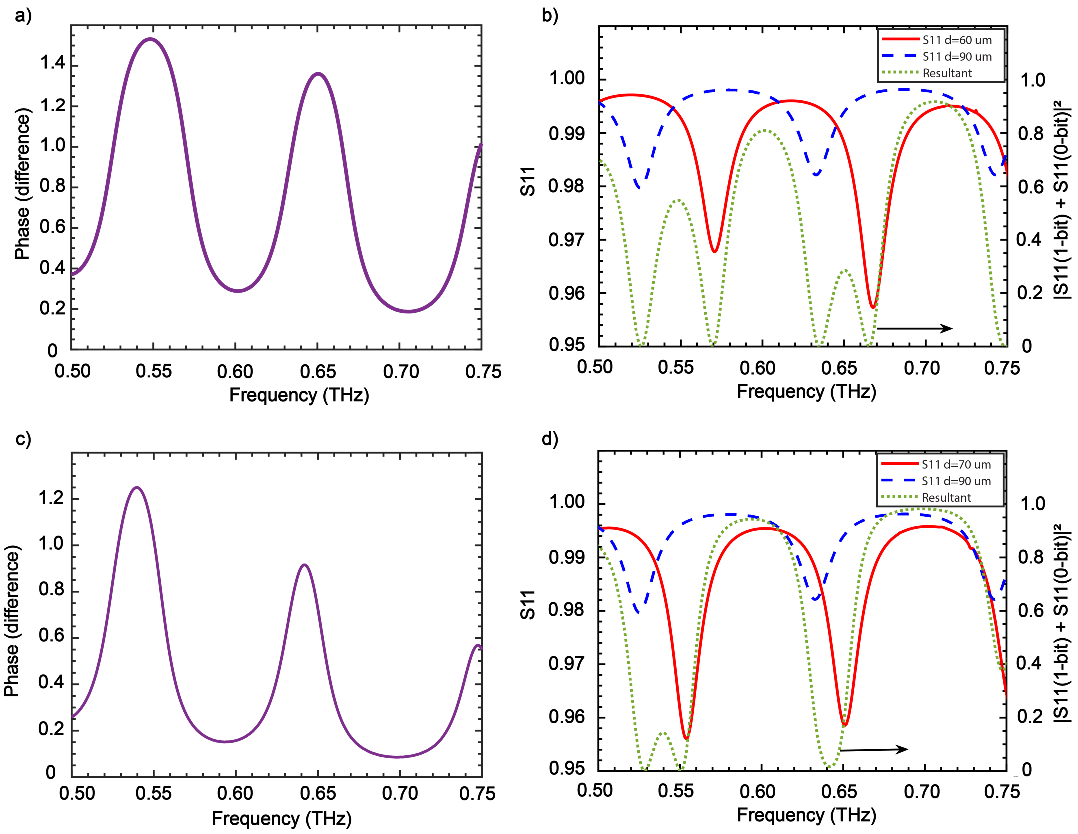

Figure 5.5. Outcome of the CST simulation. a) Reflection phase difference of 1-bit (60 µm) and 0-bit (90 µm) unit cells. b) Respective reflection amplitude of the unit cells of sizes 60-90 µm (left axis) and their combined reflected intensity (right axis). c) Reflection phase difference of 1-bit (70 µm) and 0-bit (90 µm) unit cells. d) Respective reflection amplitude of the unit cells of sizes 70-90 µm (left axis) and their combined reflected intensity (right axis) (Noori et al., 2023).

structure. The outcome demonstrates that the reflection angle decreases as the frequency increases, which is consistent with the theoretical prediction. The maximum reflection angles obtained from the normalized intensities in Figures 5.6 are slightly less than the angles obtained from the equations 2.16 and 2.17.

5.1.3.3. Measurement Result and Discussion

A variety of angles were measured using the setup mentioned above (Figure 5.4). Due to the Golay Cell blockage, there is a measurement limitation angle for the system. The available measurement angles with this configuration are between 23° and 60° with

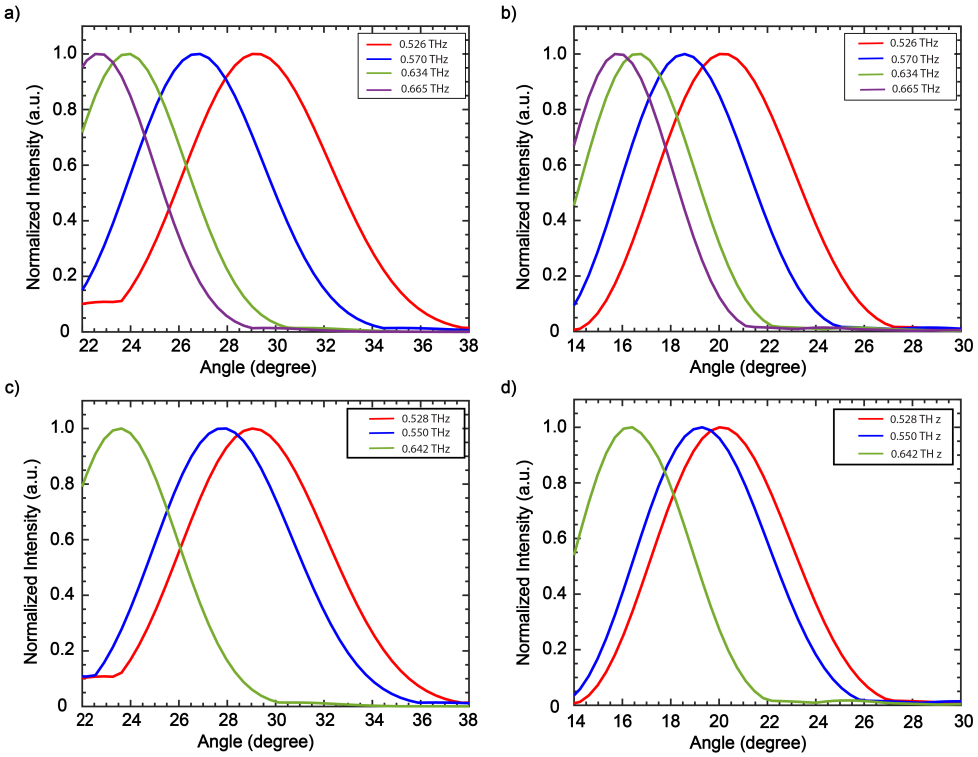

Figure 5.6. For the unit cell sizes of 60-90 μm and 70-90 μm, normalized data of a certain frequency behavior at different angles were determined using MATLAB analytical computations (Noori et al., 2023). a) The checkerboard pattern (60-90 μm). b) The stripe pattern (60-90 μm). c) The checkerboard pattern (70-90 μm). d) The stripe pattern (70-90 μm).

the step of 1°. The results can be applied to both sides of the z-axis based on the measurement on one side. Figures 5.7 display the whole spectrum intensity (Lock-in values) measured at various detector angles. The measured data for various angles are normalized to their highest values for each frequency (Figure 5.8). The outcome is shown in Figure 5.8. This graph's behavior can be compared to Figure 5.6.

Figure 5.7 shows that the intensity is almost zero at 0.560 THz, which is the water absorption frequency. As a result, the intensity value around 0.560 is measured low. At frequencies over 0.650 THz, the source's intensity starts to wane, therefore, we may not be able to observe significant peaks in that range. So, to overcome this issue, the data have been normalized to their maximum values in Figures 5.8. Three measurements were made for each angle, and the average result with a negligible error bar is shown in Figures 5.8. As illustrated in Figure 5.8(a) for the checkerboard pattern with 60-90 μm unit cells, the reflection angle for 0.526, 0.570, 0.634, and 0.665 THz, is calculated using the eq. 2.17 as 30°, 28°, 25°, and 24°, respectively, but it is measured as 30° and 31° for 0.526

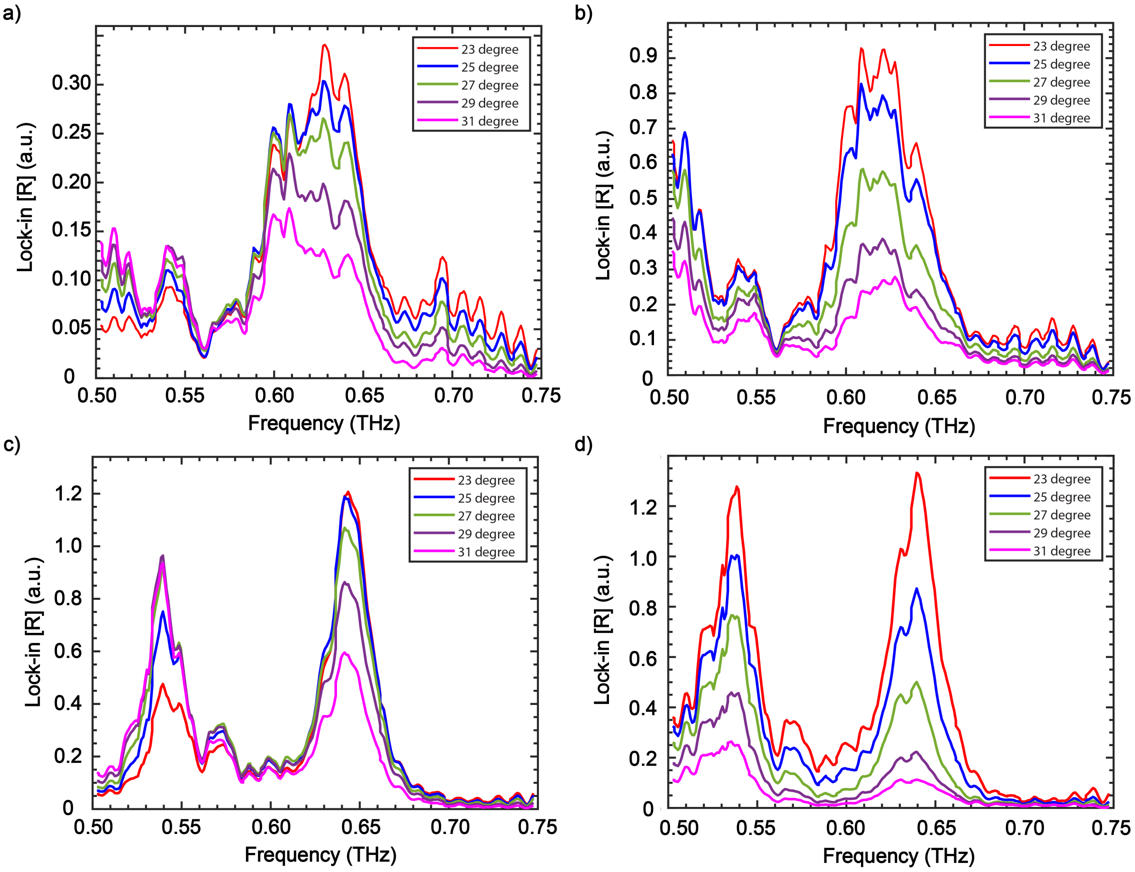

Figure 5.7. Raw results of the samples' full-spectrum measurements taken at various angles. a) Checkerboard pattern (60-90 μm). b) Stripe pattern (60-90 μm). c) Checkerboard pattern (70-90 μm). d) Stripe pattern (70-90 μm) (Noori et al., 2023).

THz which is approximately consistent compared with calculation result, 28° for 0.570 THz which is the same result as the calculations, 25° for 0.634 THz which is also the same as a calculated result, and 23° for 0.665 THz which is 1° less than the expected result that could be due to experimental error. The CST simulation findings for the other checkerboarded sample with unit cell sizes of 70-90 μm at Figure 5.5(c) reveal that there are two frequencies with a 180° phase difference. These frequencies are 0.528 THz and 0.550 THz as well as one at almost 0.640 THz where the reflection phase difference is approximately 165°. The calculated reflection angles results related to these frequencies are 30°, 29°, and 24°, respectively. The measurement results indicate that for 0.528 THz, the measured angle (Figure 5.8(c)) is 30° and 31° which are approximately similar to the calculated result. For 0.550 THz it is also 30°, which is only slightly different from the theoretical 29°, and also it is the maximum at the wide area from 26° until 29°. For the

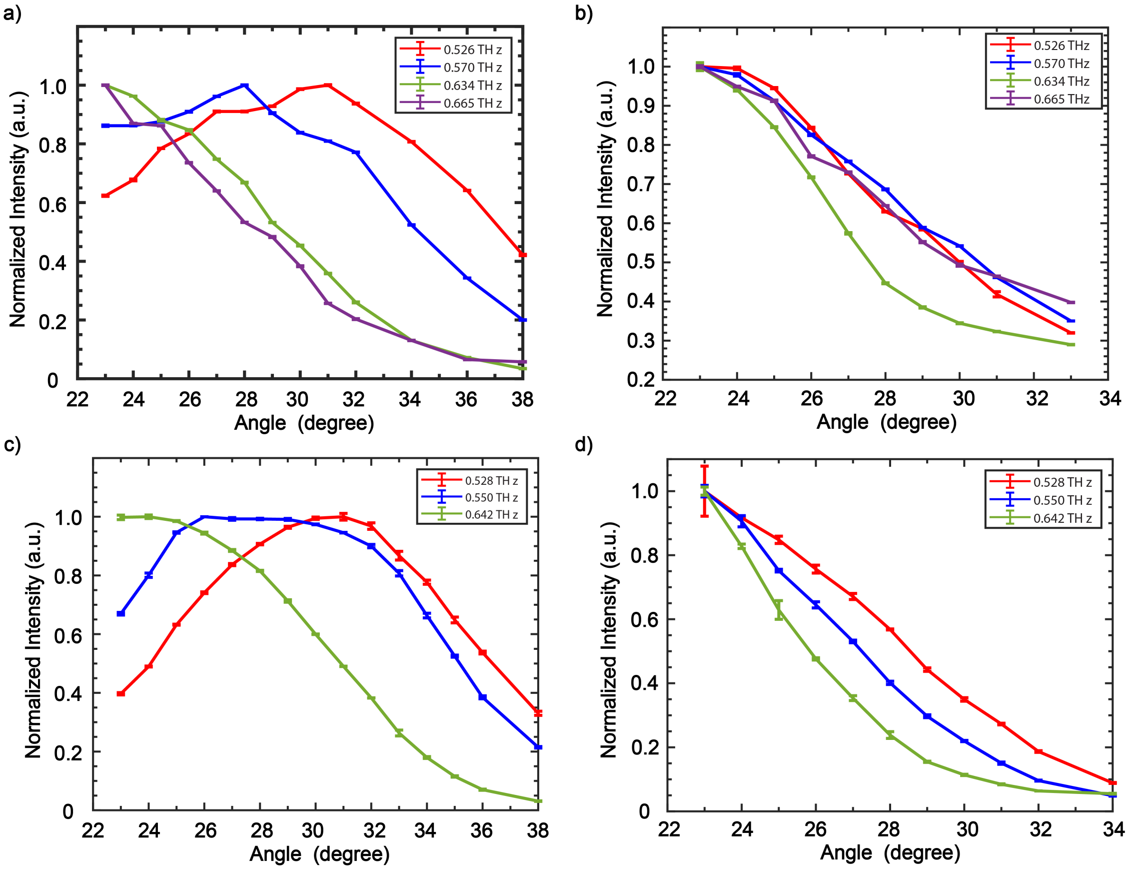

Figure 5.8. The behavior of normalized intensity of specific frequencies at various angles. a) Checkerboard pattern (60-90 µm). b) Stripe pattern (60-90 µm). c) Checkerboard pattern (70-90 µm). d) Stripe pattern (70-90 µm) (Noori et al., 2023).

last frequency of 0.640 THz, the obtained result is 23° and 24°, which is also roughly consistent with the calculated results. These results indicate a wider measured angle also, which could be due to the larger metallic gold patch. For the stripe pattern with the unit cell of 60-90 µm Figure 5.8(b), for the frequencies 0.520, 0.570, 0.634, and 0.665 THz, the maximum reflection angles are obtained (Eq. 2.16) as 21°, 19°, 17°, and 16°, respectively. For the stripe pattern with the unit cell of 70-90 µm Figure 5.8(d), for the frequencies 0.528, 0.550, and 0.640 THz, the reflection angles are obtained as 21°, 20°, and 17°, respectively. These angles are less than 23° and cannot be measured with this system configuration.

5.2. VO_2-based coded MM for THz wavefront engineering

Phase change materials, including graphene (Qi et al., 2020), liquid crystals (Lee et al., 2018), GST (Germanium Antimony Telluride, Ge3Sb2Te6) (Chen et al., 2009; Patel and Parmar, 2021; Wei et al., 2019), and vanadium dioxide (Huang et al., 2020; Wu et al., 2021; Yang et al., 2022) have been studied as tunable material for MM applications. When compared to volumetric vanadium dioxide, graphene has a very short switching time (Shabanpour et al., 2020) and demonstrates a significant loss (Wang et al., 2018). In the THz range, liquid crystals are unable to properly transition from insulator to metal (Wang et al., 2018). VO_2 is a reversible metal-insulator phase transition material with a $68°$C phase transition temperature.

A research team (Erçağlar et al., 2021) theoretically demonstrated an all-dielectric gradient MM with periodic arrays. They created a MM with π radian phase delay differences using SiO_2 substrate and binary Si microcylinders. A SiO_2 film served as a spacer layer between the VO_2 layer and two microcylinders in this configuration. Their proposed MM has various functions in the terahertz region: When TM and TE polarized light are exposed to radiation at 0.66-0.77 THz, transmission and double beam splitting take place. When VO_2 is in an insulating condition, this transmission double beam splitting happens. At 1.0 to 1.5 THz, the MM turns into a reflecting beam splitter when VO_2 is metallic. Their MM is insensitive to polarization. To the best of our knowledge, the VO_2 based coding MM for anomalous reflection in the THz area has not been the subject of experimental research.

In this section also the simulation, design, and fabrication of the coding VO_2-based MM is presented in which the switching of the VO_2 between the conductive and insulator mode is activated using 915 nm laser beam.

5.2.1. VO_2 MIT Modulation

The resistance of the samples was measured as the temperature-dependent resistance with four probe stations and explained in Chapter 4. Then the experimental conductivity was calculated using these data.

Figure 5.9 shows a comparison of measured (from Figure 4.1(a)) and calculated VO_2 conductivity using Eq. 2.9. As shown in the figure, the electrical conductivity measured in the lab has a steeper slope than the calculated results. In order to fit the exper-

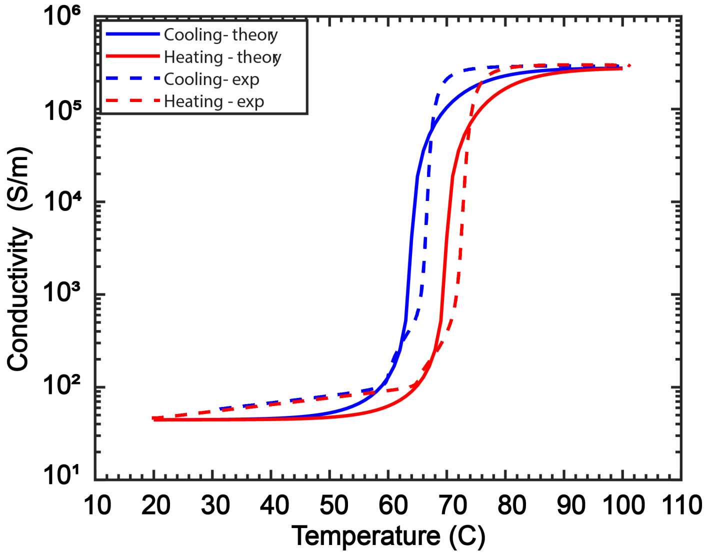

Figure 5.9. Temperature dependent conductivity of VO_2 in obtained using Eq. 2.9 comparing with the experimental conductivity values obtained (from Figure 4.1(a)) using the Four-Probe system in our laboratory.

imental conductivity with the calculated values, the following parameters were used as input into the filling fraction (Eq. 2.8) at 0.1 THz. The T_0= 68 °C is considered for cooling temperature and the T_0= 74°C is considered for heating temperature. For these values, the VO_2 conductivity at RT is obtained as 45 S/m at 25 °C and in 100 °C, is obtained as 2.77×10^5 (Figure 5.9).

There are different techniques for triggering the MIT transition in VO_2: doping (Asayesh-Ardakani et al., 2015; Joy et al., 2020; Muller et al., 2020; Tan et al., 2012), electrical excitation (Chen et al., 2021; He et al., 2015; Jeong et al., 2013; Kim et al., 2005; Leroy et al., 2012), optical excitation (Becker et al., 1996; Briggs et al., 2010; Cavalleri et al., 2001; Roach and Balberg, 1971; Zhang et al., 2019) and strain (Cao et al., 2009; Hu et al., 2010; Park et al., 2013). In this thesis, an optical modulation technique was used.

5.2.1.1. Optical Excitation

For the first time, Becker et al. modulated the VO_2 MIT transition in 1994 using optical excitation (Becker et al., 1994). A wide range of EM waves can trigger the MIT of VO_2 film including continuous waves (CW) and pulsed waves, ranging from UV, visible, and infrared to THz waves (Lu et al., 2021). By applying a laser, the insulating band gap is collapsed by electron excitation, resulting in VO_2 becoming metallic. In essence, it involves the transfer of photon energy through photoelectron phonons (Shao et al., 2018). However, the exact reason why the VO_2 becomes metallic is not yet known. The phase changes may have occurred due to electronic correlations being disrupted or they may have occurred due to structural distortions (Otto et al., 2019). Using EM waves as external stimuli, the photoinduced MIT process is triggered by two different mechanisms (Zhai et al., 2018): The slow photothermal effect and the fast photodoping effect. In the case of CW lasers, the mechanism that triggers MIT is called the photothermal effect, and the measurement response time ranges from microseconds to seconds (Lu et al., 2021). The photodoping process occurs extremely rapidly, and the MIT can be activated by an intense FS pulse laser within 1 picosecond (Lu et al., 2021).

The device structure was explained after studying the conductivity of the VO_2. In order to explain how the VO_2 reflection phase can be modified by changing the conductivity of the VO_2, the following section means section 5.2.2 was studied. The CST software was used to simulate the reflection amplitude and phase of the proposed MM.

5.2.2. Temperature-dependent Reflection Phase

The first concept for creating a VO_2-based MM in this thesis was to employ a single unit cell means 1-bit (Figure 5.10), and one could create a 0-bit unit cell by increasing the sample's temperature (modulating the VO_2 transition).

It was necessary to initially conduct research utilizing the CST simulation to examine the temperature-dependent reflection phase of the suggested structure. A DMD may be utilized to selectively adjust the VO_2 conductivity and obtain the desired scattering pattern for this proposed MM. The measurement setup employed to determine the MM's anomalous reflection angle is the same as that employed in the hard-coded section (Figure 5.4). In order to alter the conductivity of the VO_2, a laser pump of the CCMI module with a 45 W, 915 nm laser diode, and a 1.3 cm diameter output was employed. Additionally, a Texas Instruments digital micromirror device (DMD DLP650LNIR) was employed to regulate the illumination region. DMD could be patterned with a computer. The pattern will subsequently be transferred to the sample once the laser is shone onto the DMD (Figure 5.11). By beaming the patterned laser onto the samples, which were initially made up of only a single 1-bit unit cell (Figure 5.12). The unit cells that are illuminated with a laser become 0-bit, while the remaining unit cells stay 1-bit. Using this

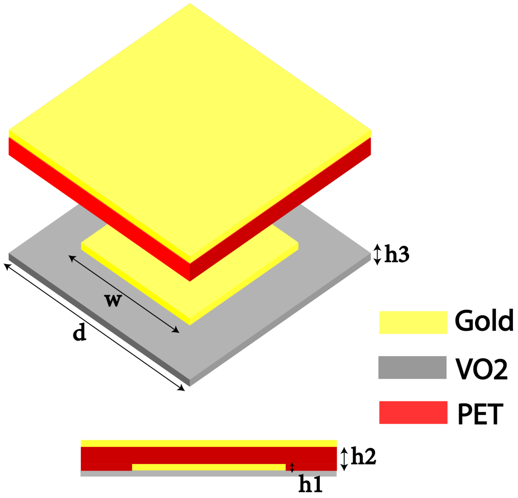

Figure 5.10. Simulated structure in order to investigate the temperature-dependent reflection phase properties of the VO_2 layer. Geometrical parameters: gold patch width is w= 60 µm (1-bit) with the thickness of 80 nm, the VO_2 side is d= 90 µm with the thickness of h3= 100 nm, the PET layer thickness is 25 µm.

technology, a remarkable tunable digital MM with multiple functionalities may be created due to the freedom of developing different DMD patterns. DMD was also used by other researchers (Yin et al., 2022) to modulate the Si layer in their MM.

To determine the reflection phase difference and reflection amplitude for the 1-bit unit cell prior to fabrication, a CST simulation was run. In order to facilitate the simulation speed, the thickness of the sapphire substrate is considered zero. In other words, it is better to mention that the effect of the substrate is not considered, and the actual simulated unit cell is presented in Figure 5.10. There is a 1-bit unit cell, with a gold patch side size of 60 µm. The geometrical parameters are identical to the hard-coded sample, with a VO_2 layer with a side of d= 90 µm that is simulated using its conductivity values. The sample is simulated at the different cooling and heating processes, and the conductivity values are obtained from the result demonstrated in Figure 5.9. The simulation was run from 60°C to 75°C with the step of 1 degree in addition to the 31°C at near room temperature (the experimental data was used, for the cooling process, the minimum measured temperature was 31°C). As It has shown in Figure 5.9, there is not much difference between the experimental and calculated conductivity values. For this section, the experimentally obtained conductivity values of VO_2 as input for the CST software were used.

Figure 5.13 and 5.14 represent the simulation reflection phase and amplitude of the cooling and heating process, respectively. To recognize the 180° of the phase differ-

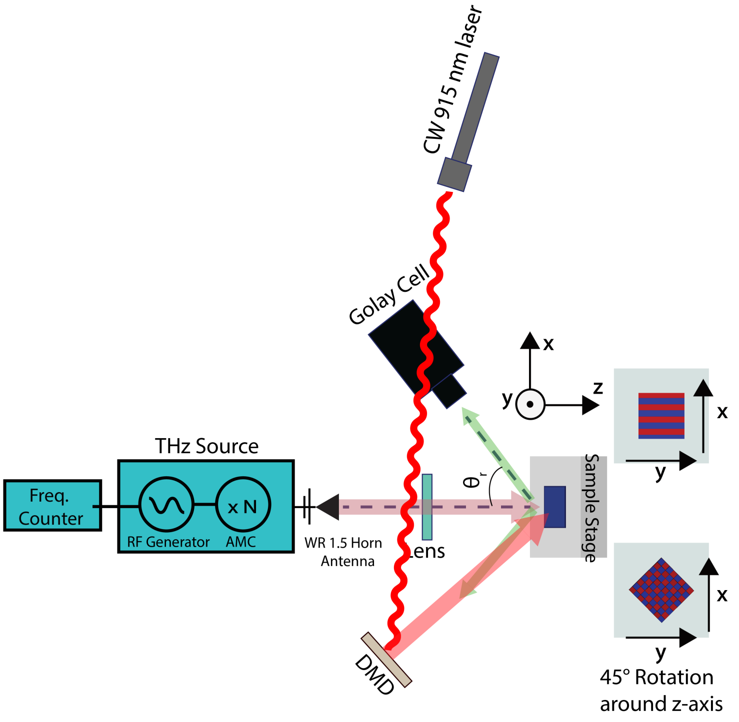

Figure 5.11. Schematic image of the reflection system with DMD and CW laser pump.

ence between the insulator and conductor phases of VO_2, the y-axis of phase and phase difference graphs is divided by 180. Figure 5.13(a and b) depicts how the reflection phase and amplitude fluctuate with temperature during the cooling process. The reflection phase and amplitude between 31°C, 60°C, and 65°C are almost identical. Also for the 68°C and 69°C until 72°C. Thus, it is decided to display a few of them. Alternatively, just the temperatures in which there is a change in the reflection phase are displayed. Figure 5.15(a and b), demonstrate the phase difference for the cooling and heating process, respectively. The phase difference versus frequency between the insulator and conductor modes of the unit cell's VO_2 layer is shown in Figure 5.15. The phase differences graphs demonstrate that as the temperature rises, for one specific frequency, the phase difference is increasing, for example, at 0.95 THz, increasing from 66°C to 67°C, the phase differences jump from 0 to 180°. To make this issue easier to understand, the phase difference for various temperatures for specific frequencies is demonstrated in Figure 5.16.

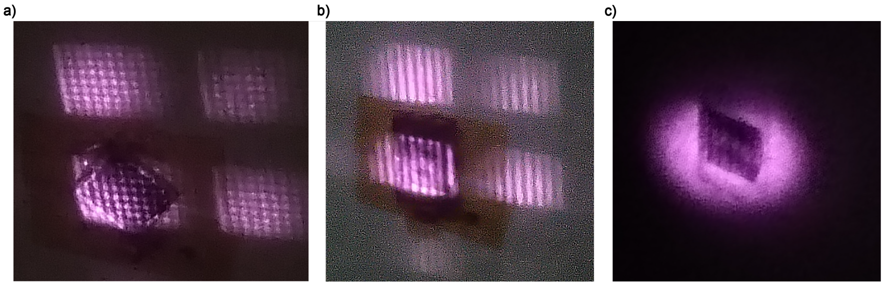

Figure 5.12. Adjusting CW laser, using a patterned DMD onto samples. a) Checkerboarded sample. b) Stripe sample. c) Direct exposure of the laser over the sample.

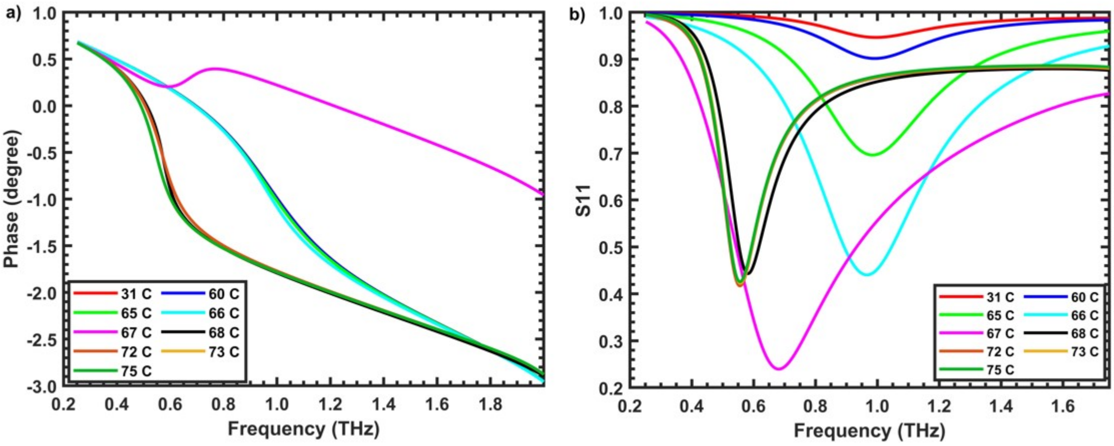

Figure 5.13. For the cooling process. a) Reflection phase b) Reflection amplitude.

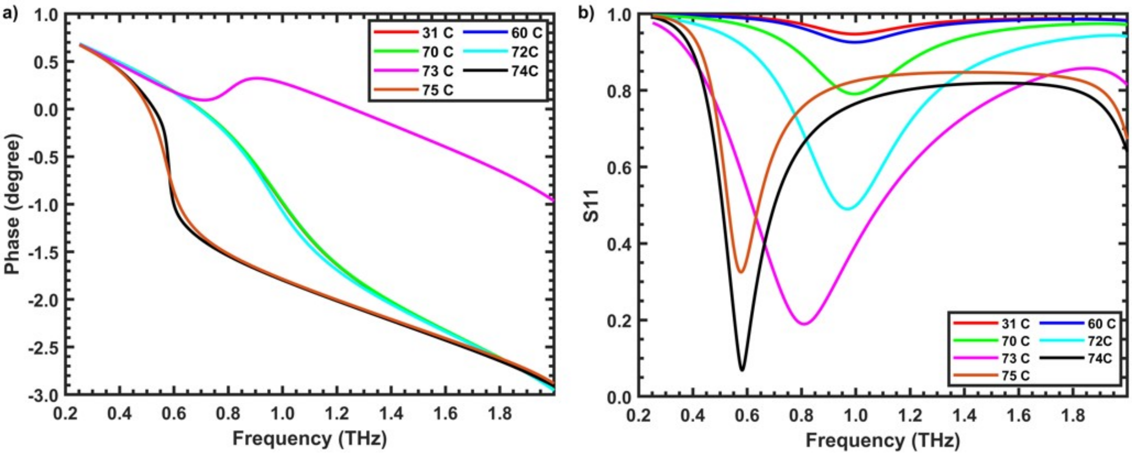

Figure 5.14. For the heating process. a) Reflection phase b) Reflection amplitude.

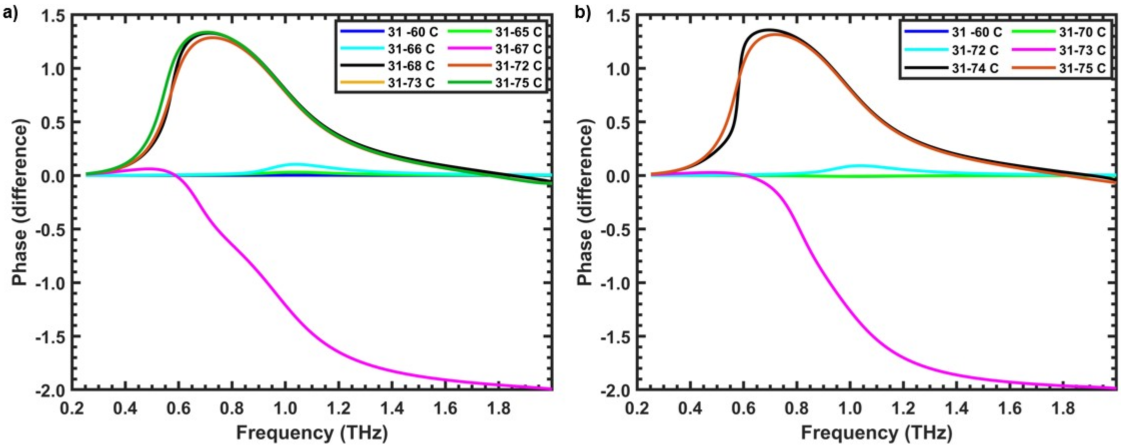

Figure 5.15. Phase difference between the insulator and conductor modes of the unit cell. a) Cooling process. b) Heating process.

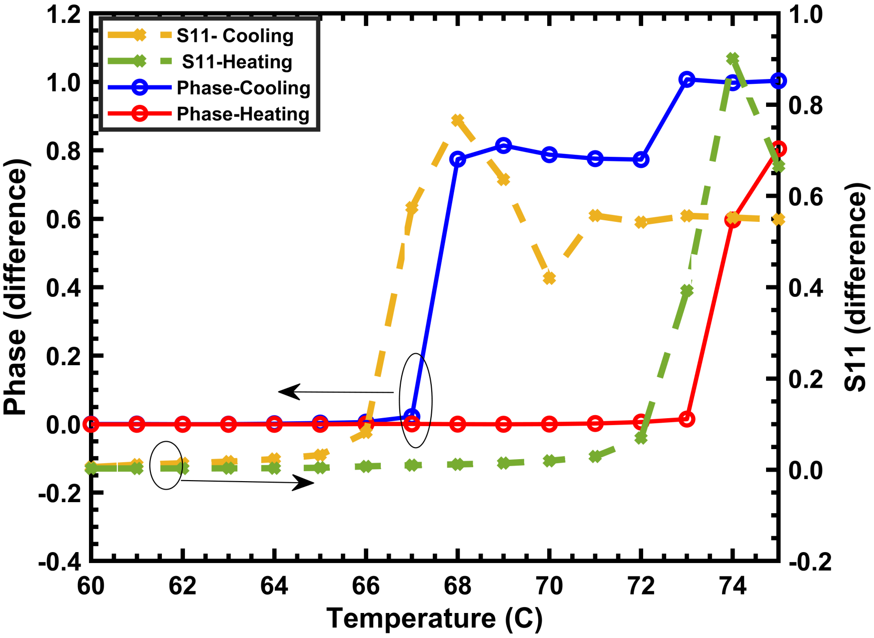

Figure 5.16. The phase difference and S11 differences at different temperatures at the specific frequency of 0.572 THz (where there is a 180° phase difference) for the cooling and heating process.

Figure 5.16 shows clearly the phase difference and S11 difference both behave as hysteresis for the cooling and heating process for a specific frequency. This idea helps us to understand, also it is possible to create and design a MM VO_2-based unit cell and modify its reflection phase by slightly altering the temperature at a specific frequency. Figure 5.16, shows that at a frequency of 0.572, there is a 180° phase difference between the 31°C and 73°C (1-bit and 0-bit) in the cooling process, but the amplitude difference between the 31°C and 73°C is greater than 0.5. In order to have a strong scattering pattern when solving the array factor equation, the reflection amplitude between the 0-bit and 1-bit must be nearly identical. When the amplitudes of the coding unit cells have a large difference, a huge lobe appears in the middle of the scattering pattern. The notion of employing the DMD and creating one sort of unit cell (1-bit) did not work out according to the simulation results with the suggested 1-bit unit cell.

This outcome compelled us to develop VO_2-based unit cells with 0 and 1 bits. It indicates that the samples have previously been patterned as checkerboard and stripe. The scattering pattern then diminishes when a CW laser is shone directly at the sample as shown in Figure 5.12(c). The next section explains the unit cell design and the outcomes.

5.2.3. Unit cell Design

Figure 5.17 depicts a schematic view of the fabricated MM. The suggested MM has the potential to regulate the phase. The only difference between the structure and geometries of this MM and the one explained in the previous chapter is the presence of a VO_2 layer embedded between the sapphire and the metallic gold patch. As it is seen in Figure 5.17, the MM, is a multi-layer structure. It is illuminated from the sapphire side. C-cut sapphire with is employed as the substrate. A square patterned VO_2 layer with the side length of 90 μm is on top of the sapphire in both 0-bit and 1-bit structure, and a square patterned gold layer with the side length of 90 μm (as ”0”) and 60 μm (as ”1”) is above it. The ground layer and the gold patch were separated by a PET layer. Sapphire was simulated with $\varepsilon = 9.61$ and $\mu = 1$. The material properties of the gold layer were taken from the CST material library. Spacer PET layer with the $\varepsilon = 2.54$ and $\mu = 1$ was simulated. The VO_2 was simulated as normal material with $\varepsilon = 9$ and $\mu = 1$ and with different conductivity values as 45 S/m for room temperature and 2.77×10^5 S/m for the conductive mode of the film. The geometry sizes of the unit cells are w1=90 μm, w2=60 μm, and d =100 μm is the periodicity of the unit cell. The thickness of the sapphire substrate, VO_2 film, gold patch, PET, and the gold ground layer are 430 μm, 100 nm, 80 nm, 25 µm, and 80 nm, respectively.

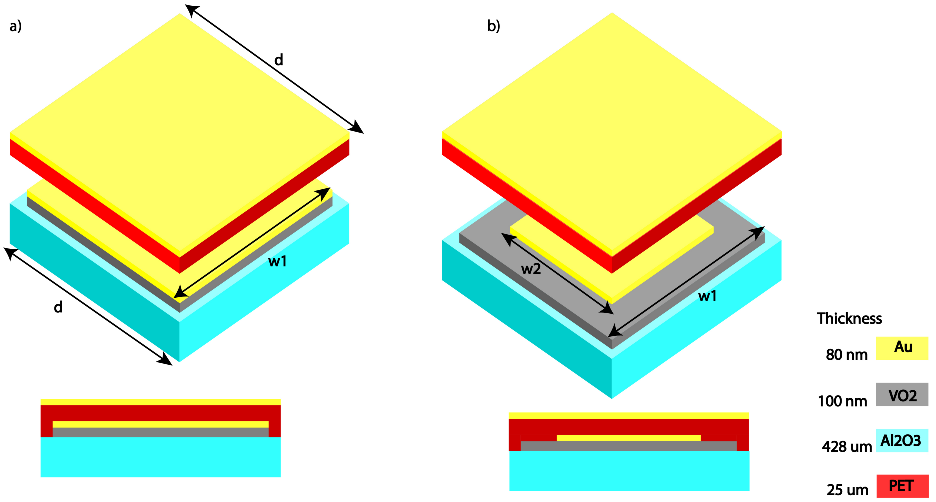

Figure 5.17. The VO_2-based unit cell is depicted schematically. The VO_2 is patterned as a square with a side of 90 µm. a) A 0-bit unit cell has an Au layer with a side length of 90 µm. b) A 1-bit unit cell has an Au layer with a side length of 60 µm.

The VO_2 film could be simulated using a variety of methods. The Drude model could be used to simulate the VO_2 (Jiang et al., 2022; Ren and Tang, 2021; Wang et al., 2020) but conductivity values utilized in the conductivity-dependent plasma frequencies should be the bulk values rather than the DC conductivity values, hence one should be cautious when employing Drude's model. As material attributes in CST, the conductivity values of VO_2 have also been used in other studies (Shabanpour et al., 2020; Zhang et al., 2017).

5.2.3.1. Fabrication Process

The geometry for two unit cells of different sizes was simulated by CST microwave studio software to provide 180° out-of-phase condition between the 0-1 bit unit cells. The 1-bit unit cell structure is made up of 60 × 60 µm^2 gold patches fabricated on 90 × 90 µm^2 VO_2 patches, while the 0-bit unit cell structure is made up of 90 × 90 µm^2 gold patches fabricated on 90 × 90 µm^2 VO_2 patches. MM is composed of 10 × 10 supercells, with each supercell made up of 8 × 8 unit cells.

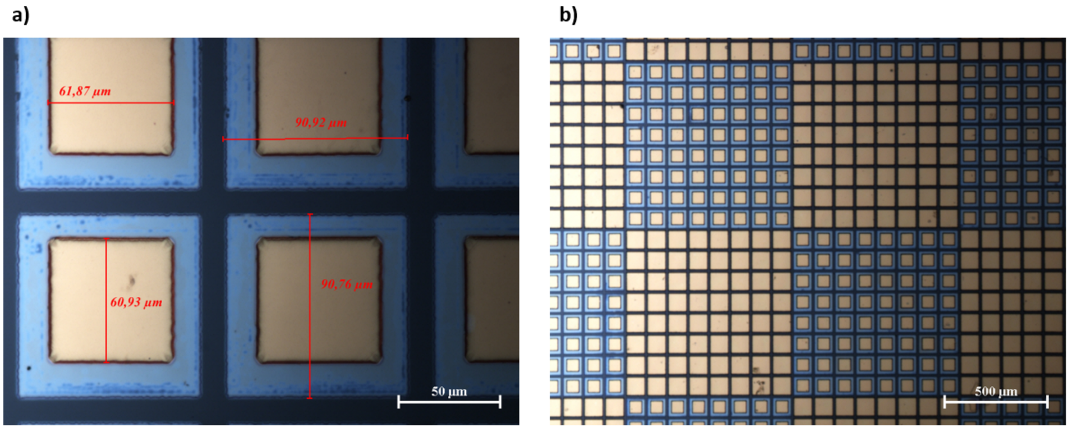

Figure 5.18. Optical images of the checkerboarded sample following two steps photolithography and dry etching. a) The optical image with 20X resolution. b) 5X resolution.

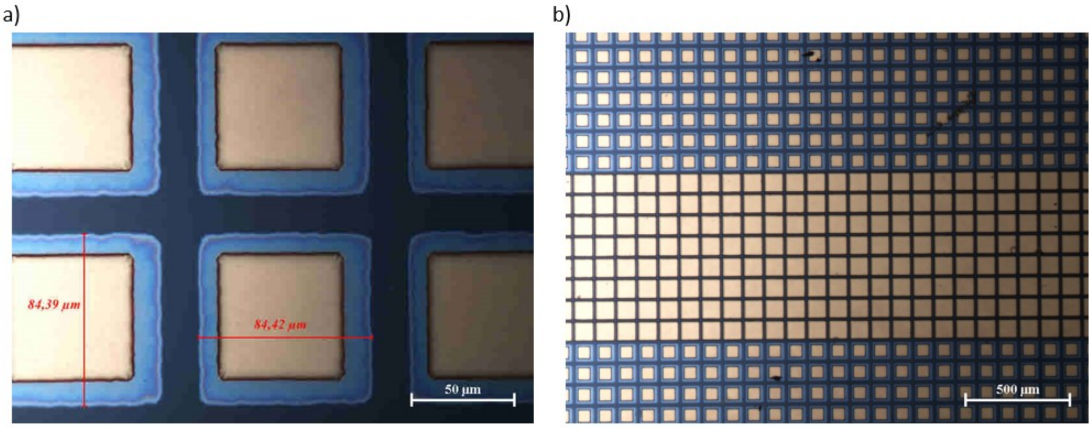

Figure 5.19. Optical images of the striped sample following two steps photolithography and dry etching. a) The optical image with 20X resolution. b) 5X resolution.

Unit cells were created as follows: First, VO_2 thin film was grown utilizing DC magnetron sputtering on top of the c-cut sapphire substrate. The 90×90 μm^2 VO_2 patch squares were then created using a traditional photolithography procedure followed by dry etching. Thermal evaporation was used to deposit the gold layer on top of the patterned VO_2 film in order to create the square gold patches. Photolithography, followed by dry etching, was also used to pattern this gold layer (Figure 5.18 and 5.19). After that, a 25 μm PET sheet was laminated to the gold patch side. Finally, a gold ground layer was fabricated on the back side of the device using thermal evaporation to achieve MM reflection. Here also, two different patterns were used: stripe and checkerboard structures.

5.2.3.2. Measurement Set up

Measurements were done using the direct laser exposure, with the setup illustrated in Figure 5.20.

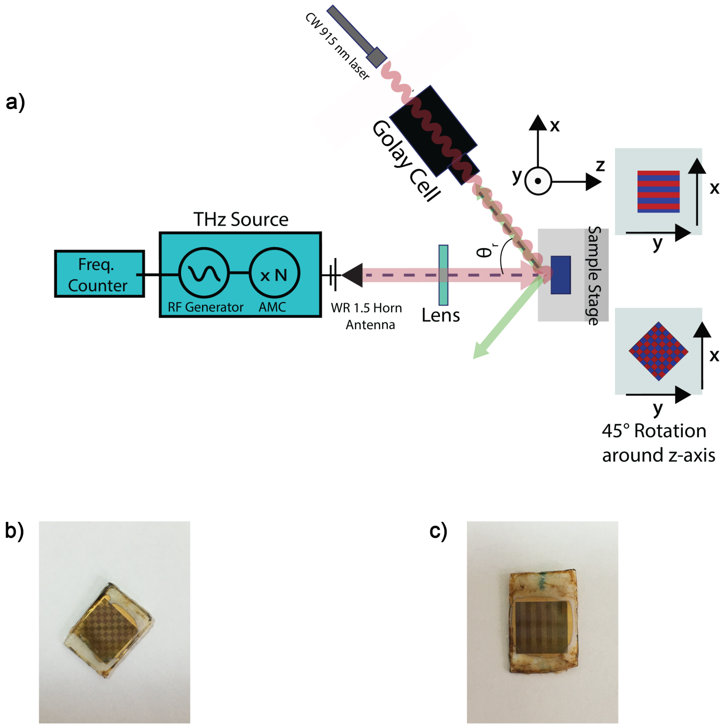

Figure 5.20. a) System with direct laser exposure. b) The fabricated checkerboarded pattern. c) the fabricated stripe pattern.

In this thesis, the result of using direct exposure was investigated. A pump laser was used to illuminate the sample. The laser was shone onto the sample at the same angle that the detector was positioned, as could be observed from the measurement setup.

5.2.4. Result and Discussion

5.2.4.1. Simulation

Figure 5.21 and 5.22 depict the CST simulation result for the 0-bit and 1-bit unit cells. The proposed unit cell was a VO_2 with a side length of 90 µm, but after the photolithography, the VO_2 pattern size for the stripe pattern obtained at 85 µm as it could be seen in Figure 5.19.

So the simulation is performed with a unit cell size of gold patch size of 60 µm and 90 µm with a VO_2 size of 90 µm for two different VO_2 states: when VO_2 is at RT (Figure 5.21(a and b)) and when VO_2 is at its conductive mode (Figure 5.21(c and d)). Also, a unit cell with a gold patch size of 60 µm and a 90 µm VO_2 patches with a VO_2 size of 85 µm for two different VO_2 states: when VO_2 is at RT (Figure 5.22(a and b)) and when VO_2 is at its conductive mode (Figure 5.22(c and d)). As shown in Figures 5.21(a) and 5.22(a) at the insulating mode of the VO_2, there is a π phase shift between the two unit cell and Figures 5.21(c) and 5.22(c), the reflection phase difference of 180° vanishes as VO_2 conductivity rises. According to the simulation, we expect to have a 180° phase difference at 4 different frequencies for the checkerboard pattern, at almost 0.525, 0.553, 0.637, and 0.644 THz for the sample with 90 µm of VO_2 side. Also, for the VO_2 side of 85 µm, the phase difference of 180° was achieved at 0.526, 0.550, and 176° at 0.640 THz. The CST finding demonstrates that at VO_2 insulating mode, it is expected to observe a beam splitting behavior, just similar to the hard-coded MM, and while turning the VO_2 layer to a conductor phase, reflected beam, is expected to vanish as the phase difference of 180° disappear. The sum interference between the reflections from S11(1 bit) and S11(0 bit) is used to compute the resultant reflected intensity as shown in Figures 5.21(b and d) and 5.22(b and d). The expected resonances occur near frequencies 0.525, 0.553 THz, and a wider region around 0.637 and 0.644 THz for 60-90 µm and VO_2 size of 90 µm case (Figure 5.21(b)). For the 60-90 µm and VO_2 size of 85 µm case (Figure 5.22(b)) the expected resonances occur at 0.526, 0.550, and 0.640 THz.

The resultant phase differences and reflection amplitude values will then be used as input in MATLAB to calculate the elevation angles from the Eqs. 2.16 and 2.17 and to

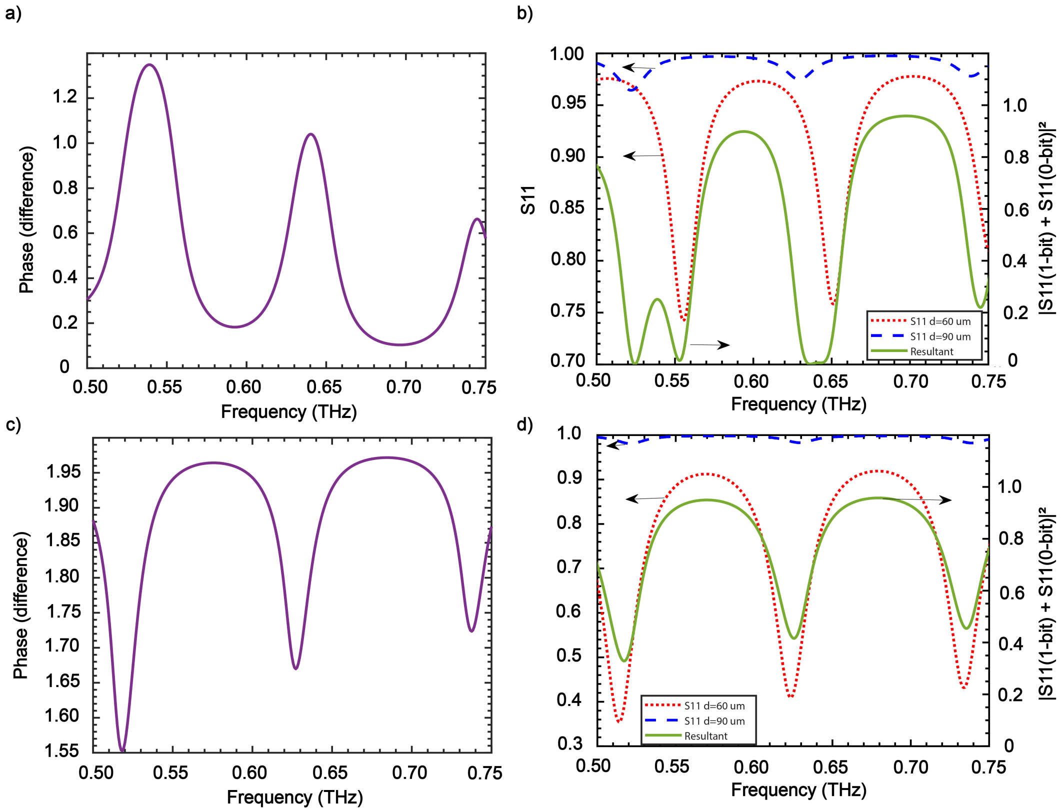

Figure 5.21. CST simulation result of 1-bit (60 µm) and 0-bit (90 µm) unit cells for the checkerboard pattern with the VO_2 side of 90 µm. a) Reflection phase difference when VO_2 is at room temperature (Conductivity 45 S/m). b) Respective reflection amplitude (left axis) and combined reflected intensity (right axis) when VO_2 is at room temperature (Conductivity 45 S/m). c) Reflection phase difference when VO_2 is its conductive mode (Conductivity 2.7×10^5 S/m). d) Respective reflection amplitude (left axis) and combined reflected intensity (right axis) when VO_2 is in its conductive mode (Conductivity 2.7×10^5 S/m).

obtain normalized intensity graphs versus reflection angles. From Eq. 2.17 the expected reflection angle for the checkerboard pattern, is expected as 30°, 29°, 25°, and 24° for 0.525, 0.553, 0.637, and 0.644 THz, respectively. For the stripe pattern, the expected reflection angles obtained from the Eq. 2.16, are 21°, 20°, and 17° for 0.526, 0.550, and 0.640 THz, respectively. There is less than approximately 1° difference between the results obtained from the Eqs. 2.16 and 2.17 and the normalized intensity presented in Figures 5.23(a and b).

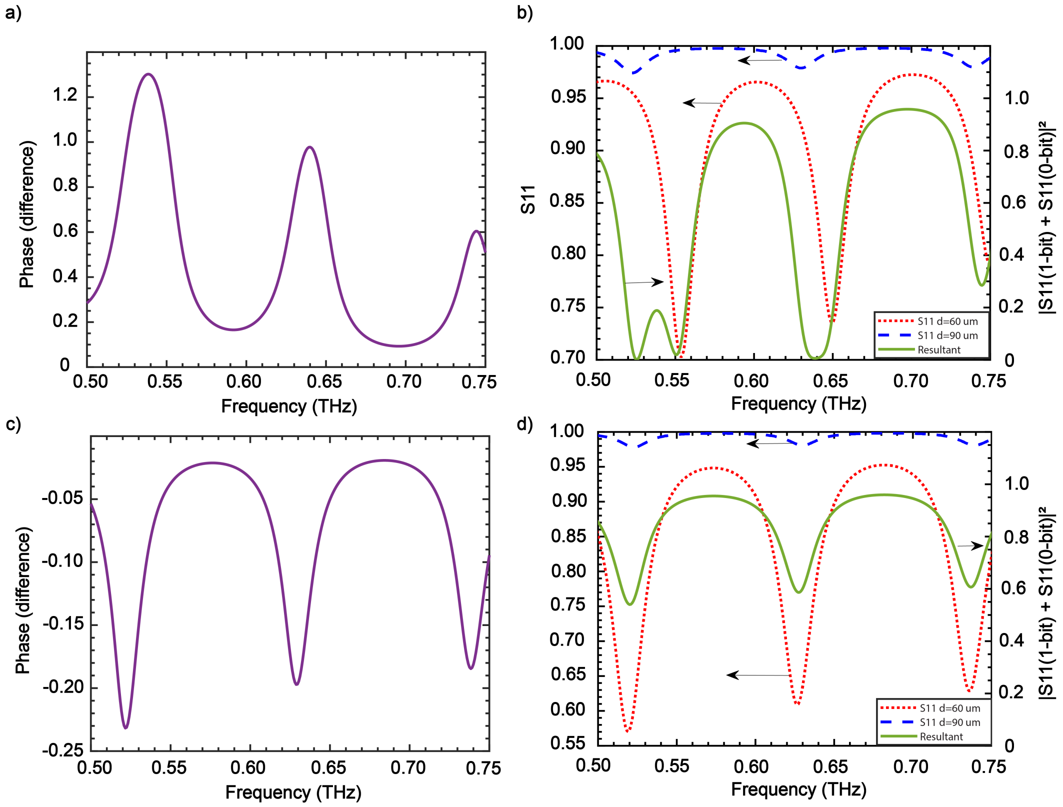

Figure 5.22. CST simulation result of 1-bit (60 µm) and 0-bit (90 µm) unit cells for the stripe pattern with the VO_2 side of 85 µm. a) Reflection phase difference when VO_2 is at room temperature (Conductivity 45 S/m). b) Respective reflection amplitude (left axis) and combined reflected intensity (right axis) when VO_2 is at room temperature (Conductivity 45 S/m). c) Reflection phase difference when VO_2 is at conductive mode (Conductivity 2.77×10^5 S/m). d) Respective reflection amplitude and combined reflected intensity (right axis) when VO_2 is at conductive mode (Conductivity 2.77×10^5 S/m).

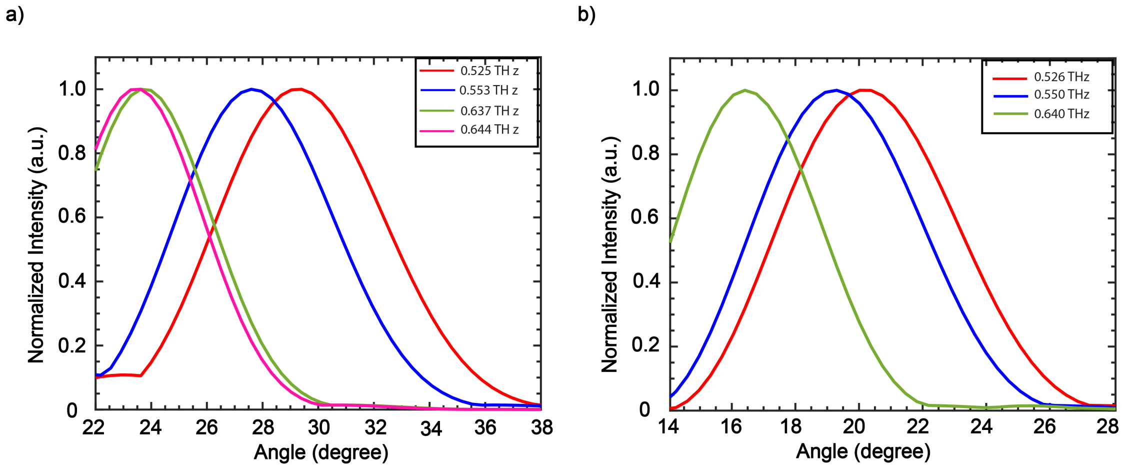

Figure 5.23. Normalized intensity graphs versus deflection angle obtained from MATLAB analytical calculations. a) The checkerboard pattern (The VO_2 side of 90 µm). b) The stripe pattern (The VO_2 side of 85 µm).

5.2.4.2. Experimental Result and Discussion

Figures 5.24(a and b) illustrate the whole spectrum of the checkerboard and stripe patterns when the detector is positioned at various angles while the sample is at room temperature. Figures 5.24(c and d) show the corresponding normalized intensity versus reflection angles for each frequency.

From Figure 5.24(c), the measured reflection angle for the checkerboard patterns, are 32° and 33° for 0.525 THz, which is 2° and 3° higher than the calculated value that is 30°. For 0.553 THz, the measured reflection angles are 32° which is 3° higher than the calculated value, meaning 29°. For 0.637 THz, the measured angles are 26° and 27°, which are also 1° and 2° higher than the calculated value which is 25°. For 0.644 THz, the measured angle is 27° and which is again 3° higher than the calculated values which is 24°.

The incident beam blockage in the setup configuration, which was also previously mentioned for the hard-coded stripe patterns (section 5.1), prevents measurements at angles lower than 23°. However, according to our results, it is possible to discuss the result for the stripe pattern. Figure 5.24(d), the maximum reflection angles for the 0.526 THz, 0.550 THz, and 0.640 THz are measured as 23°. According to the calculation result, the maximum reflection angle for these frequencies is 21°, 20°, and 17°, respectively.

The switching functionality of the MMs was examined using a 915 nm laser beam, as was described in the measurement section. In which the input current values were used

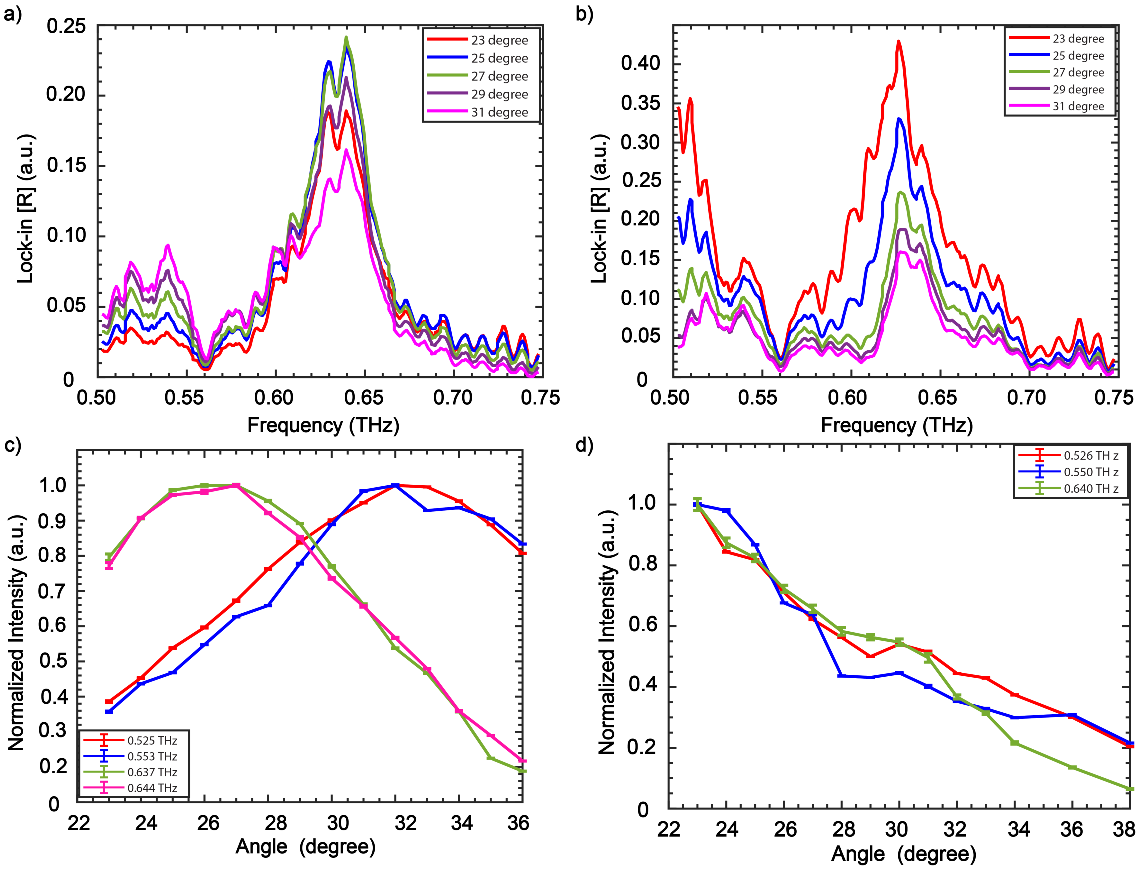

Figure 5.24. Full spectrum of the samples: a) checkerboard sample b) stripe sample. Normalized intensity vs reflection angles for certain frequencies: c) checkerboard sample, d) stripe sample.

to adjust the laser beam's power. It was found through experimentation that 1.5 A of current (equivalent to approximately 2.88 W) was sufficient to change the VO_2 conductivity layer in these samples. Figure 5.25(a) shows the checkerboard sample at 28° deflection angle at room temperature, and the red curve shows the result when the sample is exposed to a laser beam with a power of roughly 2.88 W. The intensity has obviously decreased as the VO_2 layer turns conductive. Figure 5.25(b) shows a stripe pattern measured at about 25°; the blue curve is measured while the sample is at ambient temperature and the VO_2 layer is in insulator mode, and the red curve is measured when the sample is exposed with a laser power of approximately 8.62 W. The data show a significant decrease in intensity following exposure. The larger current value was utilized for the laser illumination for the stripe pattern since after using the laser a few times over the sample, the VO_2 layer response to the laser was decreased, which could be owing to the low quality of the VO_2 layer.

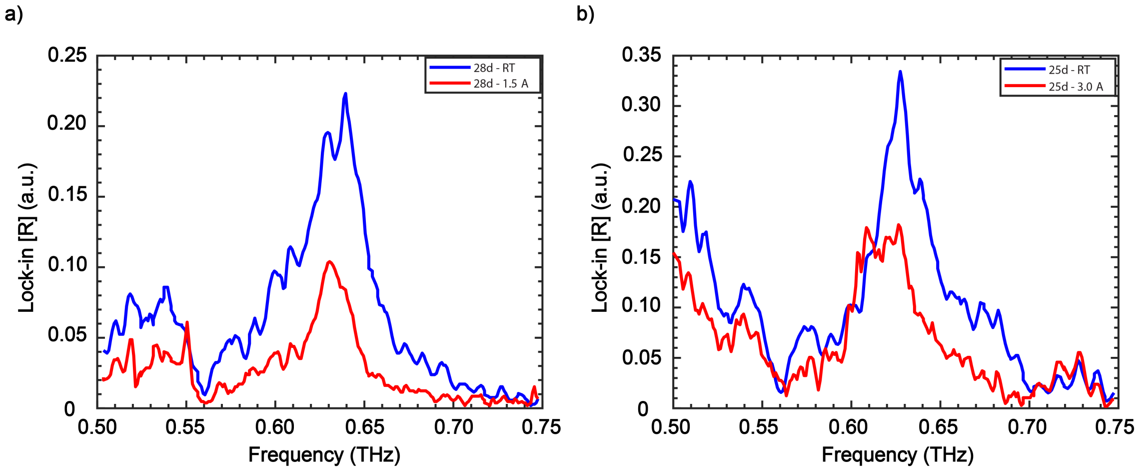

Figure 5.25. a) Spectrum of the checkerboard pattern at 28° detector position at room temperature (blue curve) and when the laser is exposed (red curve). b) Spectrum of the stripe pattern at 25° detector position at room temperature (blue curve) and when the laser is exposed (red curve)

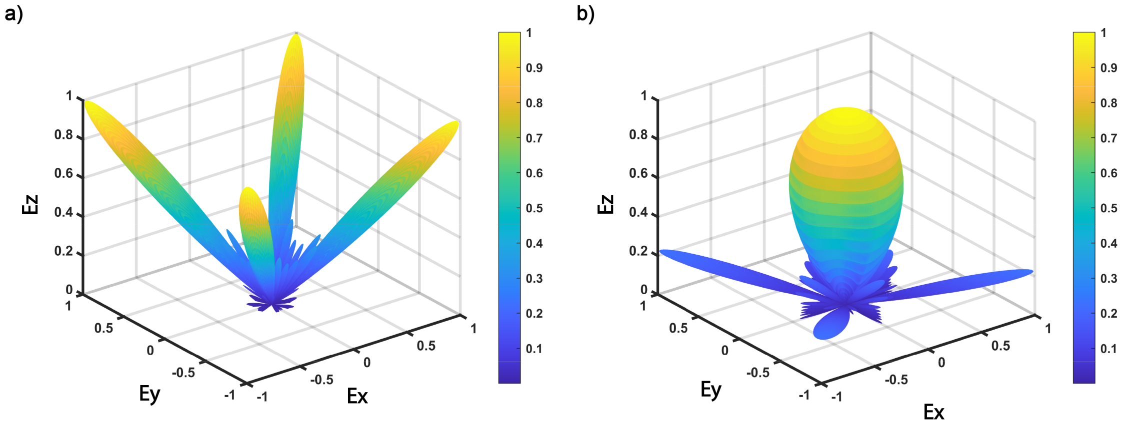

Figure 5.26. 3D scattering pattern for the checkerboarded sample at 0.525 THz obtained by solving array factor equation in MATLAB (the phase difference and the amplitude are obtained from Figure 5.22(c). a) When the sample is at room temperature. b) when the sample is illuminated by a laser.

The amplitude modulation depth (MD) was calculated (Gao et al., 2020) for the result shown in Figure 5.25 using the Eq. 5.1.

$$MD = \frac{(R_{rt}(\omega) - R_{cnd}(\omega))}{R_{rt}(\omega)} \tag{5.1}$$

For the checkerboard pattern at 0.639 THz (Figure 5.25(a), the maximum peak), the MD is about 62% and for the striped pattern at 0.627 THz (Figure 5.25(b), the maximum peak), the MD is about 46 $\%$.

The calculated scattering pattern for the specific frequencies for checkerboard samples confirms that as VO_2 became conductive, the 180° phase difference between the unit cells vanish, and also the difference between the amplitudes of the 0-bit and 1-bit increases, resulting in the disappearance of the scattering pattern, as shown in Figure 5.26. Figure 5.26(a), shows the scattering pattern of a checkerboard sample at 0.525 THz, with a 180° phase difference between the 1-bit and the 0-bit while the sample is at room temperature. Figure 5.26(b) represents the same sample scattering pattern when the sample is illuminated by a laser and causes a change in phase difference and the unit cells reflection amplitude as it is presented in Figure 5.22(c).

5.2.5. Conclusion

The section 5.1 presented a brief description of the fabrication process of coding beam splitter MM, as well as comprehensive simulation and their experimentation results. CST simulation was performed in order to modify the unit cells' geometrical characteristics in order to achieve the beam deflection functionality of the MM. The predicted radiation pattern and the normalized intensity were then calculated by Matlab for both the checkerboarded and stripe pattern using the CST findings to determine the far-field radiation of the MM using the array factor. After that, samples were fabricated and then measured between 0.50 and 0.75 THz at various angles. The presented THz MM successfully shows the operation of the beam deviation for the checkerboarded pattern both analytically and experimentally. THz beams can be split into four different anticipated directions. Due to the experimental measurement setup, it was not possible to measure the reflection angles of the expected frequencies of the stripe patterns, which would have shown a 180° of phase difference between the "0" and "1" bit unit cells.

The section 5.2.2 examined the VO_2 temperature-dependent reflection phase at specific frequencies which is expected to see a 180° phase difference between the 1-bit and the 0-bit. The discussion of VO_2-based samples followed (section 5.2.3), including their design, simulation, fabrication, and experimental results. The results show that the VO_2-based samples have the ability to switch ON/OFF. In which the beam spectrum was visible when the VO_2 layer was in the insulator mode, but the beam intensity decreases once the sample was stimulated with a CW laser beam shining directly on it. The reflection angles for the checkerboarded patterns were obtained and compared with the calculated values. The result indicates that the experimental reflection angles are on average 2°-3° higher than the calculated results. Also, the experimental results illustrate wider angles than the calculations. These findings are consistent with Eq. 2.17, which states that the reflection angle decreases as frequency increases.

It is worth noting that the simulation results are based on the assumption that the incident beam is a perfect plane wave, whereas the incident wave is not a perfect plane wave in reality. When the incident beam is focused over the surface of the sample via the lens, the wavefront becomes convex or concave, resulting in a widened reflection peak and decreased intensity (Liu et al., 2016; Zhang et al., 2016). As a result, the measured values differ from the analytically calculated values. Additionally, during fabrication, a slight misalignment (roughly 1 μm-2 μm) (Liu et al., 2016; Zhang et al., 2016) between the VO_2 layer and the gold patch layers, as well as other fabrication problems like laminating PET at a high temperature of the fabricated sample, may have contributed to the differences between the measured and simulated results.

CHAPTER 6

CONCLUSION

Terahertz waves are significant because of their unique properties, which allow them to be used in imaging, accurate spectroscopic analysis, secure communication, and scientific study. THz technological advances will result in new applications and discoveries in a wide range of sectors. To expand THz utilization, devices with the ability to manipulate THz waves must be developed. The objective of this thesis is to design 1-bit coding MMs, for the engineering of THz waveform with the potential application in THz communications. Two types of MMs were designed and fabricated and measured. The hard-coded (metal-based) MM and VO_2 based MM. Both have the same structure including a sapphire substrate, VO_2 layer (used in the VO_2 based MM), the gold layer as a metallic patch (coded as 0 and 1-bit), PET acting as a dielectric spacer, and a gold ground layer. 1-bit coding MMs are made of two unit cells coded as 0 and 1. The 1-bit unit cell is the one with the smaller gold patch side of 60 µm, while the 0-bit unit cell is the one with the larger gold patch side of 90 µm. The physical geometries of the unit cells were obtained using CST simulation to demonstrate 180° phase difference between the 0 and 1-bit unit cells in the frequency range of 0.50- 0.75 THz. The beam-splitting characteristic is determined by the sequence of the coded unit cells. The incident beam will split into two reflected beams with equal angles to the z-axis if the unit cells are patterned in a stripe design. The incident beam will split into four reflected beams with identical angles to the z-axis if the unit cells are patterned in a checkerboard design. The generalized Snell's law states that these reflection angles rely on both the physical size of the unit cell and the incident beam wavelength. Therefore, according to this law, one can modify the reflection angle by altering the periodicity or the physical size of the unit cell indicating that the characteristics of MM are driven by their geometries. Theoretical calculations were carried out in order to explore the reflection behavior of the proposed MM using MATLAB. The CST simulation was used to determine the reflection phase and amplitudes of the two coded unit cells, and the resulting values were entered as inputs into MATLAB equations to study the normalized intensity.

In the first step of the fabrication process, VO_2 was grown on the top of the sapphire substrate. During the growth step, more than 20 samples of VO_2 with an MIT transition magnitude greater than almost 10^3 were successfully grown. Variable characterization techniques were used to investigate the grown films including XRD, SEM, electrical characterization, and THz transmission using the CW laser in order to modulate the MIT. The geometry and size of the unit cell were obtained using CST simulation.

During the experiment procedure, a quartz mask was created. There were striped and checkerboard patterns with various cell sizes. Using this mask, the fabricated VO_2 layer was patterned by photolithography and three hours of etching. Every unit cell in the VO_2 patterned layer has a side of 90 µm. DEKTAK profilometry was used in order to determine the thickness of the patterned VO_2 after etching. THz transmission characterization were performed on the as grown VO_2 and patterned VO_2 samples. MIT modulation was done using CW 915 nm laser. According to the analysis's findings, the VO_2 layer has good transparency at room temperature and can be compared to sapphire; however, when VO_2 transforms into metallic, it completely blocks THz transmission. In other words, VO_2 film has a very good response to laser impact. These analyses were fully studied in Chapter 4.

After the THz characterization of the VO_2 layer, the gold layer was deposited by thermal evaporation on the top of the patterned VO_2, having a thickness of around 80 nm. The gold layer was patterned and etched for 10 minutes with an approximately 2 µm deviation error from the center of the patterned VO_2 unit cells. Then a PET layer was laminated on top of the gold patches using a furnace. Finally, the ground gold layer was deposited using thermal evaporation.

It is important to mention that the first intention of fabrication of VO_2 based MM was fabricating a tunable digital MM. In which, the MM could be designed entirely out of a single 1-bit unit cell and then the 0-bit unit cell could be obtained using a DMD and laser, by adjusting the conductivity of the VO_2 layer. However, the CST simulation results indicated that this suggested 1-bit unit cell is inefficient, due to having a discrepancy between the 1 and 0-bit unit cell's reflection amplitudes. As a result, the VO_2 based coded MM, fabricated as striped and checkerboarded designs. These samples were then measured at room temperature as well as while a laser radiated on them. The results showed that at room temperature, the samples can operate as beam splitters, reflecting the incident beam in a certain direction, and when the laser is turned on, the VO_2 turns conductive, and the scattering pattern is reduced. The expected outcome was that the scattering pattern would fade completely after laser exposure; however, in this case, the reason that the scattering pattern did not vanish could be related to the VO_2 layer's deteriorating quality following sample production and frequent laser usage on them. The beam-splitting functionality was observed at room temperature, for both checkerboarded and stripe patterns.

The deflection angle for the checkerboard pattern was measured between 2°-3° greater than the calculated results obtained from Snell's law. Aside from the VO_2 based MM, hard-coded MM were also fabricated, with the same structure as the VO_2 based MM but without the VO_2 layer inside. Two sets of the 1-bit coded samples of 60 (1-bit)-90 (0-bit) µm and 70 (1-bit)-90 (0-bit) µm were fabricated and measured. The measured deflection angles of the MMs showed that the checkerboard samples for both sets have a relatively good agreement with the calculated results. Also, the experimental finding suggests that the 70-90 µm has a wider reflected beam than the 60-90 µm MM. For the stripe patterns, the analytically calculated results indicate that the scattering occurs at angles less than 23°, which is not possible to measure them using this setup (For angles less than 23°, the incident beam is blocked by the detector).

The use of such affordable materials as polymers and metals with simple geometries as demonstrated here can be very beneficial for beam steering applications, which are predicted to become increasingly significant with the development of 6G and beyond technologies in the near future.

REFERENCES

Aetukuri, N. B., A. X. Gray, M. Drouard, M. Cossale, L. Gao, A. H. Reid, R. Kukreja, H. Ohldag, C. A. Jenkins, E. Arenholz, et al. (2013). Control of the metal–insulator transition in vanadium dioxide by modifying orbital occupancy. *Nature Physics 9*(10), 661–666.

Ahmadivand, A., B. Gerislioglu, and Z. Ramezani (2019). Gated graphene island-enabled tunable charge transfer plasmon terahertz metamodulator. *Nanoscale 11*(17), 8091–8095.

Akyildiz, I. F., C. Han, and S. Nie (2018). Combating the distance problem in the millimeter wave and terahertz frequency bands. *IEEE Communications Magazine 56*(6), 102–108.

Alaboz, H. (2018). *Magnetron sputter grown metal doped vanadium oxide thin films for terahertz bolometers*. Ph. D. thesis, Izmir Institute of Technology (Turkey).

Alves, F., D. Grbovic, B. Kearney, and G. Karunasiri (2012). Microelectromechanical systems bimaterial terahertz sensor with integrated metamaterial absorber. *Optics letters 37*(11), 1886–1888.

Asayesh-Ardakani, H., A. Nie, P. M. Marley, Y. Zhu, P. J. Phillips, S. Singh, F. Mashayek, G. Sambandamurthy, K.-b. Low, R. F. Klie, et al. (2015). Atomic origins of monoclinic-tetragonal (rutile) phase transition in doped vo2 nanowires. *Nano Letters 15*(11), 7179–7188.

Bai, Y., K. Chen, T. Bu, and S. Zhuang (2016). An electrically tunable terahertz metamaterial modulator with two independent channels. *Journal of Applied Physics 119*(12), 124505.

Becker, M. F., A. B. Buckman, R. M. Walser, T. Lepine, P. Georges, and A. Brun (1996). Femtosecond laser excitation dynamics of the semiconductor-metal phase transition in vo2. *Journal of Applied Physics 79*(5), 2404–2408.

Becker, M. F., A. B. Buckman, R. M. Walser, T. Lepine, P. M. Georges, and A. Brun (1994). Femtosecond switching of the solid state phase transition in the smart-system material vo2. In *Smart Structures and Materials 1994: Smart Materials*, Volume 2189, pp. 400–408. SPIE.

Born, M. and E. Wolf (2013). *Principles of optics: electromagnetic theory of propagation, interference and diffraction of light*. Elsevier.

Briggs, R. M., I. M. Pryce, and H. A. Atwater (2010). Compact silicon photonic waveguide modulator based on the vanadium dioxide metal-insulator phase transition. *Optics express 18*(11), 11192–11201.

Burla, M., C. Hoessbacher, W. Heni, C. Haffner, Y. Fedoryshyn, D. Werner, T. Watanabe, H. Massler, D. L. Elder, L. R. Dalton, et al. (2019). 500 ghz plasmonic mach-zehnder modulator enabling sub-thz microwave photonics. *Apl Photonics 4*(5), 056106.

Cai, X., R. Tang, H. Zhou, Q. Li, S. Ma, D. Wang, T. Liu, X. Ling, W. Tan, Q. He, et al. (2021). Dynamically controlling terahertz wavefronts with cascaded metasurfaces. *Advanced Photonics 3*(3), 036003.

Cao, J., E. Ertekin, V. Srinivasan, W. Fan, S. Huang, H. Zheng, J. Yim, D. Khanal, D. Ogletree, J. Grossman, et al. (2009). Strain engineering and one-dimensional organization of metal–insulator domains in single-crystal vanadium dioxide beams. *Nature nanotechnology 4*(11), 732–737.

Cavalleri, A., C. Tóth, C. W. Siders, J. Squier, F. Ráksi, P. Forget, and J. Kieffer (2001). Femtosecond structural dynamics in vo 2 during an ultrafast solid-solid phase transition. *Physical review letters 87*(23), 237401.

Chen, B., J. Wu, W. Li, C. Zhang, K. Fan, Q. Xue, Y. Chi, Q. Wen, B. Jin, J. Chen, et al. (2021). Programmable terahertz metamaterials with non-volatile memory. *Laser & Photonics Reviews*, 2100472.

Chen, H.-T., W. J. Padilla, M. J. Cich, A. K. Azad, R. D. Averitt, and A. J. Taylor (2009). A metamaterial solid-state terahertz phase modulator. *Nature photonics 3*(3), 148–151.

Chen, L., H. L. Ma, and H. Y. Cui (2018). Wavefront manipulation based on mechanically reconfigurable coding metasurface. *Journal of Applied Physics 124*(4), 043101.

Cheng, Y., Y. Zou, H. Luo, F. Chen, and X. Mao (2019). Compact ultra-thin seven-band microwave metamaterial absorber based on a single resonator structure. *Journal of Electronic Materials 48*(6), 3939–3946.

Collin, R. E. (1987). *Antennas and radiowave propagation*. McGraw-Hill.

Cong, L., W. Cao, X. Zhang, Z. Tian, J. Gu, R. Singh, J. Han, and W. Zhang (2013). A perfect metamaterial polarization rotator. *Applied Physics Letters 103*(17), 171107.

Cui, T. J., M. Q. Qi, X. Wan, J. Zhao, and Q. Cheng (2014). Coding metamaterials, digital metamaterials and programmable metamaterials. *Light: science & applications 3*(10), e218–e218.

Currie, M., V. D. Wheeler, B. Downey, N. Nepal, S. B. Qadri, J. A. Wollmershauser, J. Avila, and L. Nyakiti (2019). Asymmetric hysteresis in vanadium dioxide thin films. *Optical Materials Express 9*(9), 3717–3728.

D'Aloia, A. G., M. D'Amore, and M. S. Sarto (2020). Low-terahertz transparent graphene-based absorber. *Nanomaterials 10*(5), 843.

D'Arco, A., M. Di Fabrizio, V. Dolci, M. Petrarca, and S. Lupi (2020). Thz pulsed imaging in biomedical applications. *Condensed Matter 5*(2), 25.

Davies, A., E. H. Linfield, and M. B. Johnston (2002). The development of terahertz sources and their applications. *Physics in Medicine & Biology 47*(21), 3679.

Della Giovampaola, C. and N. Engheta (2014). Digital metamaterials. *Nature materials 13*(12), 1115–1121.

Demirhan, Y., H. Alaboz, M. A. Nebioğlu, B. Mulla, M. Akkaya, H. Altan, C. Sabah, and L. Ozyuzer (2017). Fourcross shaped metamaterial filters fabricated from high temperature superconducting ybco and au thin films for terahertz waves. *Superconductor Science and Technology 30*(7), 074006.

Dhillon, A. S. and D. Mittal (2019). Wide band ultrathin polarization insensitive electric field driven metamaterial absorber. *Optics Communications 443*, 186–196.

Duan, G., J. Schalch, X. Zhao, A. Li, C. Chen, R. D. Averitt, and X. Zhang (2019). A survey of theoretical models for terahertz electromagnetic metamaterial absorbers. *Sensors and Actuators A: Physical 287*, 21–28.

El Haddad, J., B. Bousquet, L. Canioni, and P. Mounaix (2013). Review in terahertz spectral analysis. *TrAC Trends in Analytical Chemistry 44*, 98–105.

Elayan, H., O. Amin, R. M. Shubair, and M.-S. Alouini (2018). Terahertz communication: The opportunities of wireless technology beyond 5g. In *2018 International Conference on Advanced Communication Technologies and Networking (CommNet)*, pp. 1–5. IEEE.

Erçağlar, V., H. Hajian, A. E. Serebryannikov, and E. Ozbay (2021). Multifunctional tunable gradient metasurfaces for terahertz beam splitting and light absorption. *Optics Letters 46*(16), 3953–3956.

Fan, F., Y. Hou, Z.-W. Jiang, X.-H. Wang, and S.-J. Chang (2012). Terahertz modulator based on insulator–metal transition in photonic crystal waveguide. *Applied optics 51*(20), 4589–4596.

Fedulova, E., M. M. Nazarov, A. Angeluts, M. Kitai, V. Sokolov, and A. Shkurinov (2012). Studying of dielectric properties of polymers in the terahertz frequency range. In *Saratov Fall Meeting 2011: Optical Technologies in Biophysics and Medicine XIII*, Volume 8337, pp. 83370I. International Society for Optics and Photonics.

Frame, J. D., N. G. Green, and X. Fang (2018). Modified maxwell garnett model for hysteresis in phase change materials. *Optical Materials Express 8*(7), 1988–1996.

Fu, X., F. Yang, C. Liu, X. Wu, and T. J. Cui (2020). Terahertz beam steering technologies: From phased arrays to field-programmable metasurfaces. *Advanced optical materials 8*(3), 1900628.

Gao, L.-H., Q. Cheng, J. Yang, S.-J. Ma, J. Zhao, S. Liu, H.-B. Chen, Q. He, W.-X. Jiang, H.-F. Ma, et al. (2015). Broadband diffusion of terahertz waves by multi-bit coding metasurfaces. *Light: Science & Applications 4*(9), e324–e324.

Gao, M., X. Wang, S. Luo, Q. Lu, S.-N. Luo, C. Lu, S. Chen, F. Long, and Y. Lin (2020). Terahertz transmission properties of vanadium dioxide films deposited on gold grating structure with different periods. *Materials Research Express 7*(5), 056404.

He, M., A. K. Azad, S. Ye, and W. Zhang (2006). Far-infrared signature of animal tissues characterized by terahertz time-domain spectroscopy. *Optics Communications 259*(1), 389–392.

He, X., J. Xu, X. Xu, C. Gu, F. Chen, B. Wu, C. Wang, H. Xing, X. Chen, and J. Chu (2015). Negative capacitance switching via vo2 band gap engineering driven by electric field. *Applied Physics Letters 106*(9), 093106.

Hu, B., Y. Ding, W. Chen, D. Kulkarni, Y. Shen, V. V. Tsukruk, and Z. L. Wang (2010). External-strain induced insulating phase transition in vo2 nanobeam and its application as flexible strain sensor. *Advanced Materials 22*(45), 5134–5139.

Huang, J., J. Li, Y. Yang, J. Li, J. Li, Y. Zhang, and J. Yao (2020). Active controllable bandwidth of thz metamaterial bandpass filter based on vanadium dioxide. *Optics Communications 465*, 125616.

Huang, L., X. Chen, H. Mühlenbernd, H. Zhang, S. Chen, B. Bai, Q. Tan, G. Jin, K.-W. Cheah, C.-W. Qiu, et al. (2013). Three-dimensional optical holography using a plasmonic metasurface. *Nature communications 4*(1), 1–8.

Itoh, T. and C. Caloz (2005). *Electromagnetic metamaterials: transmission line theory and microwave applications*. John Wiley & Sons.

Jackson, J. D. (1999). Classical electrodynamics.

Jeong, J., N. Aetukuri, T. Graf, T. D. Schladt, M. G. Samant, and S. S. Parkin (2013). Suppression of metal-insulator transition in vo2 by electric field–induced oxygen vacancy formation. *Science 339*(6126), 1402–1405.

Jepsen, P. U., B. M. Fischer, A. Thoman, H. Helm, J. Suh, R. Lopez, and R. Haglund Jr (2006). Metal-insulator phase transition in a v o 2 thin film observed with terahertz spectroscopy. *Physical Review B 74*(20), 205103.

Jiang, H., Y. Wang, Z. Cui, X. Zhang, Y. Zhu, and K. Zhang (2022). Vanadium dioxide-based terahertz metamaterial devices switchable between transmission and absorption. *Micromachines 13*(5), 715.

Jiu-sheng, L., L. Shao-he, and Y. Jian-quan (2020). Actively tunable terahertz coding metasurfaces. *Optics Communications 461*, 125186.

Jiu-Sheng, L., Z. Ze-Jiang, and Y. Jian-Quan (2017). Flexible manipulation of terahertz wave reflection using polarization insensitive coding metasurfaces. *Optics express 25*(24), 29983–29992.

Jördens, C., F. Rutz, and M. Koch (2006). Quality assurance of chocolate products with terahertz imaging. In *European conference on non-destructive testing*.

Joy, R., Z. Han, K. Xu, X. Pan, N. Liao, and H. Zhou (2020). Dft investigation of gas sensing characteristics of au-doped vanadium dioxide. *Physics Letters A 384*(32), 126823.

Katzschner, W., A. Steckenborn, R. Löffler, and N. Grote (1984). Ion beam milling of inp with an ar/o2-gas mixture. *Applied physics letters 44*(3), 352–354.

Kemp, M. C., P. Taday, B. E. Cole, J. Cluff, A. J. Fitzgerald, and W. R. Tribe (2003). Security applications of terahertz technology. In *Terahertz for military and security applications*, Volume 5070, pp. 44–52. SPIE.

Kim, H., N. Charipar, M. Osofsky, S. Qadri, and A. Piqué (2014). Optimization of the semiconductor-metal transition in vo2 epitaxial thin films as a function of oxygen growth pressure. *Applied physics letters 104*(8), 081913.

Kim, H.-T., B.-G. Chae, D.-H. Youn, G. Kim, K.-Y. Kang, S.-J. Lee, K. Kim, and Y.-S. Lim (2005). Raman study of electric-field-induced first-order metal-insulator transition in vo 2-based devices. *Applied Physics Letters 86*(24), 242101.

Klimov, V., I. Timofeeva, S. Khanin, E. Shadrin, A. Ilinskii, and F. Silva-Andrade (2002). Hysteresis loop construction for the metal-semiconductor phase transition in vanadium dioxide films. *Technical Physics 47*(9), 1134–1139.

Köseoğlu, H. (2020). Terahertz imaging applications and characterization of ito thin films grown by magnetron sputtering.

Krammer, A., A. Gremaud, O. Bouvard, R. Sanjines, and A. Schüler (2016). In situ photoelectron spectroscopic characterization of reactively sputtered, doped vanadium oxide thin films. *Surface and Interface Analysis 48*(7), 440–444.

Kuznetsov, S. A., M. A. Astafev, M. Beruete, and M. Navarro-Cía (2015). Planar holographic metasurfaces for terahertz focusing. *Scientific reports 5*(1), 1–8.

Landy, N. I., S. Sajuyigbe, J. J. Mock, D. R. Smith, and W. J. Padilla (2008). Perfect metamaterial absorber. *Physical review letters 100*(20), 207402.

Lee, C.-R., S.-H. Lin, S.-M. Wang, J.-D. Lin, Y.-S. Chen, M.-C. Hsu, J.-K. Liu, T.-S. Mo, and C.-Y. Huang (2018). Optically controllable photonic crystals and passively tunable terahertz metamaterials using dye-doped liquid crystal cells. *Journal of Materials Chemistry C 6*(18), 4959–4966.

Lee, Y.-S. (2009). *Principles of terahertz science and technology*, Volume 170. Springer Science & Business Media.

Leroy, J., A. Crunteanu, A. Bessaudou, F. Cosset, C. Champeaux, and J.-C. Orlianges (2012). High-speed metal-insulator transition in vanadium dioxide films induced by an electrical pulsed voltage over nano-gap electrodes. *Applied Physics Letters 100*(21), 213507.

Liu, H., S. Lysenko, A. Rua, V. Vikhnin, G. Zhang, O. Vasquez, and F. Fernandez (2006). Laser excitation and excited state dynamics in vanadium dioxide thin film. *Journal of luminescence 119*, 404–411.

Liu, K., S. Lee, S. Yang, O. Delaire, and J. Wu (2018). Recent progresses on physics and applications of vanadium dioxide. *Materials Today 21*(8), 875–896.

Liu, S., T. J. Cui, L. Zhang, Q. Xu, Q. Wang, X. Wan, J. Q. Gu, W. X. Tang, M. Qing Qi, J. G. Han, et al. (2016). Convolution operations on coding metasurface to reach flexible and continuous controls of terahertz beams. *Advanced Science 3*(10), 1600156.

Liu, S., L. Zhang, Q. L. Yang, Q. Xu, Y. Yang, A. Noor, Q. Zhang, S. Iqbal, X. Wan, Z. Tian, et al. (2016). Frequency-dependent dual-functional coding metasurfaces at terahertz frequencies. *Advanced Optical Materials 4*(12), 1965–1973.

Lu, C., Q. Lu, M. Gao, and Y. Lin (2021). Dynamic manipulation of thz waves enabled by phase-transition vo2 thin film. *Nanomaterials 11*(1), 114.

Lu, H., S. Clark, Y. Guo, and J. Robertson (2021). The metal–insulator phase change in vanadium dioxide and its applications. *Journal of Applied Physics 129*(24), 240902.

Ma, Z., Z. Geng, Z. Fan, J. Liu, and H. Chen (2019). Modulators for terahertz communication: The current state of the art. *Research.*

Manjappa, M., P. Pitchappa, N. Wang, C. Lee, and R. Singh (2018). Active control of resonant cloaking in a terahertz mems metamaterial. *Advanced Optical Materials 6*(16), 1800141.

Mittleman, D. M., R. H. Jacobsen, and M. C. Nuss (1996). T-ray imaging. *IEEE Journal of selected topics in quantum electronics 2*(3), 679–692.

Moccia, M., S. Liu, R. Y. Wu, G. Castaldi, A. Andreone, T. J. Cui, and V. Galdi (2017). Coding metasurfaces for diffuse scattering: scaling laws, bounds, and suboptimal design. *Advanced Optical Materials 5*(19), 1700455.

Muller, A., R. A. Khadar, T. Abel, N. Negm, T. Rosca, A. Krammer, M. Cavalieri, A. Schueler, F. Qaderi, J. Bolten, et al. (2020). Radio-frequency characteristics of ge-doped vanadium dioxide thin films with increased transition temperature. *ACS Applied Electronic Materials 2*(5), 1263–1272.

Ni, X., A. V. Kildishev, and V. M. Shalaev (2013). Metasurface holograms for visible light. *Nature communications 4*(1), 1–6.

Noori, A., B. Akyurek, Y. Demirhan, L. Ozyuzer, K. Guven, H. Altan, and G. Aygun (2023). Terahertz wavefront engineering using a hard-coded metasurface. *Optical and Quantum Electronics 55*(8), 676.

Noori, A., H. Döğer, Y. Demirhan, M. Ozdemir, L. Ozyuzer, G. Aygun, and Ö. Sağlam

(2021). Nanolitography based on electrospun and etched nanofibers. *Microelectronic Engineering 239*, 111526.

Otto, M. R., L. P. R. de Cotret, D. A. Valverde-Chavez, K. L. Tiwari, N. Émond, M. Chaker, D. G. Cooke, and B. J. Siwick (2019). How optical excitation controls the structure and properties of vanadium dioxide. *Proceedings of the National Academy of Sciences 116*(2), 450–455.

Ou, H., F. Lu, Y. Liao, F. Zhu, and Y.-S. Lin (2020). Tunable terahertz metamaterial for high-efficiency switch application. *Results in Physics 16*, 102897.

Park, J. H., J. M. Coy, T. S. Kasirga, C. Huang, Z. Fei, S. Hunter, and D. H. Cobden (2013). Measurement of a solid-state triple point at the metal–insulator transition in vo2. *Nature 500*(7463), 431–434.

Patel, S. K. and J. Parmar (2021). Highly sensitive and tunable refractive index biosensor based on phase change material. *Physica B: Condensed Matter 622*, 413357.

Pedrotti, F. L., L. M. Pedrotti, and L. S. Pedrotti (2017). *Introduction to optics*. Cambridge University Press.

Pendry, J. B. (2000). Negative refraction makes a perfect lens. *Physical review letters 85*(18), 3966.

Pendry, J. B. and D. R. Smith (2004). Reversing light with negative refraction. *Physics today 57*, 37–43.

Pergament, A., G. Stefanovich, and A. Velichko (2013). Oxide electronics and vanadium dioxide perspective: A review. *Journal on Selected Topics in Nano Electronics and Computing 1*(1), 24–43.

Pu, M., C. Hu, M. Wang, C. Huang, Z. Zhao, C. Wang, Q. Feng, and X. Luo (2011). Design principles for infrared wide-angle perfect absorber based on plasmonic structure. *Optics Express 19*(18), 17413–17420.

Qi, Y., Y. Zhang, C. Liu, T. Zhang, B. Zhang, L. Wang, X. Deng, Y. Bai, and X. Wang (2020). A tunable terahertz metamaterial absorber composed of elliptical ring graphene arrays with refractive index sensing application. *Results in Physics 16*, 103012.

Rahm, M., J.-S. Li, and W. J. Padilla (2013). Thz wave modulators: a brief review on different modulation techniques. *Journal of Infrared, Millimeter, and Terahertz Waves 34*(1), 1–27.

Rajabalipanah, H., A. Abdolali, J. Shabanpour, A. Momeni, and A. Cheldavi (2019). Asymmetric spatial power dividers using phase–amplitude metasurfaces driven by huygens principle. *ACS omega 4*(10), 14340–14352.

Ren, Y. and B. Tang (2021). Switchable multi-functional vo 2-integrated metamaterial devices in the terahertz region. *Journal of Lightwave Technology 39*(18), 5864–5868.

Roach, W. and I. Balberg (1971). Optical induction and detection of fast phase transition in vo2. *Solid State Communications 9*(9), 551–555.

Rout, S. and S. Sonkusale (2017). *Active Metamaterials*. Springer.

Sağlam, H. (2013). *Area Dependence of Josephson Critical Current Density in Superconducting Bi 2 Sr 2 CaCu 2 O 8+ d Mesas for Terahertz Emission*. Izmir Institute of Technology (Turkey).

Santulli, A. C., W. Xu, J. B. Parise, L. Wu, M. Aronson, F. Zhang, C.-Y. Nam, C. T. Black, A. L. Tiano, and S. S. Wong (2009). Synthesis and characterization of v 2 o 3 nanorods. *Physical Chemistry Chemical Physics 11*(19), 3718–3726.

Scarborough, C., Z. Jiang, D. Werner, C. Rivero-Baleine, and C. Drake (2012). Experimental demonstration of an isotropic metamaterial super lens with negative unity permeability at 8.5 mhz. *Applied Physics Letters 101*(1), 014101.

Schade, U., L. Puskar, E. Ritter, and J. Beckmann (2020). Etalon effects in thz film measurements. In *2020 45th International Conference on Infrared, Millimeter, and Terahertz Waves (IRMMW-THz)*, pp. 1–1. IEEE.

Shabanpour, J., S. Beyraghi, and A. Cheldavi (2020). Ultrafast reprogrammable multifunctional vanadium-dioxide-assisted metasurface for dynamic thz wavefront engineering. *Scientific reports 10*(1), 1–14.

Shao, L., W. Zhu, M. Y. Leonov, and I. D. Rukhlenko (2019). Dielectric 2-bit coding metasurface for electromagnetic wave manipulation. *Journal of Applied Physics 125*(20), 203101.

Shao, Z., X. Cao, H. Luo, and P. Jin (2018). Recent progress in the phase-transition mechanism and modulation of vanadium dioxide materials. *NPG Asia Materials 10*(7), 581–605.

Shi, R., Y. Chen, X. Cai, Q. Lian, Z. Zhang, N. Shen, A. Amini, N. Wang, and C. Cheng (2021). Phase management in single-crystalline vanadium dioxide beams. *Nature Communications 12*(1), 1–9.

Shin, J.-H., K. H. Park, and H.-C. Ryu (2022). A band-switchable and tunable thz metamaterial based on an etched vanadium dioxide thin film. In *Photonics*, Volume 9, pp. 89. MDPI.

Sui, S., H. Ma, J. Wang, Y. Pang, M. Feng, Z. Xu, and S. Qu (2018). Absorptive coding metasurface for further radar cross-section reduction. *Journal of Physics D: Applied Physics 51*(6), 065603.

Sun, L., L. Zhao, and R.-Y. Peng (2021). Research progress in the effects of terahertz waves on biomacromolecules. *Military Medical Research 8*(1), 1–8.

Taghvaee, H., A. Pitilakis, O. Tsilipakos, A. C. Tasolamprou, N. V. Kantartzis, M. Kafesaki, A. Cabellos-Aparicio, E. Alarcon, and S. Abadal (2022). Multi-wideband terahertz communications via tunable graphene-based metasurfaces in 6g networks. *arXiv preprint arXiv:2203.10298.*

Tan, X., T. Yao, R. Long, Z. Sun, Y. Feng, H. Cheng, X. Yuan, W. Zhang, Q. Liu, C. Wu, et al. (2012). Unraveling metal-insulator transition mechanism of vo2triggered by tungsten doping. *Scientific reports 2*(1), 1–6.

Tao, H., C. Bingham, A. Strikwerda, D. Pilon, D. Shrekenhamer, N. Landy, K. Fan, X. Zhang, W. Padilla, and R. Averitt (2008). Highly flexible wide angle of incidence terahertz metamaterial absorber: Design, fabrication, and characterization. *physical* *review B 78*(24), 241103.

Tao, H., N. I. Landy, C. M. Bingham, X. Zhang, R. D. Averitt, and W. J. Padilla (2008). A metamaterial absorber for the terahertz regime: design, fabrication and characterization. *Optics express 16*(10), 7181–7188.

Tiwari, K. (2015). *The photoinduced phase transitions of vanadium dioxide*. McGill University (Canada).

Tonouchi, M. (2007). Cutting-edge terahertz technology. *Nature photonics 1*(2), 97–105.

Uddin, J. (2017). *Terahertz Spectroscopy: A Cutting Edge Technology*. BoD–Books on Demand.

Wang, L., W. Hong, L. Deng, S. Li, C. Zhang, J. Zhu, and H. Wang (2018). Reconfigurable multifunctional metasurface hybridized with vanadium dioxide at terahertz frequencies. *Materials 11*(10), 2040.

Wang, L., Y. Zhang, X. Guo, T. Chen, H. Liang, X. Hao, X. Hou, W. Kou, Y. Zhao, T. Zhou, et al. (2019). A review of thz modulators with dynamic tunable metasurfaces. *Nanomaterials 9*(7), 965.

Wang, T., Y. Zhang, H. Zhang, and M. Cao (2020). Dual-controlled switchable broadband terahertz absorber based on a graphene-vanadium dioxide metamaterial. *Optical Materials Express 10*(2), 369–386.

Wegkamp, D. and J. Stähler (2015). Ultrafast dynamics during the photoinduced phase transition in vo2. *Progress in Surface Science 90*(4), 464–502.

Wei, M., Z. Song, Y. Deng, Y. Liu, and Q. Chen (2019). Large-angle mid-infrared absorption switch enabled by polarization-independent gst metasurfaces. *Materials Letters 236*, 350–353.

Wen, Q.-Y., Y.-S. Xie, H.-W. Zhang, Q.-H. Yang, Y.-X. Li, and Y.-L. Liu (2009). Transmission line model and fields analysis of metamaterial absorber in the terahertz band. *Optics express 17*(22), 20256–20265.

Wu, C., F. Feng, and Y. Xie (2013). Design of vanadium oxide structures with controllable electrical properties for energy applications. *Chemical Society Reviews 42*(12), 5157–5183.

Wu, G., X. Jiao, Y. Wang, Z. Zhao, Y. Wang, and J. Liu (2021). Ultra-wideband tunable metamaterial perfect absorber based on vanadium dioxide. *Optics Express 29*(2), 2703–2711.

Yang, D., W. Wang, E. Lv, H. Wang, B. Liu, Y. Hou, and J.-h. Chen (2022). Programmable vo2 metasurface for terahertz wave beam steering. *Iscience 25*(8), 104824.

Yang, T.-H., R. Aggarwal, A. Gupta, H. Zhou, R. J. Narayan, and J. Narayan (2010). Semiconductor-metal transition characteristics of vo 2 thin films grown on c-and r-sapphire substrates. *Journal of Applied Physics 107*(5), 053514.

Yin, S., D. Zeng, Y. Chen, W. Huang, C. Zhang, W. Zhang, and Y. E (2022). Optically controlled terahertz dynamic beam splitter with adjustable split ratio. *Nanomaterials 12*(7), 1169.

Yu, N., P. Genevet, M. A. Kats, F. Aieta, J.-P. Tetienne, F. Capasso, and Z. Gaburro (2011). Light propagation with phase discontinuities: generalized laws of reflection and refraction. *science 334*(6054), 333–337.

Yuan, S., R. Yang, J. Xu, J. Wang, and J. Tian (2019). Photoexcited switchable single-/dual-band terahertz metamaterial absorber. *Materials Research Express 6*(7), 075807.

Yüce, H. (2015). Characterization of vanadium oxide thin films grown by magnetron sputtering technique. Master's thesis, İzmir Institute of Technology.

Yurttaş, B. (2021). Development of conductive oxide based thin film modified electrodes and biosensors applications. Master's thesis, Izmir Institute of Technology.

Zhai, Z.-H., S.-C. Chen, L.-H. Du, S.-C. Zhong, W. Huang, Z.-R. Li, H. Schneider, Q. Shi, and L.-G. Zhu (2018). Giant impact of self-photothermal on light-induced ultrafast insulator-to-metal transition in vo 2 nanofilms at terahertz frequency. *Optics*

Express 26(21), 28051–28066.

Zhang, C., G. Zhou, J. Wu, Y. Tang, Q. Wen, S. Li, J. Han, B. Jin, J. Chen, and P. Wu (2019). Active control of terahertz waves using vanadium-dioxide-embedded metamaterials. *Physical Review Applied 11*(5), 054016.

Zhang, G., H. Ma, C. Lan, R. Gao, and J. Zhou (2017). Microwave tunable metamaterial based on semiconductor-to-metal phase transition. *Scientific Reports 7*(1), 1–6.

Zhang, J., L. Yang, L. Li, T. Zhang, H. Li, Q. Wang, Y. Hao, M. Lei, and K. Bi (2017). High-efficiency polarization conversion phase gradient metasurface for wideband anomalous reflection. *Journal of Applied Physics 122*(1), 014501.

Zhang, L., S. Mei, K. Huang, and C.-W. Qiu (2016). Advances in full control of electromagnetic waves with metasurfaces. *Advanced Optical Materials 4*(6), 818–833.

Zhang, M., J. Zhang, A. Chen, and Z. Song (2019). Vanadium dioxide-based bifunctional metamaterial for terahertz waves. *IEEE Photonics Journal 12*(1), 1–9.

Zhao, Y., J. Hwan Lee, Y. Zhu, M. Nazari, C. Chen, H. Wang, A. Bernussi, M. Holtz, and Z. Fan (2012). Structural, electrical, and terahertz transmission properties of vo2 thin films grown on c-, r-, and m-plane sapphire substrates. *Journal of Applied Physics 111*(5), 053533.

Zhao, Y., Y. Zhang, Q. Shi, S. Liang, W. Huang, W. Kou, and Z. Yang (2018). Dynamic photoinduced controlling of the large phase shift of terahertz waves via vanadium dioxide coupling nanostructures. *ACS Photonics 5*(8), 3040–3050.

Zheng, G., H. Mühlenbernd, M. Kenney, G. Li, T. Zentgraf, and S. Zhang (2015). Metasurface holograms reaching 80% efficiency. *Nature nanotechnology 10*(4), 308–312.

Zhou, F., Y. Bao, W. Cao, C. T. Stuart, J. Gu, W. Zhang, and C. Sun (2011). Hiding a realistic object using a broadband terahertz invisibility cloak. *Scientific reports 1*(1), 1–5.

Zhu, Y., S. Vegesna, V. Kuryatkov, M. Holtz, M. Saed, and A. A. Bernussi (2012). Terahertz bandpass filters using double-stacked metamaterial layers. *Optics Letters 37*(3), 296–298.

Zhu, Y., Y. Zhao, M. Holtz, Z. Fan, and A. A. Bernussi (2012). Effect of substrate orientation on terahertz optical transmission through vo 2 thin films and application to functional antireflection coatings. *JOSA B 29*(9), 2373–2378.

APPENDIX A

GENERAL MATLAB CODE FOR PREDICTING FAR-FIELD SCATTERING PATTERNS

This code is a modified version of the (Sui et al., 2018) research paper.

```
clc
clear
close all
f = 0.643e+12;%frequency (Hz)
w = 2*pi*f; %angular frequency (Hz)
c = 3e+8; % speed of light (m/s)
epsilon0 = 8.8541878128e-12; % F*m-1
lambda = c/f;%wavelength (m).
k = 2*pi/lambda; %wave vector (1/m)
m=6;n=m; % the number of unit cells
nSubCell = 8; % number of supercells
d = 100e-6;% (m) unit cell size
dEgree = {’180’};
raD = deg2rad(180);
PhaseMAT = [raD 0;raD  0];
refPhase = (repelem(repmat(PhaseMAT,n/2),nSubCell  ,nSubCell
    ));
refAmp= ones(m*nSubCell,n*nSubCell);
bitAMP_1=0.804898;bitAMP_0=0.987294; %amplitude of coding
    elements ”1” and ”0”, respectively;
for ii=1:1:m*nSubCell
        for jj=1:1:n*nSubCell
              if refPhase(ii,jj)== 0
                    refAmp(ii,jj)=bitAMP_1;
               else
                    refAmp(ii,jj)=bitAMP_0;
               end
```

```
        end
end
M=500;N=500;
theta=linspace(-pi/2,pi/2,M);
phi=linspace(-pi,pi,N);
[theta0,phi0]=meshgrid(theta,phi);
E_t=zeros(N,M);
for ii=1:1:m*nSubCell
        for jj=1:1:n*nSubCell
                E_t=E_t+refAmp(ii,jj).*exp(1i.*(refPhase(ii,jj)+k.*d.*((ii-1/2).*cos(phi0)+(jj-1/2).*sin(phi0)).*sin(theta0)));
        end
end
Ex=abs(E_t).*sin(theta0).*cos(phi0);
Ey=abs(E_t).*sin(theta0).*sin(phi0);
Ez=abs(E_t).*cos(theta0);
Exx=sin(theta0).*cos(phi0);
Eyy=sin(theta0).*sin(phi0);
Ezz=abs(E_t).*cos(theta0);
% normalized Intensity
figure(1)
theta = linspace(0,pi,M);
phi = linspace(-pi/2,pi/2,M);
[THETA,PHI]= meshgrid(theta,phi);
dtheta=pi/M;
dphi=pi/M;
IntenSity = abs(E_t).^2;
NormIntensity=IntenSity./max(max(IntenSity));
plot((THETA-pi/2).*(180/pi), NormIntensity,'r');
xlabel('\theta[deg]','FontSize',10);
ylabel('Normalized intensity','FontSize',10);
title(sprintf('Normalized intensity along theta for %s degree',dEgree{:}));
```

VITA

EDUCATION

2023, Ph.D. in Physics, Graduate School of Engineering and Sciences, Izmir Institute of Technology, Izmir / Turkey
Thesis Title: Modulation of Terahertz Waves by VO_2 Based Metamaterials
Supervisor: Prof. Dr. Gulnur Aygun

2014, M.Sc. in Atomic Molecular Physics, Kharazmi University, Tehran / Iran
Thesis Title: Relativistic Electron Beam Interaction in Quantum Plasma
Supervisor: Prof. Hassan Mehdian
Co-Supervisor: Assoc. Prof. Ali Hasanbeigi

2011, B.Sc. in Solid State Physics, S and B University, Zahedan / Iran

PUBLICATIONS

A. Noori, B. Akyurek, Y. Demirhan, L. Ozyuzer, K. Guven, H. Altan, and G. Aygun
Terahertz wavefront engineering using a hard-coded metasurface.
Optical and Quantum Electronics 55(8), 676 (2023)

A. Noori, H. Döğer, Y. Demirhan, M. Ozdemir, L. Ozyuzer, G. Aygun, and Ö. Sağlam
Nanolitography based on electrospun and etched nanofibers.
Microelectronic Engineering 239, 111526 (2021)